Microdamage Healing in Asphalt and Asphalt Concrete, Volume IV: A Viscoelastic Continuum Damage Fatigue Model of Asphalt Concrete with Microdamage Healing

PUBLICATION NO. FHWA-RD-98-144

JUNE 2001

U.S. Department of Transportation
Federal Highway Administration

Research, Development, and Technology
Turner-Fairbank Highway Research Center
6300 Georgetown Pike
McLean, VA 22101-2296

Technical Report Documentation Page

1. Report No.	2. Government Accession No.	3. Recipient's Catalog No.
FHWA-RD-98-144		

4. Title and Subtitle	5 Report Date
Microdamage Healing in Asphalt and Asphalt Concrete, Volume IV: A Viscoelastic Continuum Damage Fatigue Model of Asphalt Concrete with Microdamage Healing	June 2001
	6. Performing Organization Code

7. Author(s)	8. Performing Organization Report No.
R. L. Lytton, C. W. Chen and Dallas N. Little	Research Report 7229

9. Performing Organization Name and Address	10. Work Unit No. (TRAIS)
Texas Transportation Institute The Texas A&M University System College Station, Texas 77843-3135	11. Contract or Grant No. DTFH61-92-C-00170

12. Sponsoring Agency Name and Address	13. Type of Report and Period Covered
Western Research Institute (WRI) P.O. Box 3395 University Station Laramie, Wyoming 82071	Final: February 1998
	14. Sponsoring Agency Code

15. Supplementary Notes

Research performed in cooperation with the Federal Highway Administration.
Research Project Title: Fundamental Properties of Asphalts and Modified Asphalts
Task K - Microdamage Healing in Asphalt and Asphalt Concrete

16. Abstract

A mechanistic approach to fatigue characterization of asphalt-aggregate mixtures is presented in this volume. This approach is founded on a uniaxial viscoelastic constitutive model that accounts for damage evolution under cyclic loading conditions. The elastic-viscoelastic correspondence principle is applied in order to evaluate damage growth and healing in cyclic loading separately from time-dependent characteristics of the material. The damage growth during loading cycles and healing during rest periods are modeled using work potential theory, a continuum damage theory based on thermodynamics of irreversible processes. Internal state variable formulation was used in developing the analytical representation model. Tensile uniaxial fatigue tests were performed in the controlled-strain mode with different strain amplitudes to determine model parameters. The resulting constitutive model successfully predicts the damage growth of asphalt concrete under monotonic loading at varying strain rates and damage growth and recovery due to complex loading histories, in both controlled-strain and controlled-stress modes, composed of randomly applied multi-level loading with different loading rates and varying durations of rest.

Fatigue lives of two different mixtures were predicted with reasonable accuracy using the constitutive model for the constant stress-strain amplitude cyclic loading histories with and without rest periods. A standard uniaxial fatigue test protocol is proposed by simplifying the experimental approach used in developing the constitutive model.

17. Key Words	18. Distribution Statement
controlled-stress modes, controlled-strain, damage growth, fatigue characterization	No restrictions. This document is available to the public through NTIS: National Technical Information Service 5285 Port Royal Road Springfield, Virginia 22161

19. Security Classif.(of this report)	20. Security Classif.(of this page)	21. No. of Pages	22. Price
Unclassified	Unclassified	178	

Form DOT F 1700.7 (8-72) Reproduction of completed page authorized

SI* (MODERN METRIC) CONVERSION FACTORS

APPROXIMATE CONVERSIONS TO SI UNITS

Symbol	When You Know	Multiply By	To Find	Symbol
	LENGTH			
in	inches	25.4	millimeters	mm
ft	feet	0.305	meters	m
yd	yards	0.914	meters	m
mi	miles	1.61	kilometers	km
	AREA			
in^2	square inches	645.2	square millimeters	mm^2
ft^2	square feet	0.093	square meters	m^2
yd^2	square yards	0.836	square meters	m^2
ac	acres	0.405	hectares	ha
mi^2	square miles	2.59	square kilometers	km^2
	VOLUME			
fl oz	fluid ounces	29.57	milliliters	mL
gal	gallons	3.785	liters	L
ft^3	cubic feet	0.028	cubic meters	m^3
yd^3	cubic yards	0.765	cubic meters	m^3
NOTE: Volumes greater than 1000 l shall be shown in m^3.				
	MASS			
oz	ounces	28.35	grams	g
lb	pounds	0.454	kilograms	kg
T	short tons (2000 lb)	0.907	megagrams (or "metric ton")	Mg (or "t")
	TEMPERATURE (exact)			
°F	Fahrenheit temperature	5(F-32)/9 or (F-32)/1.8	Celcius temperature	°C
	ILLUMINATION			
fc	foot-candles	10.76	lux	lx
fl	foot-Lamberts	3.426	candela/m^2	cd/m^2
	FORCE and PRESSURE or STRESS			
lbf	poundforce	4.45	newtons	N
lbf/in^2	poundforce per square inch	6.89	kilopascals	kPa

APPROXIMATE CONVERSIONS FROM SI UNITS

Symbol	When You Know	Multiply By	To Find	Symbol
	LENGTH			
mm	millimeters	0.039	inches	in
m	meters	3.28	feet	ft
m	meters	1.09	yards	yd
km	kilometers	0.621	miles	mi
	AREA			
mm^2	square millimeters	0.0016	square inches	in^2
m^2	square meters	10.764	square feet	ft^2
m^2	square meters	1.195	square yards	yd^2
ha	hectares	2.47	acres	ac
km^2	square kilometers	0.386	square miles	mi^2
	VOLUME			
mL	milliliters	0.034	fluid ounces	fl oz
L	liters	0.264	gallons	gal
m^3	cubic meters	35.71	cubic feet	ft^3
m^3	cubic meters	1.307	cubic yards	yd^3
	MASS			
g	grams	0.035	ounces	oz
kg	kilograms	2.202	pounds	lb
Mg (or "t")	megagrams (or "metric ton")	1.103	short tons (2000 lb)	T
	TEMPERATURE (exact)			
°C	Celcius temperature	1.8C + 32	Fahrenheit temperature	°F
	ILLUMINATION			
lx	lux	0.0929	foot-candles	fc
cd/m^2	candela/m^2	0.2919	foot-Lamberts	fl
	FORCE and PRESSURE or STRESS			
N	newtons	0.225	poundforce	lbf
kPa	kilopascals	0.145	poundforce per square inch	lbf/in^2

* SI is the symbol for the International System of Units. Appropriate rounding should be made to comply with Section 4 of ASTM E380.

(Revised September 1993)

TABLE OF CONTENTS

TABLE OF CONTENTS
(continued)

LIST OF TABLES

LIST OF FIGURES

List of Figures
(Continued)

PROJECT SUMMARY

Background and Objectives

This final report documents the findings of a four and one-half year study of ***"Microdamage Healing in Asphalt and Asphalt Concrete."*** The study is identified as Task K in a larger overall study under the direction of Western Research Institute entitled ***"Fundamental Properties of Asphalts and Modified Asphalts."*** The study was sponsored by the Federal Highway Administration (FHWA) under contract number DTFH61-92-C-00170. Work in Task K was a joint effort between the Texas Transportation Institute (TTI) of Texas A&M University and the Department of Civil Engineering at North Carolina State University (NCSU).

The final report is divided, for reasons of readability and ease of documentation, into four volumes: (1) Microdamage Healing - Project Summary Report, (2) Evidence of Microdamage Healing, (3) Microdamage and Healing Model, and (4) Viscoelastic Continuum Damage Fatigue Model.

There were five primary study objectives:

1. Demonstrate that microdamage healing occurs and that it can be measured in the laboratory and in the field.
2. Confirm that the same fracture properties that control propagation of visible cracks control the propagation of microcracks, and determine the effects of microdamage healing on these fracture properties and basic fracture parameters.
3. Identify the asphalt constituents that influence microdamage and microdamage healing.
4. Establish appropriate correlations between microdamage and microdamage healing in the laboratory and in the field.
5. Predict the effect of microdamage healing on pavement performance and develop the appropriate constitutive damage models that account for the effects of microdamage healing on the performance of asphalt concrete pavement layers.

By satisfying the objectives of this research, FHWA will be able to:

1. Establish the validity and significance of microdamage healing in flexible pavement design and analysis.
2. Identify how microdamage healing can be utilized in pavement design and analysis.
3. Maximize pavement performance life by selecting asphalt binders that maximize microdamage healing.

Volume 1: Microdamage Healing - Project Summary Report

Volume 1 is a summary report that chronicles the research highlights of the entire study. Volume 1 describes the success of the project in addressing the project objectives as summarized in the following paragraphs.

The initial research objective was to demonstrate that healing occurs and can be measured both in the laboratory and in the field. Healing was verified on laboratory test samples that demonstrated that dissipated pseudo-strain energy (DPSE), which steadily decreased during cyclic, controlled-strain loading, was recovered after rest periods. The level and rate of the recovered DPSE varied in a logical manner corresponding to changes in the duration of the rest period and the temperature during the rest period. A parameter called the Healing Index (HI) was developed to quantify the magnitude of healing. Furthermore, a Micromechanics Fatigue and Healing Model (MFHM) was developed in this study on the basis of the basic laws of fracture and microcrack growth. This model predicts the size distribution of microcracks and the growth of the microcracks as the fatigue process continues. The model, which is based on a relationship between stiffness loss during the fatigue process (due to microcrack damage) and the rate of change in DPSE, reveals a reduced average length of microcracks in the sample following rest periods. The MFHM model can be used to accurately calculate (by reverse calculation techniques) pertinent material properties and the rate of change in DPSE during the fatigue and healing process at temperatures below 25°C. However, the back-calculated pertinent material properties and the rate of change in DPSE cannot be accurately predicted using the MFHM at temperatures above about 25°C. This is because below 25°C, the change in damage during cyclic loading is almost all due to microcrack growth and healing. However, at the higher temperatures, plastic deformation occurs to a considerable extent, and plastic damage is not accounted for by the MFHM.

Convincing evidence of healing based on field data further verifies the occurrence of and ability to measure microdamage and healing. The stiffness of damaged roadways was found to recover or increase after rest periods where the stiffness was measured using in situ surface wave techniques. Experiments that verify healing were performed on U.S. 70 in North Carolina, the MnROAD project in Minnesota, and the Accelerated Loading Facility in McLean, Virginia.

The second research objective, using the MFHM, which is based on fracture mechanics principles, was to confirm that the same fracture properties that control the propagation of visible cracks also control the propagation of microcracks and determine the effects of microdamage healing on the basic fracture properties and the fatigue life.

The third objective was to identify the asphalt constituents that influence microdamage and microdamage healing. Five asphalts ranging widely in aromatic, amphoteric, and wax contents were considered, and asphalts with low amphoteric and

high aromatic contents were found to be better healers. However, the most important relationship between binder properties and healing was based on surface energy, which was shown to be fundamentally related to fracture and healing in a landmark study by Richard Schapery. More specifically, two components of surface energy (the polar and the non-polar component) were found to explain experimental data on the rate of early healing and the development of long-term healing.

The fourth objective was to establish appropriate correlations between microdamage and microdamage healing in the laboratory and in the field. This was accomplished, as evidence verifies that a very significant level of recovery or healing occurs in the field following rest periods, and this level of recovery is in agreement with the magnitude of healing measured in the laboratory.

Finally, the project sought to predict the effect of microdamage healing on pavement performance and to develop an appropriate damage model. Two complementary approaches to the accomplishment of this objective were developed in this research. One was the development of the viscoelastic continuum damage mechanics model (CDM) and the second was the micromechanics fatigue and healing model (MFHM). The CDM can be used to assess fatigue life from either controlled-strain or controlled-stress fatigue experiments and the direct effects of rest periods (healing) on damage. Whereas the CDM offers an assessment of generic damage, the MFHM offers considerable insight into how material properties of the mixture affect fracture rate, healing rate and the net rate of crack growth or fatigue, which is a balance between fracture rate and healing rate.

Volume 2: Evidence of Microdamage Healing

Volume 2 documents laboratory and field testing that provides the evidence that microdamage healing is real and measurable and that it has a significant impact on pavement performance.

Part of the laboratory experiments to evaluate the impact of rest periods were performed at North Carolina State University (NCSU). In these experiments, fatigue damage was induced through flexural beam experiments. Damage was recorded as the flexural stiffness of the beam became smaller during the flexural fatigue experiment and as the dynamic modulus of elasticity (as measured from impact resonance) became smaller. The experiment included two very different asphalt binders: AAD and AAM. The experiment clearly demonstrated that the rest periods introduced after fatigue damage allowed significant recovery in the flexural and dynamic modulus. The recovery was attributed to the healing of microcracks within the sample. The time of the rest period and the temperature of the sample during the rest period were found to significantly affect the degree of healing. The healing potentials of AAD and AAM asphalt cements were evaluated using four different indicators. Each indicator showed AAM to be a significantly better healer than AAD.

A separate series of laboratory testing was performed at Texas A&M University's Texas Transportation Institute (TTI). These tests consisted of controlled-strain haversine loading direct tensile tests and controlled-strain trapezoidal loading direct tensile tests. The change and rate of change in DPSE were recorded throughout the test and after rest periods introduced during the fatigue tests. The recovered DPSE after the rest period normalized by the DPSE before the rest period defined a Healing Index (HI) term used to quantify healing. Although healing was found to be dependent on the temperature of mixture during the rest period and the length of the rest period, it was also found to be highly dependent on the type of asphalt cement. Asphalt AAM was found to provide much better healing properties than asphalt AAD, which is in agreement with the work of NCSU where significantly different testing protocols were used.

A discussion is presented in Volume 2 that explains the importance of transforming the dissipated energy into pseudo-dissipated energy in order to accurately evaluate the relative ability of the various mixtures to heal. The transformation to pseudo-strain energy can be tedious and painfully slow. However, a linear transformation protocol is presented that is acceptably accurate and efficient. This protocol was used in this research to calculate pseudo-dissipated energies for the mixtures compared.

The TTI laboratory work demonstrated that several factors may influence the measure of microdamage healing apart from crack healing: molecular structuring or steric hardening, temperature confoundment, and stress relaxation during loading and rest periods. Each factor is discussed with respect to its role in influencing microdamage and microdamage healing. The conclusions are that: 1) molecular structuring is not of significance or importance for the rest periods and test protocols used in this study; 2) temperature increase upon loading or dissipation during rest periods was minimal in these experiments and had an insignificant impact on measured properties due to the nature of the test protocol, number of loading cycles used, and length of rest periods; and 3) stress relaxation must be accounted for (as it was) in the presentation of data as they relate to microdamage healing.

The influence of several factors as they affect microdamage healing (the healing index) are discussed. These include the effects of low density polyethylene (LDPE) as an asphalt additive, the effects of age-hardening (including the effects of hydrated lime as an inhibitor of hardening), the effect of five different binders (exhibiting very different compositional properties) and the effect of different mixture types (dense graded mixtures versus stone mastic type mixtures).

The most notable finding presented in this volume is the difference in healing indices among the five virgin binders evaluated. A strong relationship between surface energy of the binder and the magnitude of healing and the rate of realization of maximum healing is presented. This relationship agrees with the fundamental (fracture mechanics-based) explanation of fatigue presented in Volume 3. In this fundamental relationship, the fatigue

process is presented as a balance between the fracture during loading and healing or recovery during periods of rest.

Volume 2 completes the evidence of microdamage healing with convincing field evidence. Wave speed and attenuation measurements were made on in situ pavements. The stress wave test and analysis successfully detected fatigue damage growth and microdamage healing of asphalt pavements (at the FHWA's Turner-Fairbank Highway Research Center - Accelerated Loading Facility) with different asphalt layer thicknesses and viscosities and demonstrated the importance of microdamage healing during rest periods on pavement performance. The ability of stress wave testing to measure microdamage and healing in the field was further evaluated at the Minnesota Road Project (Mn/ROAD) on seven pavement test sections at the site. The results further confirmed that the stress wave analysis can be used to monitor microdamage growth and healing in the field. The conclusion of the field study was that, although healing of asphalt concrete pavements in the field is more difficult to measure than in the controlled setting of a laboratory, it can be accurately detected using stress wave analysis. The fact that healing does occur in pavements in the field during rest periods suggests that the performance and service life of the pavement will be increased if rest periods are introduced, or if binders are used that heal more quickly and completely.

Volume 3: Micromechanic Fatigue and Healing Model

Volumes 3 and 4 present two different ways of describing the fatigue cracking in mixes. In both volumes, the sample being tested is damaged. The two approaches differ in their ways of characterizing cracking. In Volume 3, it is assumed that all of the damage is due to cracking and obeys the fracture and healing laws that have been established for viscoelastic materials. In this approach the material properties that are relevant to these fracture and healing laws may be measured independently of the sample that is tested in fatigue. The resulting model of fatigue cracking and healing is the Micromechanics Fracture and Healing Model (MFHM). In Volume 4, the sample is assumed to suffer a generic "damage" with which no material properties are associated. Instead, model coefficients are found by analysis of the sample damage and healing data. The resulting model is the continuum damage model (CDM). Tests were run and interpreted using the MFHM at 4°C, 25°C and 40°C. At the lower temperatures (4°C and 25°C), the MFHM model was used to calculate the cohesive fracture and healing surface energies, which were measured independently using a Wilhemy Plate apparatus. The calculated and measured values matched well within reasonable experimental error. However, at 40°C, the calculated surface energies did not match the measured values, indicating that a mechanism other than fracture and healing was operating at the higher temperature. The most likely damage mechanism to operate at the higher temperature is plastic flow. This suggests that a continuum damaged model (CDM) at the higher temperatures will probably be of a different form with different sets of model coefficients than what was found to fit the fracture and healing damage mechanism at the lower temperatures as

discussed in Volume 4. The most likely dividing line between the fracture and healing mechanism and the plastic flow mechanism is the stress free temperature of the asphalt concrete mixture.

Three events occur simultaneously in asphalt mixtures under strain-controlled fatigue loading. These are relaxation, fracture and healing. Relaxation of stress is a direct result of asphalt molecular structure. Fracture can be regarded as the growth of microcracks or macrocracks during loading, and healing is the recovery of the asphalt structure during rest periods. Healing is at least partly due to the recovery of bonding strength at the closure of fracture faces. The relaxation and healing mechanisms extend the performance life of asphalt mixtures while fatigue damage degrades their quality.

The theories of fracture mechanics are well established for time-independent materials, such as metals. However, analysis methods to characterize the behavior of time-dependent viscoelastic materials are rare. A number of approximate interrelationships between linear elastic and viscoelastic properties have been developed; however, they are only applicable to quasi-static problems. Finding a closed-form solution to quantify the response of viscoelastic materials under general loading conditions is one of the objectives of a portion of the study described in this volume. A second objective of this portion of the research was to show that the same fracture properties that control the propagation of visible cracks control the propagation of microcracks.

It is a third objective to show that the microfracture and healing properties that can be calculated from the measured results of tensile fatigue tests match the cohesive fracture and healing properties of the asphalt binder that can be measured independently. It is this third objective which demonstrates closure: The microfracture and healing theory proposed in this report actually does predict the measured results.

An extended background review of the literature, which supports much of the development of the models presented in this volume, is presented in the Ph.D. dissertation of Chen [1997]. This volume presents a finite element model, which is used to calculate the fracture properties of asphalt mixtures and to calculate damage behavior (average crack length and density of crack distribution) during fatigue testing. The fracture properties and damage assessment is based on dissipated pseudo-strain energy, which is recorded throughout the test. Based on the microfracture and healing model, a fundamental relation of viscoelastic fracture was derived and is presented in this volume. This fundamental law is used to describe the rate or speed of fracture and the rate or speed of microfracture healing based on fundamental properties of the mixture and its components. The law defines the fatigue process as being a balance between the rate of fracture and the rate of healing. The fundamental relationship identifies component and global mixture properties that affect fracture and healing. Tests to measure these material properties show potential for development into specification tests. Among these are the surface energy tests for binders and aggregates and mixture tensile and compressive

compliance tests. The reasonableness of the approach is demonstrated by the fact that the fundamental relationship of viscoelastic fracture mechanics was used to calculate fracture and healing surface energies from actual fatigue test pseudo-dissipated energy data and fundamental mixture fracture properties calculated from these data. The calculated mixture surface energies were within a reasonable range of those measured separately for the binder and mixture as discussed in Volume 3.

The analytical methods presented in this volume demonstrate a reduction in average microcrack length following rest periods and that the same fundamental fracture parameters that influence macrocrack growth (fractures larger than about 7.5 mm) also control microcrack growth.

Volume 4: Viscoelastic Continuum Damage Fatigue Model of Asphalt Concrete With Microdamage Healing

A mechanistic approach to fatigue characterization of asphalt-aggregate mixtures is presented in this volume. This approach is founded on a uniaxial viscoelastic constitutive model that accounts for damage evolution under cyclic loading conditions. The elastic-viscoelastic correspondence principle is applied in order to evaluate damage growth and healing in cyclic loading separately from time-dependent characteristics of the material. The damage growth during loading cycles and healing during rest periods are modeled using work potential theory, a continuum damage theory based on thermodynamics of irreversible processes. Internal state variable formulation was used in developing the analytical representation model. Tensile uniaxial fatigue tests were performed in the controlled-strain mode with different strain amplitudes to determine model parameters. The resulting constitutive model successfully predicts the damage growth of asphalt concrete under monotonic loading at varying strain rates and damage growth and recovery due to complex loading histories, in both controlled-strain and controlled-stress modes, composed of randomly applied multi-level loading with different loading rates and varying durations of rest.

Fatigue lives of two different mixtures were predicted with reasonable accuracy using the constitutive model for the constant stress-strain amplitude cyclic loading histories with and without rest periods. A standard uniaxial fatigue test protocol is proposed by simplifying the experimental approach used in developing the constitutive model.

A VISCOELASTIC CONTINUUM DAMAGE FATIGUE MODEL OF ASPHALT CONCRETE WITH MICRODAMAGE HEALING

VOLUME SUMMARY

A mechanistic approach to fatigue characterization of asphalt-aggregate mixtures is presented in this section. This approach is founded on a uniaxial viscoelastic constitutive model that accounts for damage evolution under cyclic loading conditions. The elastic-viscoelastic correspondence principle is applied in order to evaluate damage growth and healing in cyclic loading separately from time-dependent characteristics of the material. The damage growth during loading cycles and healing during rest periods are modeled using the work potential theory, a continuum damage theory based on thermodynamics of irreversible process. Internal state variable formulation was used in developing the analytical representation of the model. Tensile uniaxial fatigue tests were performed under the controlled-strain mode with different strain amplitudes to determine model parameters. The resulting constitutive model successfully predicts the damage growth of asphalt concrete under monotonic loading of varying strain rates and damage growth and recovery due to complex loading histories, in both controlled-strain and controlled-stress modes, composed of randomly applied multi-level loading with different loading rates and varying durations of rest.

Fatigue lives of two different mixtures are predicted with a reasonable accuracy using the constitutive model for the constant stress/strain amplitude cyclic loading histories with and without rest periods. A standard uniaxial fatigue test protocol is proposed by simplifying the experimental approach used in developing the constitutive model.

To provide effective readability, this section contains only the summary of information that is critical to discuss the modeling approach and practical implications of the model. Theories, detailed steps involved in developing the proposed fatigue prediction model, and the individual test results are presented in Appendix B.

CHAPTER 1: INTRODUCTION

Fatigue cracking due to repeated traffic loading is one of the major distresses in asphalt concrete pavements. These cracks start as microcracks and later propagate, densify, and coalesce due to tensile or shear stresses or combinations of both to form macrocracks. Since both crack initiation and propagation processes are directly related to stress-strain fields in asphalt layers, accurate evaluation of fatigue behavior necessitates a sound understanding of the hysteretic constitutive behavior of asphalt concrete under realistic traffic conditions.

For many years, significant research efforts have focused on developing reliable fatigue prediction models. These models usually relate the *initial* response (such as tensile strain) of asphalt mixture to the fatigue life, and as a result, they cannot account for complex damage under realistic loading conditions (e.g., multi-level loading, rest periods, etc.) that occur throughout the fatigue life. These models are simple to use because the only measured response of the mixture is at the initial stage of fatigue testing. However, with the advanced automatic control/data acquisition systems available today, this advantage of simplicity is not substantial.

Development of a fundamentally sound constitutive model serves two important purposes. For pavement engineers, the constitutive model can provide accurate information on fatigue performance of asphalt concrete under realistic loading conditions, leading to better assessment of fatigue life of a new pavement or the remaining life of an existing pavement. For materials engineers, the constitutive model founded on basic principles in mechanics provides relationships between material properties (chemical or mechanical) and model parameters, which can be used for selection or design of more fatigue-resistant binders or mixtures.

This section describes a mechanistic approach to viscoelastic constitutive modeling of asphalt concrete with damage evolution under realistic cyclic loading conditions. First, needs for a fundamentally sound constitutive fatigue model are presented. Then, a review of the proposed constitutive theory is provided with some experimental verification results. A procedure for determining important viscoelastic material properties is then discussed, as if the development of the constitutive model using internal state variable formulation and experimental results. The model is then verified using complex loading histories with random multi-level loads and varying rest periods under different modes of loading. Finally, recommendations are made on how this model can be used in specification-type fatigue performance prediction of asphalt concrete.

Needs

The most common and classical fatigue model is developed by correlating fatigue life with initial strain or stress levels applied during tests. The limitation of this

phenomenological model is that the damage evolution is not taken into consideration and hence it can only be applied to a given set of loading conditions. Also, many researchers have shown that this fatigue model grossly underpredicts field fatigue life as summarized in Kim et al. (1994). The so-called lab-to-field shift factor has been used to compensate for this discrepancy. According to Finn et al. (1977), the average value of shift factors is approximately 13. The difference between fatigue lives from the laboratory model and those observed from the in-service pavements can be mainly attributed to differences in loading and environmental conditions and changes in material properties in the field.

It is obvious that one cannot eliminate the shift factor completely by simply adopting more sophisticated material models; however, it is important for the designer to determine the magnitude of the shift. If there is a significant difference in shift factor due to the selection of asphalt binder and mix design alone, then this points immediately toward an important material property that can extend the fatigue service life of pavements. Material properties can be found by using the discipline of mechanics through which the state of stress and strain can be computed.

In order to develop a constitutive model that can be used as an effective fatigue performance model, the following three areas were identified as important factors: viscoelasticity of asphalt concrete, microdamage healing, and mode of loading.

Viscoelasticity

In recent years, the dissipated energy approach has been employed in predicting the fatigue lives of asphalt concrete that is based on the assumption that the number of cycles to failure is related mainly to the amount of energy dissipated during the test. A major advantage of this approach compared with the classical model is that predicting the fatigue behavior of a certain mix type over a wide range of conditions from a few simple fatigue tests is possible (Van Dijk and Visser, 1977).

A more rigorous approach has been presented by Kim and Little (1990), Kim et al. (1995b), and Lee and Kim (1996) in which the hysteretic behavior of asphalt concrete is attributed to three major mechanisms that take place under traffic loading: fatigue damage growth; time-dependence due to the viscoelastic nature of the material; and chemical healing across microcrack and macrocrack interfaces. The major difference in Kim's approach from the dissipated energy approach stems from the recognition of the fact that the energy dissipation under cyclic loading is not only related to the damage growth, but also due to the time-dependence of asphalt concrete. In order to illustrate this point, stresses due to a cyclic strain history (Figure 1(a)) are calculated from a linear viscoelastic constitutive equation for the uniaxial loading condition with a typical relaxation modulus of asphalt concrete:

$$\sigma = \int_0^t E(t-\iota)\frac{d\epsilon}{d\tau}\,d\tau \qquad (1)$$

where E(t) = relaxation modulus; σ = uniaxial stress; and ϵ = uniaxial strain. Equation (1) has nothing to do with damage. The resulting stress-strain behavior is displayed in Figure 1(b). As can be seen from this figure, hysteresis loops are observed even though there is no damage induced in the material. In addition, the stresses decrease as cyclic loading continues due to the relaxation of asphalt concrete.

Kim and Little (1990) applied the extended elastic-viscoelastic correspondence principle and damage mechanics proposed by Schapery (1984) to model the damage growth and healing separately from the viscoelastic effect. Although the resulting model from Kim and Little's work was verified using short-term fatigue (about 60 cycles) tests, it satisfactorily predicted the constitutive behavior of asphalt concrete under random multi-level loading with varying durations of rest, demonstrating the possibility of establishing a means of accounting for the differences between the laboratory and the field loading histories.

Microdamage Healing

Recent studies at North Carolina State University have demonstrated the importance of rest period on fatigue performance both in the laboratory and the field. Third-point-load beam fatigue tests have revealed that the introduction of three 1-day long rest periods at 25°C can increase the fatigue life of asphalt concrete beams by 50 percent (Sias, 1996). Also, Kim et al., (1994) used a stress wave technique to measure the change in the elastic modulus of asphalt concrete after rest periods in actual pavements (US 70, Clayton, NC). The first field evidence of the increase in modulus after a rest period is presented in Figure 2(a). The modulus of the AC layer, determined by the stress wave technique, decreased as the pavement temperature increased. Also, the elastic modulus after a 24-hour rest period (Point B) was greater than that before the rest period (Point A) for the same AC mid-depth temperature.

In order to investigate the possible link between this observation and the recovery from damage, Mn/ROAD pavement sections were tested in October 1993 using the same stress wave technique. At the time of the field tests, the Mn/ROAD pavements were not opened to traffic while the US 70 section had been damaged for a year. Stress wave tests were conducted for 36 hours continuously, and the test results are displayed in Figure 2(b). Different from the behavior seen in Figure 2(a), the modulus versus temperature relationships during the 1st day, night, and the 2nd day superpose well.

There are several possible reasons that can be attributed to this difference. The first is the relaxation of the material due to the material's inherent viscoelastic nature. During the rest period in the US 70 pavement, the deformation recovered and the

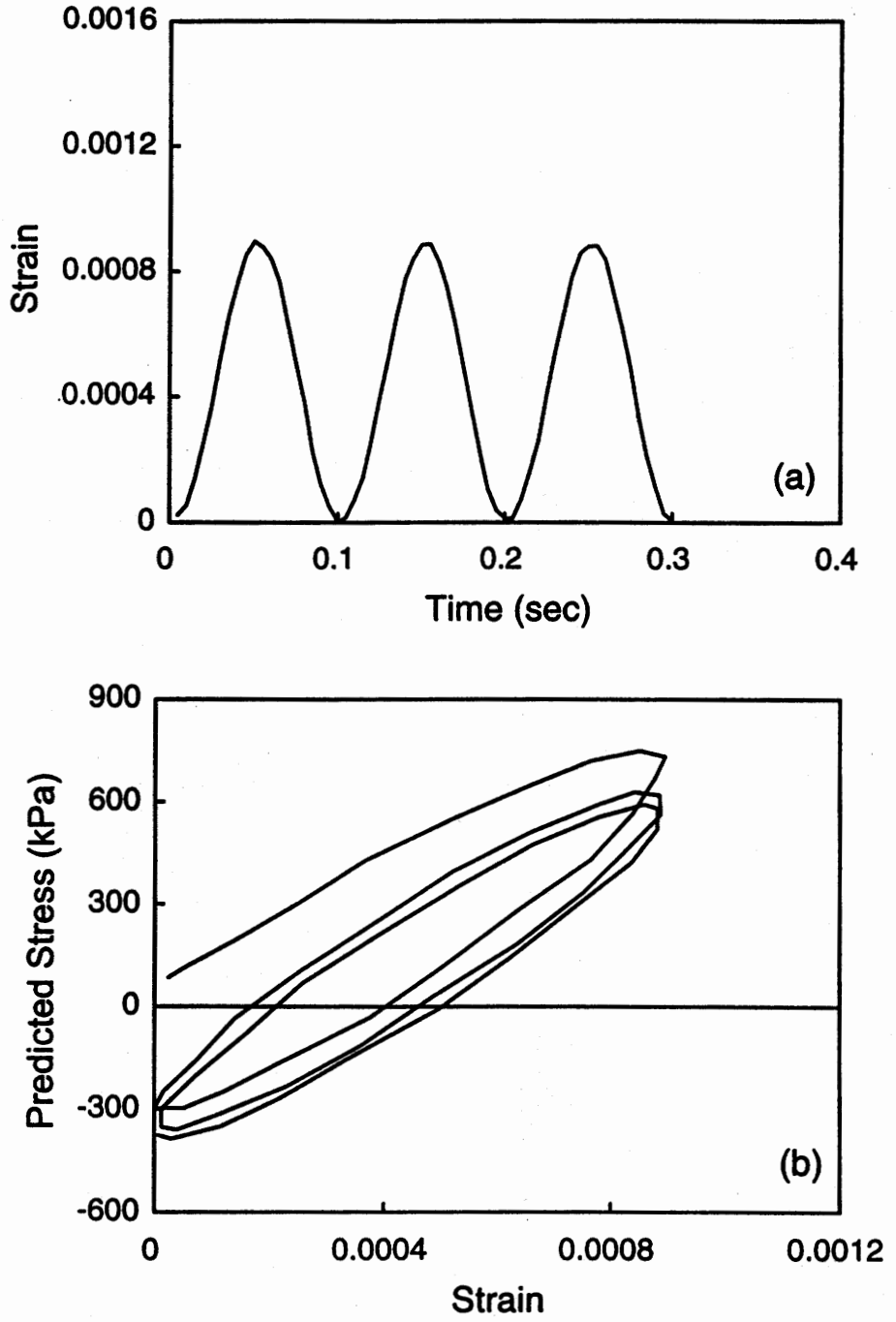

Figure 1. Stress-Strain Behavior of a Typical Asphaltic Mix Obtained from a Linear Viscoelastic Constitutive Relationship: (a) Strain Input; (b) Predicted Stress-Strain Behavior.

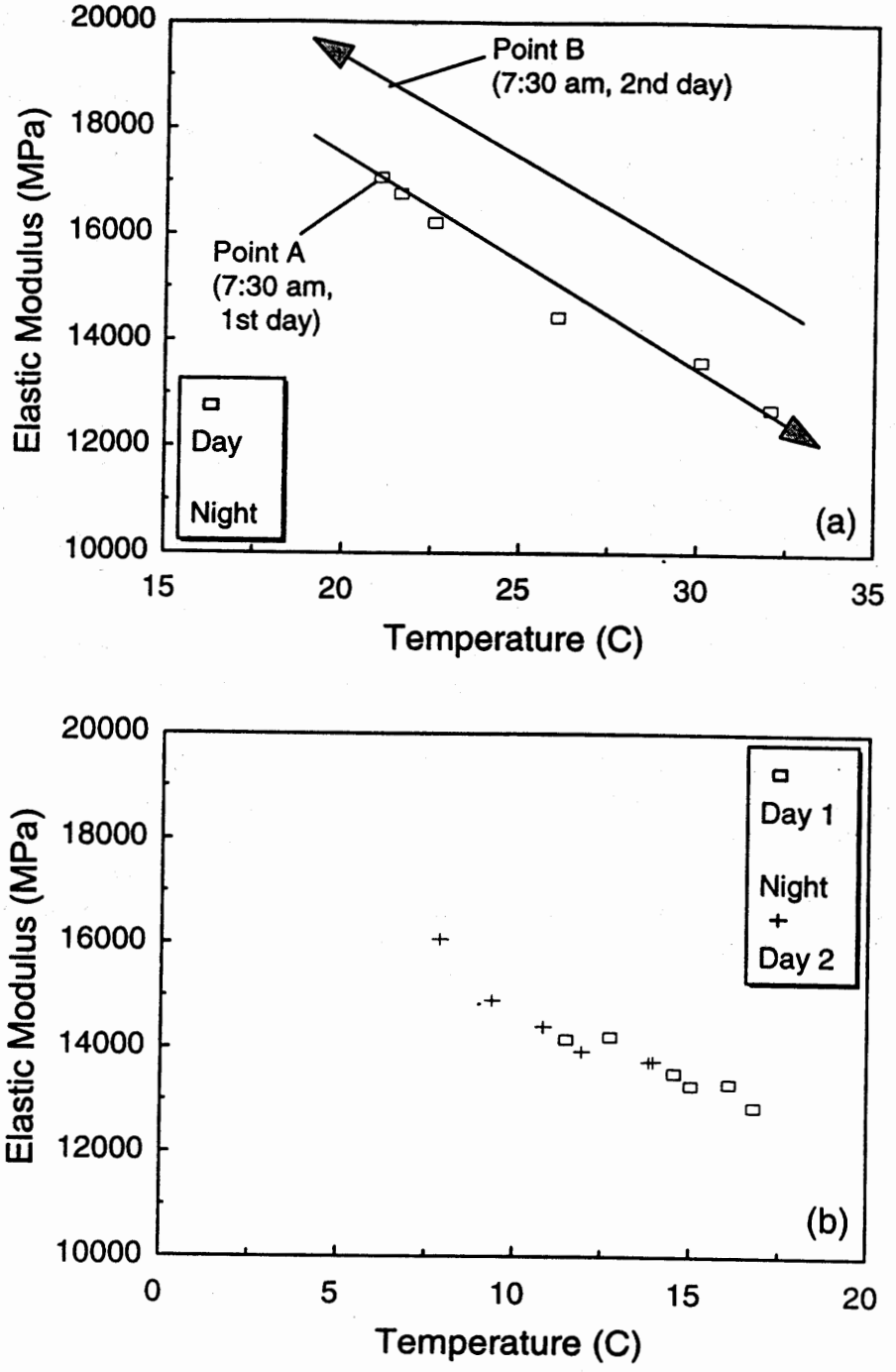

Figure 2. Change in the Elastic Modulus as a Function of AC Mid-Depth Temperature During: (a) the 24-hour Rest Period in Us 70, NC; (b) the 36-hour Rest Period in Mn/Road, MN.

microstructure of asphalt concrete changed, which probably contributed to the change in the elastic modulus. The second possibility is the steric hardening of asphalt binder due to molecular restructuring during rest periods. The third reason for the increase in the elastic modulus during rest periods in US 70 pavement is the healing of microcracks, which is a well-proven phenomenon in polymer engineering. Determining how much of the beneficial effects of rest periods are contributed from each of these factors is extremely difficult, if not impossible. In this study, the beneficial effects of rest periods that cannot be accounted for using the correspondence principle are included under the term of "microdamage healing."

Mode of loading

Another important issue in the fatigue testing and analysis of asphalt concrete is mode of loading. Generally, fatigue test methods fall into one of two types, either *controlled stress,* when a constant stress amplitude is applied, or *controlled strain,* when a constant strain amplitude is applied. The controlled-stress mode of loading appears to represent the response of thick asphalt pavements to repetitive loading, while the controlled-strain approach is suitable for thin pavements (Yoder and Witczak, 1975; Tangella et al., 1990; Tayebali et al., 1994). The controlled strain mode of testing results in a greater fatigue life for the same mixture than the controlled stress testing.

It is the authors' belief that a true material model should be independent of the mode of loading because the material does not know which mode it is subjected to. That is, the material simply responds when it is loaded. A model of fatigue behavior that is independent of the mode of loading, which is neither controlled stress nor controlled strain, would be a substantial improvement over existing models, and would result in more realistic predictions of fatigue life of asphalt pavements.

CHAPTER 2: MATERIALS AND TESTING PROCEDURE

All specimens used in this study were fabricated using Watsonville granite aggregate and AAD and AAM asphalt cements used in the Strategic Highway Research Program (hereinafter, denoted as AAD and AAM mixtures, respectively). AAD asphalt (AR4000), which is from California Costal crude, has a tendency for age hardening and cracking. AAM asphalt (AC 20), which is from West Texas intermediate, was described as a good performer with a low temperature susceptibility and some potential for low temperature cracking (Cominsky et al., 1989). Basic properties of both asphalt cements are shown in Table 1.

Table 1. Summary of AAM and AAD Asphalt Properties (Moulthrop, 1990).

Asphalt	Viscosity of Original Binder		Viscosity After Rolling Thin Film Oven Aging		Penetration of Original Binder (100g/5 s, dmm)	
	60°C, Poise	135°C, cSt	60°C, Poise	135°C, cSt	25°C	4°C
AAD-1	1,055	309	3,420	511	135	9
AAM-1	1,992	569	3,947	744	64	4

Table 2. Medium Gradation for Watsonville Granite Aggregate

Sieve Size	% Passing	% Retained
1"	100	0
3/4"	95	5
1/2"	79	16
3/8"	67	12
#4	47	20
#8	33	14
#16	22	11
#30	14	8
#50	9	5
#100	5	4
#200	-	5

A medium aggregate gradation used in the SHRP A-003A study was selected for this study, and is shown in Table 2. Aggregates were mixed with 5.0 percent asphalt cement by weight of dry aggregate at 140°C for 4 minutes. The mixture was compacted in a rectangular mold at 116°C by a rolling wheel compactor and cured at room temperature for 2 days before coring 102-mm (4-in) diameter by 200-mm (8-in) height cylindrical specimens from the slab. The specimens were cored in a horizontal direction perpendicular to the compaction force, consistent with the direction of tensile stress and/or strain developed near the bottom of an AC layer in actual pavement systems. Both ends of each specimen were cut to produce 203-mm (8-in) height. The target air voids content of the specimens was 4 percent with a Dry-Without-Parafilm measurement procedure (Harvey, 1991). Detailed information on preparing specimens using the rolling wheel compaction method is given in Appendix A.

The rolling wheel compaction has been recognized as one of the best methods in simulating the filed compaction (Tangella et al., 1990). The major advantage of this method is that the orientation of aggregate particles and density of mixture can be made to closely simulate field compaction.

All tests were conducted in a uniaxial tension mode using a servo-hydraulic closed-loop testing machine. A gluing jig and a uniaxial testing apparatus were developed to provide precise alignment of a cylindrical specimen with respect to the loading axis to reduce eccentric stress concentration during testing. Creep and relaxation tests were performed at varying temperatures for the characterization of viscoelastic properties, whereas all the fatigue tests were conducted at 25°C. Test data were collected by a data-acquisition system with a multichannel 16-bit board. Displacements were measured in two different ways: one using two extensometers in the middle portion of the sample with a gauge length of 102-mm, and the other measuring between the top and bottom loading plates, which results in a 200-mm gauge length. A haversine wave with 0.1 second loading time was used in cyclic loading. Stresses and strains used in the analysis were nominal (average) values.

Several loading histories were used in this study for different purposes. These loading histories are discussed as follows:

1. constant-strain rate monotonic loading history with varying strain rates to evaluate the validity of the correspondence principle to account for rate-dependence of the material,
2. constant stress/strain amplitude cyclic loading histories without rest periods to evaluate the ability to model damage growth and hysteretic behavior of the material,
3. constant stress/strain amplitude cyclic loading histories with rest periods for modeling microdamage healing of the material, and

4. cyclic loading histories with multilevel stress/strain amplitudes and random durations of rest for the validation of the constitutive model developed in this study.

CHAPTER 3: CONSTITUTIVE THEORY

In modeling the hysteretic behavior of asphalt-aggregate mixtures under cyclic loading, the following constitutive factors are deemed important:

1. viscoelasticity of the matrix that causes hysteretic behavior under cyclic loading and relaxation during rest periods,
2. fatigue damage growth during cyclic loading,
3. healing during rest periods, and
4. temperature dependence of asphalt matrix.

Effects of temperature on the constitutive behavior can be included in viscoelastic material properties, such as creep compliance and relaxation modulus, using time-temperature superposition principle (Kim and Lee, 1995a). In this study, temperature effects are not considered because only one temperature is used in fatigue testing. The major difficulty in evaluating the effects of the remaining three factors arises from the fact that these mechanisms occur simultaneously under cyclic loading with rest periods.

The modeling approach taken in this study categorizes these constitutive factors into the following three components: (1) linear viscoelasticity, (2) fatigue damage, and (3) microdamage healing. As was defined earlier, microdamage healing includes all the mechanisms, except linear viscoelastic relaxation, contributing to the recovery of stiffness or strength during rest periods, such as fracture healing, steric hardening, nonlinear viscoelastic relaxation, etc. The correspondence principle using the pseudo-strain concept is used to eliminate the time-dependence of the material from the hysteretic stress-strain behavior. Then work potential theory, a continuum damage theory based on irreversible thermodynamics principles, is employed to model the damage and microdamage healing. In the following, theoretical and experimental studies on these two principles are presented.

Correspondence Principle

Theoretical Framework

Theory of viscoelasticity allows viscoelastic problems to be transformed so that they are mathematically equivalent to those for elastic problems with the substitution of elastic moduli. This correspondence can be made by taking appropriate transformation of the governing field and boundary equations of viscoelastic problems with respect to time. In general, the principle employs the Laplace transformation for linear viscoelastic materials.

Schapery (1984) proposed the extended elastic-viscoelastic correspondence principle (CP) which can be applicable to both linear and nonlinear viscoelastic materials.

He suggested that constitutive equations for certain viscoelastic media are identical to those for the elastic cases, but stresses and strains are not necessarily physical quantities in the viscoelastic body. Instead, they are pseudo variables in the form of convolution integrals such that:

$$\varepsilon_{ij}^{R} = \frac{1}{E_R}\int_0^t E(t-\tau)\frac{\partial \varepsilon_{ij}}{\partial \tau}\,d\tau \tag{2}$$

$$\sigma_{ij}^{R} = E_R\int_0^t D(t-\tau)\frac{\partial \sigma_{ij}}{\partial \tau}\,d\tau \tag{3}$$

where σ_{ij}, ε_{ij} = physical stresses and physical strains,
σ_{ij}^{R}, ε_{ij}^{R} = pseudo stresses and pseudo strains,
E_R = reference modulus that is an arbitrary constant, and
E(t), D(t) = relaxation modulus and creep compliance, respectively.

For the case of a growing traction boundary surface, such as crack growth, the viscoelastic problem can be reduced to an elastic case by using physical stresses and pseudo strains (Schapery 1984).

For linear viscoelastic materials, a uniaxial stress-strain relationship is:

$$\sigma = \int_0^t E(t-\tau)\frac{d\varepsilon}{d\tau}\,d\tau \tag{4}$$

Using the definition of pseudo strain in equation (2), equation (4) can be rewritten as:

$$\sigma = E_R\,\varepsilon^{R} \tag{5}$$

where $$\varepsilon^{R} = \frac{1}{E_R}\int_0^t E(t-\tau)\frac{\partial \varepsilon}{\partial \tau}\,d\tau \tag{6}$$

A correspondence can be found between equation (5) and a linear elastic stress-strain relationship. Calculation of pseudo strain using equation (6) requires the expression of relaxation modulus as a function of time. Details of developing an analytical representation of the relaxation modulus are given in Appendix B.

For nonlinear viscoelastic materials, the explicit form of the constitutive equation between stresses and pseudo strains is dependent on material type and loading geometry.

Therefore, experimental studies are essential to establish the analytical representation of the constitutive model for a material of interest.

Experimental Verification of CP

Prior to constitutive modeling, the material's behavior was studied with the application of the CP. The types of uniaxial tensile testing used in this task were as follows:

1. controlled-stress cyclic loading tests, and
2. constant-strain-rate monotonic loading tests with varying strain rates.

In the cyclic loading tests, a loading amplitude of 156 N (35 lb) was used, which was low enough not to induce any significant damage. Typical hysteretic stress-strain behavior is presented in Figure 3(a) at selected cycles. As expected, the stress-strain loops shift to the right-hand side with the reduction of dissipated energy determined from the area inside the stress-strain curve. In Figure 3(b), the same stresses are plotted against pseudo strains calculated based on equation (5). As can be seen from Figures 3(a) and 3(b), hysteretic behavior due to both loading-unloading and repetitive loading has disappeared using the pseudo strains, except the first cycle during which some minor adjustments occur within the test setup. It is also noted that the stress pseudo-strain behavior in Figure 3(b) is linear.

In the monotonic loading tests, four different strain rates ranging from 0.0001 to 0.0032 unit/second were used. Figure 4(a) displays the rate-dependent behavior observed from the AAD mixture. Pseudo strains were plotted against σ/I in Figure 4(b). The initial pseudo stiffness I, defined as the ratio of stress to pseudo-strain at the early linear part of a stress pseudo-strain curve, was necessary to account for the effect of sample-to-sample variability. The curves representing different loading rates fall on the same line at lower stress levels, and then the discrepancy in the stress pseudo-strain curves among the different loading rates becomes greater. This behavior implies that the CP can successfully eliminate the rate dependency of the material when the damage is negligible. However, if a significant level of damage is induced in the sample, additional variables should be employed in a constitutive equation to represent the damage growth in the system. Additional results on experimental verification of the CP are documented by Kim et al., (1995b) using uniaxial cyclic data of asphalt concrete under a wide range of test conditions.

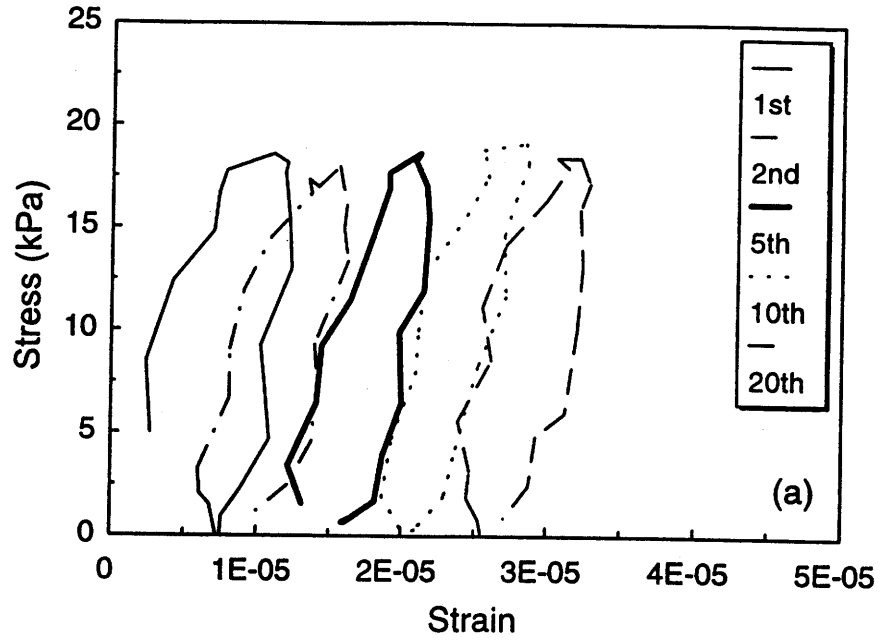

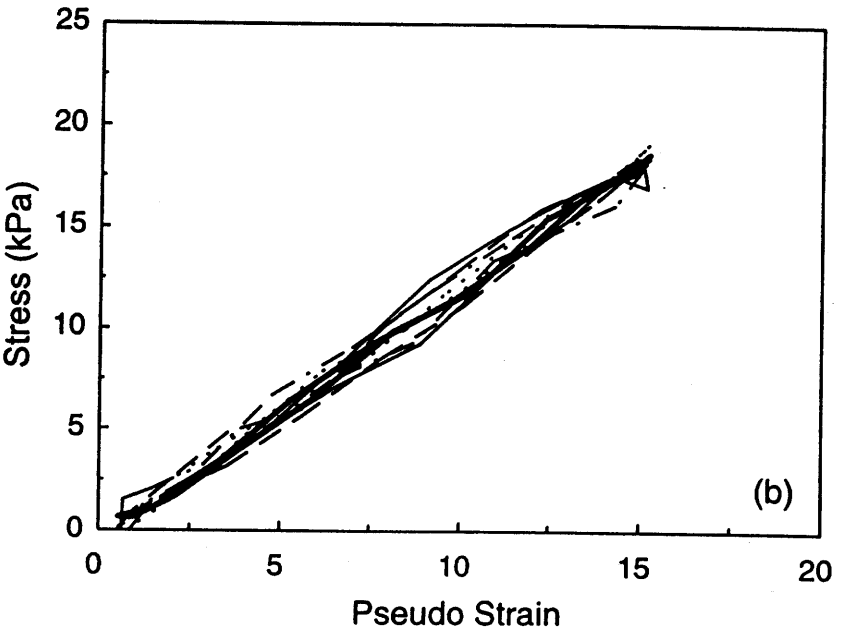

Figure 3. Application of CP to Cyclic Data with Negligible Damage: (a) Stress-Strain; (b) Stress-Pseudo Strain.

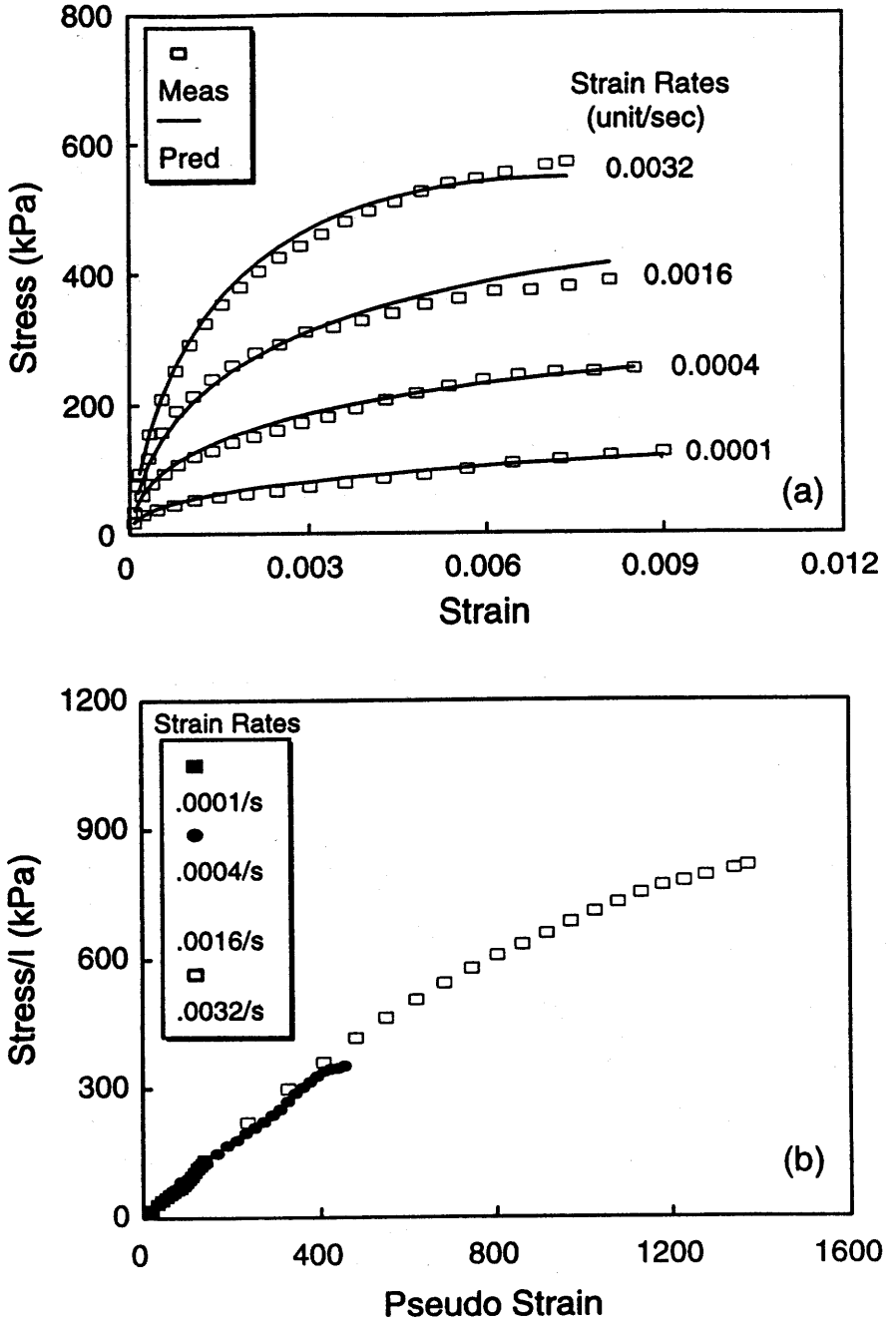

Figure 4. Application of CP to Monotonic Data: (a) Stress-Strain; (b) Stress-Pseudo Strain.

Work Potential Theory

In studying the constitutive behavior of a material with damage, two general approaches are usually considered: a micromechanical approach and a continuum approach. Brief descriptions of these approaches are made in Appendix B.

Schapery (1982, 1987, 1990, 1994) has developed a series of viscoelastic damage models for particulate and fiber-reinforced composites. His models are based on his other works on viscoelastic fracture mechanics (Schapery, 1984, 1975), and have further evolved in combination with his micromechanical model (Schapery, 1986) and work potential theory (Schapery, 1990). The work potential theory applied to viscoelastic media is composed of the following three elements:

1. *Pseudo strain energy density function:* A pseudo strain energy function exists in the following form:

$$W^R = W^R(\varepsilon^R, S_m) \tag{7}$$

where S_m are internal state variables (or damage parameters) representing structural changes in the material (e.g., damage, healing, etc.).

2. *Stress-strain relationship:* The pseudo-strain energy function has the following property:

$$\sigma = \frac{\partial W_R}{\partial \varepsilon^R} \tag{8}$$

3. *Damage evolution law:* Damage evolution in the material is governed by the following:

$$\dot{S}_m = \left(-\frac{\partial W^R}{\partial S_m}\right)^{\alpha_m} \tag{9}$$

where S_m overdot is the damage evolution rate, and α_m are material constants. Equation (9) is similar to the crack propagation rate equation.

The work potential theory has been applied by Park and Schapery (1994, 1996) in characterizing the mechanical behavior of particle-filled elastomers under axial extension and hydrostatic pressure. Park et al. (1996) also adopted the work potential theory in

modeling the rate-dependent behavior of asphalt-aggregate mixtures under constant-strain-rate monotonic loading. More information on the work potential theory can be found in Appendix B.

Damage and Microdamage Healing

In fracture mechanics, how the constitutive behavior changes as a function of crack length is a major concern; whereas, in continuum damage mechanics, it is how the constitutive behavior changes as a function of any microstructural changes that forms the basis of this system. That is, in continuum damage mechanics, the damaged body is represented as a homogeneous continuum on a scale that is much larger than the flaw sizes. The state of damage is quantified by internal state variables and the growth of damage is governed by an appropriate damage evolution law (Kim et al., 1997).

It is important to note that the term *damage* in continuum damage mechanics is defined as any structural changes in a system. Its definition and formulation are general enough for continuum damage mechanics principles to be applicable not only to deleterious structural changes (such as microcrack propagation and coalescence, void growth, plastic flows, shear banding, etc.), but also to beneficial changes (such as fracture healing, nonlinear viscoelastic relaxation, etc.). Depending on the number and nature of governing mechanisms of the material under the load, an appropriate number of internal state variables (S_m) are used for describing the constitutive behavior.

We will take full advantage of the generality that continuum damage mechanics provides by applying the work potential theory to modeling both the fatigue process during loading and the recovery process during rest. However, since the term damage is commonly considered a deleterious process in pavement engineering, in this report, we will define the term damage as all structural changes in a material contributing to the reduction of its stiffness or strength during loading except the ones represented by linear viscoelasticity. Then, *microdamage healing* is defined to include all mechanisms except linear viscoelastic relaxation contributing to the recovery of stiffness or strength during rest periods (e.g., fracture healing, steric hardening, nonlinear viscoelastic relaxation, etc). Therefore, in this study, the work potential theory, one of the continuum damage mechanics principles, is applied to modeling both damage and microdamage healing.

Internal State Variable Formulation

Using the internal state variable (ISV) formulation, the following form of constitutive relationship for asphaltic materials was proposed by Kim and Little (1990):

$$\sigma_{ij} = \sigma_{ij}(\varepsilon_{kl}, t, T, \frac{\partial T}{\partial x_n}, S_m) \tag{10}$$

where σ_{ij} = stresses in a body; $\epsilon_{kl} = \epsilon_{kl}(x_n, t)$ = strains in a body; t = time elapsed from the first application of loading; T = temperature; T/x_n = spatial temperature gradients in a body; S_m = internal state variables; i,j,k,l,n = 1, 2, 3; and m = 1, 2, 3, ..., M. Assuming that the temperature is constant spatially and the pseudo strain accounts for all the viscoelastic hereditary effects of the material associated with a given strain history, equation (10) reduces to:

$$\sigma_{ij} = \sigma_{ij}(\varepsilon^R_{kl}, T, S_m) \tag{11}$$

In this study, only the uniaxial case with constant temperature is considered; therefore, equation (11) reduces to:

$$\sigma = \sigma(\varepsilon^R, S_m) \tag{12}$$

In order to identify the basic structure of equation (12), the following uniaxial version of constitutive equations for linear elastic and linear viscoelastic bodies without and with damage is presented. They also show how models of different complexity may evolve from simpler ones.

Elastic Body without Damage:	$\sigma = E_R \varepsilon$	(13)
Elastic Body with Damage:	$\sigma = C(S_m) \varepsilon$	(14)
Viscoelastic Body without Damage:	$\sigma = E_R \varepsilon^R$	(15)
Viscoelastic Body with Damage:	$\sigma = C(S_m) \varepsilon^R$	(16)

where E_R is a constant and $C(S_m)$ indicates that C is a function of internal state variables (or damage parameters) S_m. E_R in equation (13) is Young's modulus. The function $C(S_m)$ represents the changing *stiffness* of the material due to changes in microstructure of the material, e.g., growing damage or healing. It is seen that equations (15) and (16) take the form of equations (13) and (14), respectively; i.e., a useful elastic-viscoelastic correspondence exists between the two sets of equations. This observation is supported by the CP described earlier, and therefore, the viscoelastic behavior can be described by the elastic equations with physical variables replaced by corresponding pseudo variables. The form of equation (16) is also supported by the observations made earlier from monotonic loading data in Figure 4 that, when the induced damage is negligible, the material behaves like a linear elastic material with the substitution of strain with pseudo strain and that the stiffness changes as damage grows.

Equation (16) is a more specific version of the stress-strain relationship in equation (8) and allows one to obtain the following expression for the pseudo-strain energy density function:

$$W^R = \frac{1}{2} C(S_m) (\varepsilon^R)^2 + f(S_m) \tag{17}$$

Using the initial condition (i.e., $W^R = 0$ when $\varepsilon^R = 0$), one can obtain that $f(S_m) = 0$. Equations, (7), (8), and (17) constitute the mechanical behavior of the viscoelastic materials with growing damage and other structural changes.

CHAPTER 4: EXPERIMENTAL APPROACH TO CONSTITUTIVE MODELING

Based on the above formulation, constitutive modeling of asphalt concrete under cyclic loading boils down to determination of the explicit form of $C(S_m)$ in equation (16) using the damage evolution law (equation 9) that accounts for damage growth during loading and microdamage healing during rest periods. In order to obtain necessary experimental data for this task, two types of tests were performed:

1. constant stress/strain amplitude cyclic tests without rest periods; and
2. constant stress/strain amplitude cyclic tests with seven different rest periods varying from 0.5 second to 32 minutes.

The explicit form of the constitutive equation was developed using the experimental data obtained from the test series 1. This constitutive equation was then extended to account for the microdamage healing occurring during rest periods using the data collected from the test series 2.

Using the constitutive theories described in the preceding section and experimental data obtained from monotonic and cyclic tests on asphalt concrete, a uniaxial constitutive model that accounts for the effects of rate of loading, strain level dependency, rest periods, and mode of loading is developed. The basic approach taken in the modeling is to eliminate the hysteretic behavior due to linear viscoelasticity using pseudo-strain and to analytically represent the damage and microdamage healing by means of the work potential theory.

Once the time-dependence of the material due to linear viscoelasticity is taken care of using the pseudo strain, the stress pseudo-strain behavior reveals the following three important characteristics of damage incurred in the specimens:

1. nonlinear behavior of the loading and unloading paths in each cycle,
2. change in the slope of each σ-ε^R cycle as cyclic loading continues, and
3. accumulation of permanent pseudo-strain in the controlled-strain mode (i.e., shift of the loop from the origin as cyclic loading continues).

The first two characteristics are observed in both modes of loading, while the third characteristic is unique to the controlled-stress mode.

A single parameter, secant pseudo stiffness S^R (hereinafter called pseudo stiffness for simplicity), can be used to represent the change in the slope of loops in both modes of loading and defined as follows:

$$S^R = \frac{\sigma_m}{\epsilon_m^R} \tag{18}$$

where $\epsilon_m{}^R$ is the peak pseudo strain in each stress pseudo-strain cycle, and σ_m is a stress corresponding to $\epsilon_m{}^R$.

Figure 5 presents typical stress pseudo-strain plots and pseudo stiffness in controlled-strain and controlled-stress fatigue tests. Since S^R is determined from stress and pseudo-strain values, instead of physical strain, the advantage of using pseudo strain, that is, eliminating the time-dependence from the hysteretic behavior, is still effective. Thus, the change in S^R represents damage growth and healing separately from the time-dependence, which allows a simple function of S^R to describe these mechanisms under complicated loading histories.

Analytical details involved in developing the final model can be found in Appendix B. Only important observations necessary to highlight the physical implications of the model are discussed.

The resulting constitutive model of asphalt-aggregate mixtures that accounts for damage growth and healing is:

$$\sigma = I\,(\epsilon_e^R)\,[F + G + H] \tag{19}$$

where

I = initial pseudo-stiffness,
$\epsilon_e{}^R$ = $\epsilon^R - \epsilon_S{}^R$ = effective pseudo-strain,
$\epsilon_S{}^R$ = the shift in ϵ^R representing accumulated permanent deformation in each stress pseudo-strain cycle under the controlled-stress mode,
F = the damage function representing the change in the slope of each σ-ϵ^R loop,
G = the hysteresis function representing the difference between loading and unloading paths, and
H = the healing function representing the change in secant pseudo stiffness due to rest periods.

The initial pseudo stiffness I was employed to account for the sample-to-sample stiffness variation. The reason for using $\epsilon_e{}^R$ in equation (19) is to account for the difference in fatigue mechanisms between controlled-strain and controlled-stress modes. In addition to fatigue cracking, permanent pseudo strain ($\epsilon_S{}^R$ in Figure 5) is accumulated in the material after each cycle under controlled-stress mode. To develop a universal

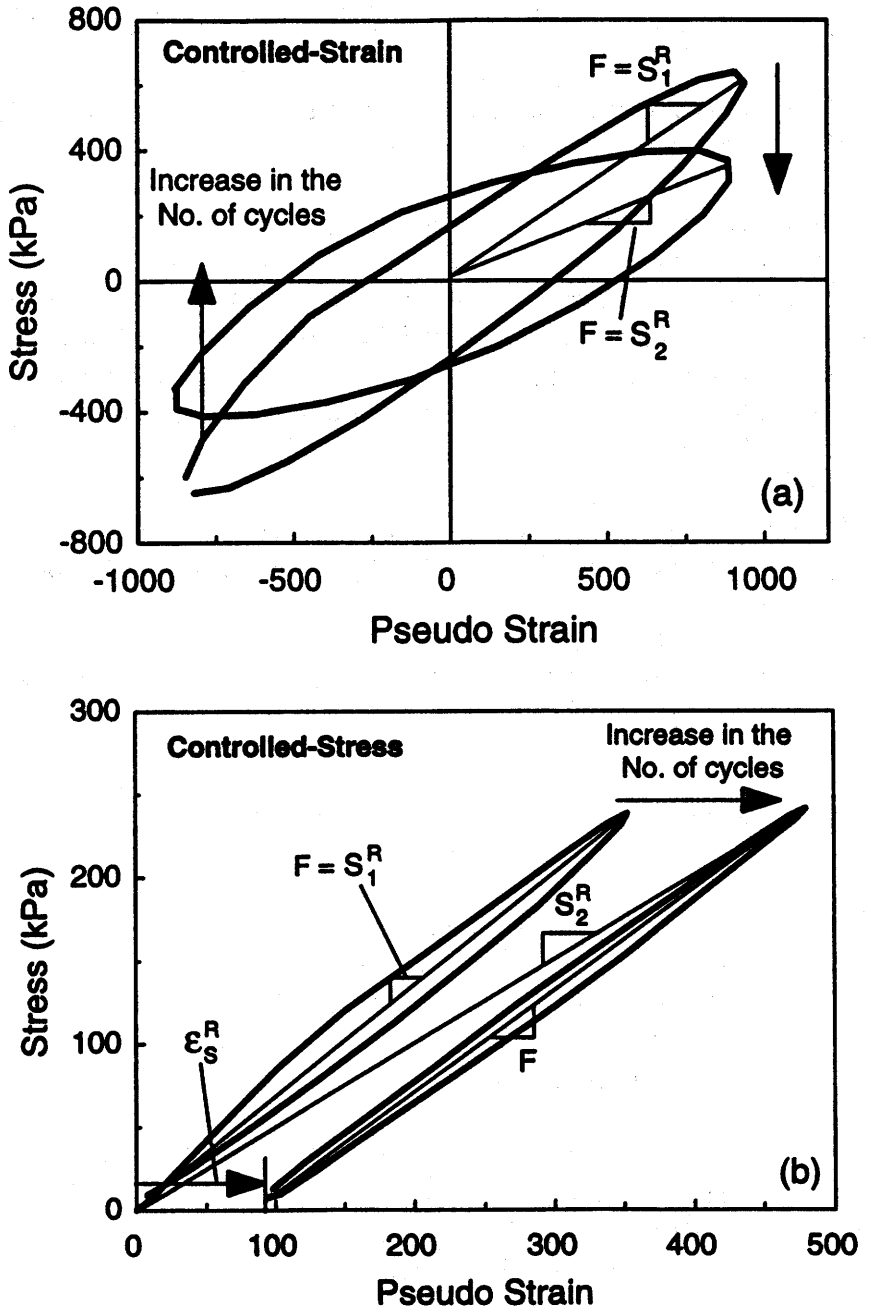

Figure 5. Stress Pseudo-Strain Behavior and Pseudo-Stiffness Changes in: (a) Controlled-Strain Mode; (b) Controlled-Stress Mode.

model that can describe the constitutive behavior of both control modes using the same model coefficients, effective pseudo strain (ϵ_e^R) is used in equation (19). Equation (19) also suggests that $C(S_m)$ in equation (16) is composed of the three functions, F, G, and H, where the functions F and H characterize the changes in S^R due to damage growth and healing, respectively, and the function G accounts for the difference in stress values between loading and unloading paths as shown in Figure 5. Brief discussions of these functions are given in the following sections.

The Damage Function F

To illustrate the change in S^R as damage grows, S^R values normalized by the initial pseudo-stiffness (I) in the controlled-strain cyclic test without rest are plotted against the number of cycles (N) in Figure 6. Since the function C_1 represents the pseudo-stiffness of the material, the decreasing trend of C_1 with increasing N in Figure 6 is expected. It can be also seen that the pseudo stiffness decreases (i.e., damage increases) more rapidly with a higher strain amplitude than a lower strain amplitude. Figure 7 depicts how the damage parameter S_1 grows as N increases. For the same value of N, the higher strain amplitude induces more damage than the lower strain amplitudes, and thus the larger S_1 values.

Figures 6 and 7 demonstrate the strain-level dependency of the function C_1 and the damage parameter S_1. The C_1 and S_1 values for the same N values are cross-plotted in Figure 8. Three curves representing different strain levels fall atop each other, demonstrating the strain-level-independence of the C_1-S_1 relationship.

The explicit form of the function F was established using the geometrical relationship between F and S^R in Figure 5(b):

$$F = \left(\frac{\epsilon_m^R}{\epsilon_m^R - \epsilon_s^R}\right) C_1(S_{1n}) \tag{20}$$

where $C_1(S_{1n}) = C_{10} - C_{11}(S_{1n})^{C_{12}}$,

ϵ_m^R = peak pseudo-strain in each stress pseudo-strain cycle,
$S_{1n} = S_1/S_{1f}$ = normalized damage parameter,
S_{1f} = a value of damage parameter S_1 at failure, and
C_{10}, C_{11}, C_{12} = regression coefficients.

The function F represents the change in the slope of stress pseudo-strain loop in the both modes of loading and is composed of two parts, $C_1(S_{1n})$ and the correction factor $\epsilon_m^R/(\epsilon_m^R - \epsilon_s^R)$. Tthe function $C_1(S_{1n})$ represents the change in S^R under a continuous cyclic loading without rest periods. The correction factor in front of $C_1(S_{1n})$ is simply a

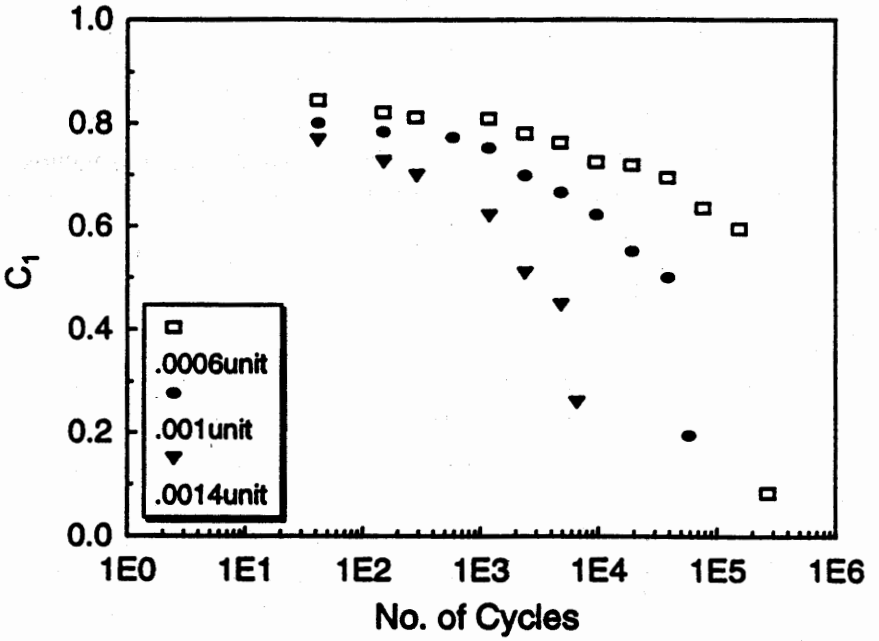

Figure 6. Change in Pseudo-Stiffness C_1 as the Number of Cycles Increase.

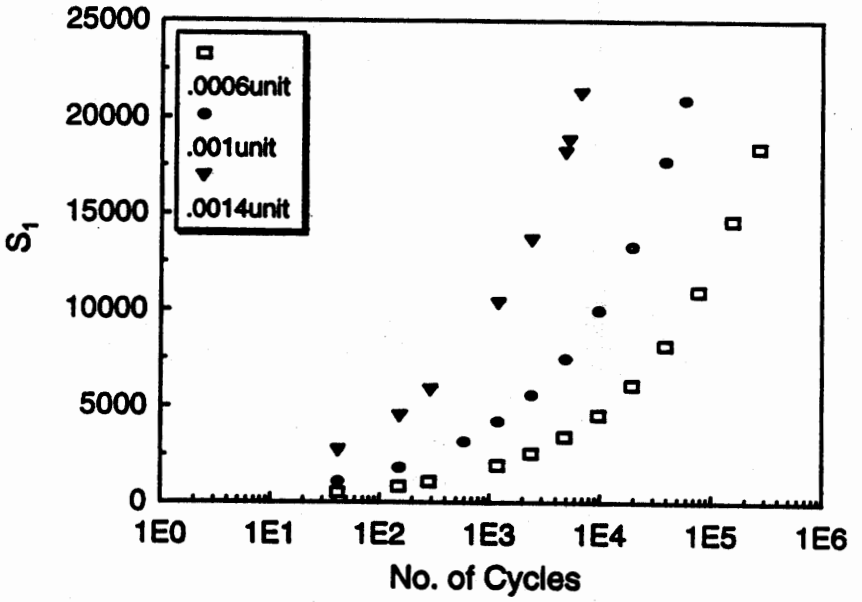

Figure 7. Change in Damage Parameter S_1 as the Number of Cycles Increases.

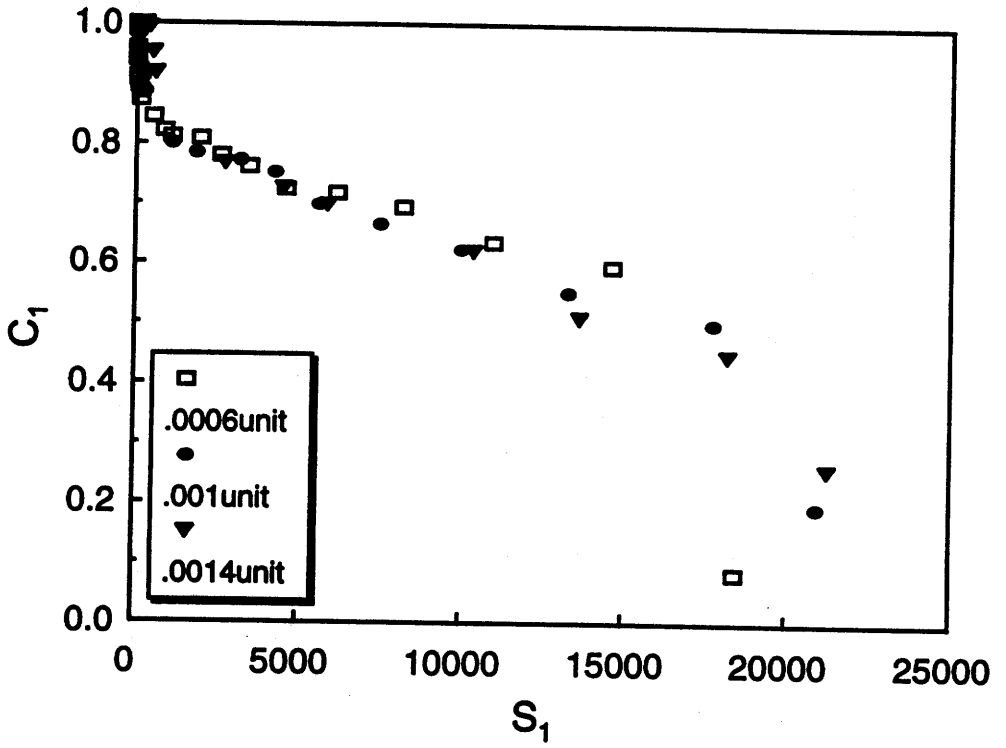

Figure 8. Relationship Between C_1 and S_1.

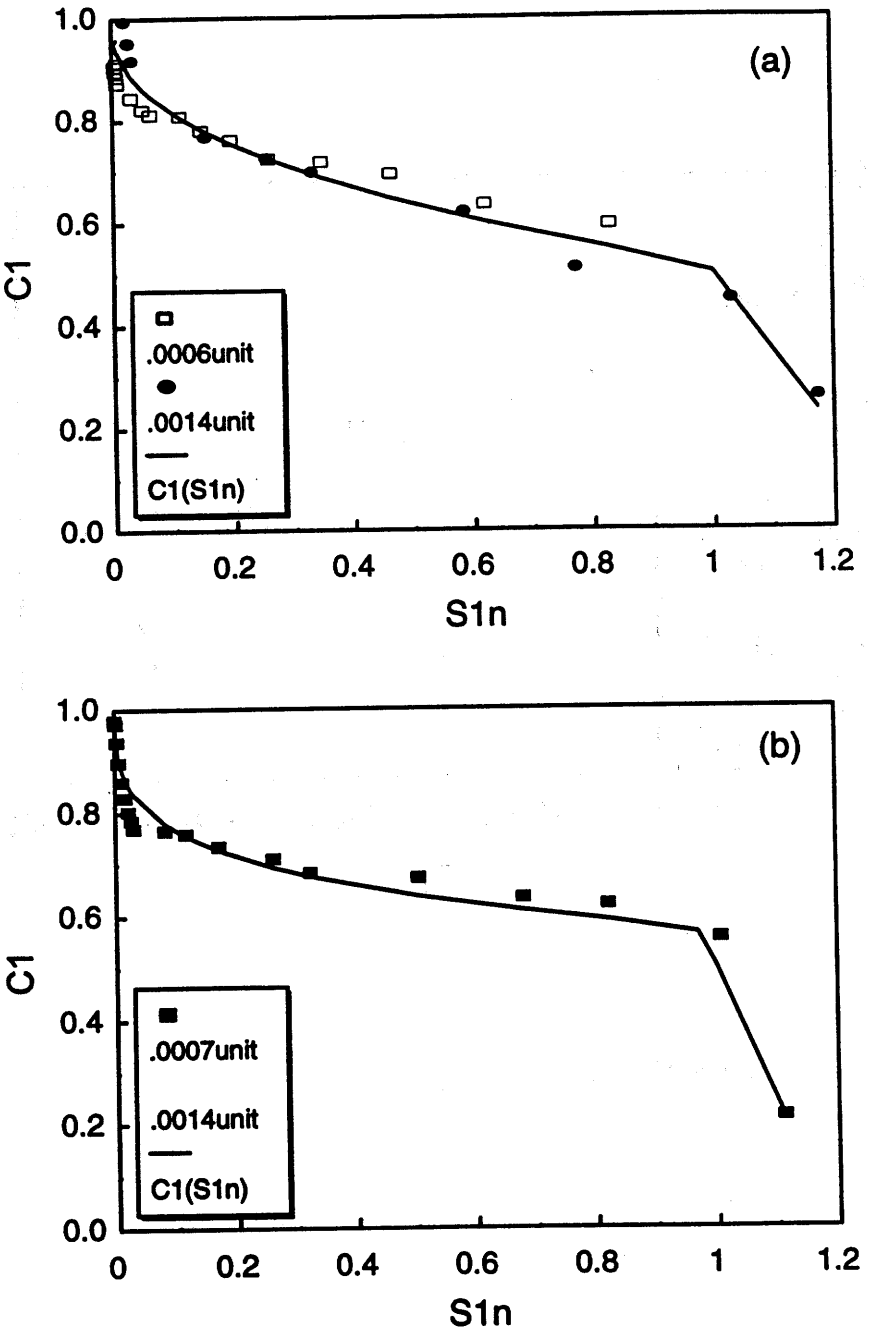

Figure 9. Change in Normalized Pseudo-Stiffness as Damage Grows: (a) AAD Mixture; (b) AAM Mixture.

geometric factor that is necessary to represent the slope of each stress pseudo-strain loop using a single expression for both modes of loading. Normalized damage parameter S_{1n} was used to account for the difference in the values of damage parameter at failure S_{1f} between two modes of loading. Figure 9 shows C_1-S_{1n} behavior of AAD and AAM mixtures under the controlled-strain mode.

The Hysteresis Function G

Although the damage function F characterizes the change in pseudo stiffness from one cycle to the next, modeling the hysteretic stress pseudo-strain loop in each cycle requires an additional function representing the difference between loading and unloading paths. As can be seen from the loading and unloading curves in Figure 5, there are two different stresses associated with one ϵ^R value in each cycle when damage is present. On the loading path, the stress is a function of current ϵ^R only, while on the unloading path, the stress is a function of current ϵ^R and the largest ϵ^R during the ϵ^R history up to that time (ϵ_L^R). This observation suggests the use of ϵ^R/ϵ_L^R in identifying whether the point of interest is on the loading path or on the unloading path (Kim and Little, 1990), that is, $\epsilon^R/\epsilon_L^R = 1$ during the loading path, and $\epsilon^R/\epsilon_L^R < 1$ during the unloading path. Using the experimental data, it was found that the following function can characterize the hysteretic stress pseudo-strain behavior under cyclic loading:

$$G = G_0 + G_1 \left| \frac{\epsilon^R}{\epsilon_L^R} \right|^{G_2(\epsilon_0^R)} \tag{21}$$

where $G_2(\epsilon_0^R) = G_{2R}\left(\beta_0 + \frac{\beta_1}{\epsilon_0^R}\right)$,

ϵ_0^R = amplitude of pseudo strain, and
G_{2R}, β_0, β_1 = regression coefficients.

It is noted here that the hysteresis function G is necessary to accurately describe the stress-strain behavior of both loading and unloading paths; however, when only peak stress and strain values of each cycle are of concern (e.g., in the case of predicting fatigue life of the material), the function G can be omitted, which makes the model simpler and more practical.

The Healing Function H

The function H was used to represent the change in S^R due to rest periods. A typical trend of S^R before and after a rest period is shown in Figure 10. In this figure, the curve OBCD represents the reduction in S^R due to damage growth for the case without a rest period (i.e., $C_1(S_{1n})$), and the curve AB′D′ depicts the reduction in S^R due to damage

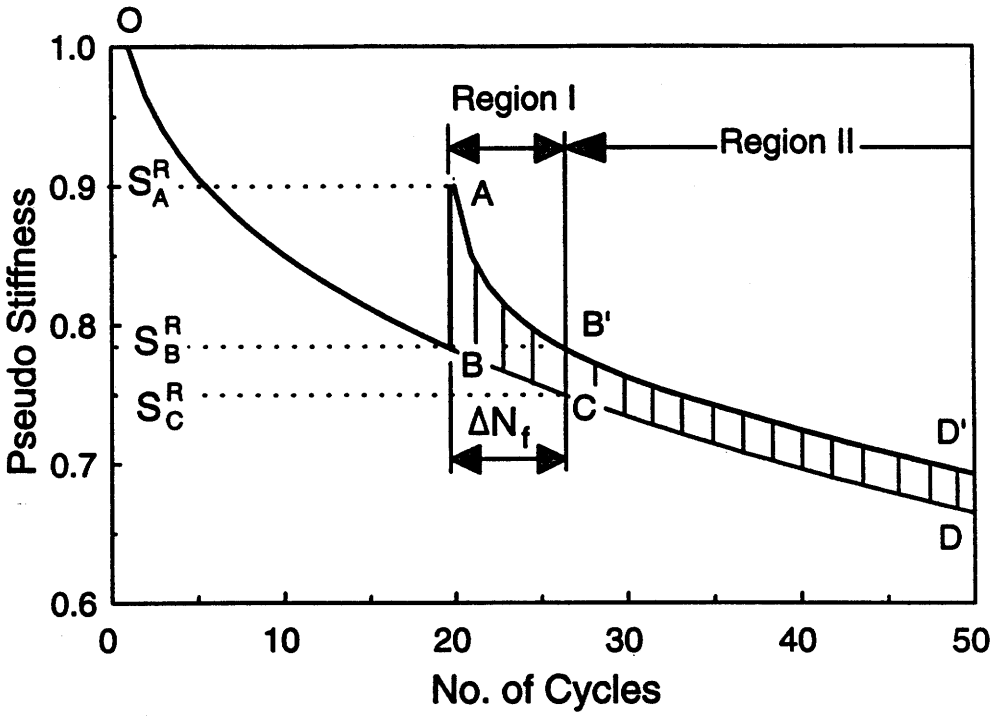

Figure 10. Change in Pseudo Stiffness Before and After a Rest Period.

Table 3. A Viscoelastic Continuum Model of Asphalt Concrete with Microdamage Healing

$$\sigma = I(\epsilon_e^R)[F + G + H]$$

where

I = initial pseudo stiffness,

ϵ_e^R = $\epsilon^R - \epsilon_S^R$ = effective pseudo strain,

$$F = \left(\frac{\epsilon_m^R}{\epsilon_m^R - \epsilon_s^R}\right) C_1(S_{1n})$$

$$G = G_0 + G_1 \left|\frac{\epsilon^R}{\epsilon_L^R}\right|^{G_2(\epsilon_0^R)}$$

$$H = [S_{B,i}^R + C_2(S_2)]C_3(S_3) - C_1(S_{1n}) - \sum_{j=1}^{i-1}(S_{B,j}^R - S_{C,j}^R) \quad when\ S^R > S_{B,i}^R\ (Region\ I)$$

or

$$H = \sum_{j=1}^{i}(S_{B,j}^R - S_{C,j}^R) \quad when\ S^R < S_{B,i}^R\ (Region\ II)$$

$$C_1(S_{1n}) = C_{10} - C_{11}(S_{1n})^{C_{12}}$$

$$C_2(S_2) = C_{20} - C_{21}(S_2)^{C_{22}}$$

$$C_3(S_3) = C_{30} - C_{31}(S_3)^{C_{32}}$$

$$G_2(\epsilon_0^R) = G_{2R}\left(\beta_0 + \frac{\beta_1}{\epsilon_0^R}\right)$$

$$S_{1(i=N)} \cong \sum_{i=1}^{N}\left[\frac{I}{2}(\epsilon_{mi}^R)^2(C_{1(i-1)} - C_{1(i)})\right]^{\frac{\alpha_1}{(1+\alpha_1)}}(t_1 - t_{i-1})^{\frac{1}{(1+\alpha_1)}}$$

$$S_{2(i)} \cong \left[\frac{I}{2}(\epsilon_{m(i)}^R)^2(S_A^R - S_B^R)\right]^{\frac{\alpha_2}{(1+\alpha_2)}} t_{RP(i)}^{\frac{1}{(1+\alpha_2)}}$$

$$S_{3(i=N)} \cong \sum_{i=1}^{N}\left[\frac{IS_A^R}{2}(\epsilon_{mi}^R)^2(C_{3(i-1)} - C_{3(i)}\right]^{\frac{\alpha_3}{(1+\alpha_3)}}(t_i - t_{i-1})^{\frac{1}{(1+\alpha_3)}}$$

C_{ij} = regression coefficients,

α_i = internal state evolution rates,

Table 3. Continued

G_{2R}, β_0, $\beta 1$=		regression coefficients,
$t_{RP(i)}$	=	duration of the i^{th} rest period,
$\epsilon^R_{m(i)}$	=	peak pseudo strain right before the i^{th} rest period,
ϵ^R_e	=	the shift in ϵ^R representing accumulated permanent deformation in each stress pseudo-strain cycle under the controlled-stress mode,
ϵ^R_0	=	amplitude of pseudo strain,
S_{1n}	=	normalized damage parameter (i.e., S_1/S_{1f}),
S_{1f}	=	a value of damage parameter S_1 at failure,
$S^R_{A,i}$	=	pseudo stiffness immediately after the i^{th} rest period,
$S^R_{B,i}$	=	pseudo stiffness immediately before the i^{th} rest period, and
$S^R_{C,i}$	=	pseudo stiffness without rest period at the point when S^R is equal to $S_B{}^R$ for the case with a rest period.

growth after the rest period. S^R has increased from point B to point A after the rest period due to the microdamage healing, and then it decreases as the loading continues after the rest. The beneficial effect of rest period diminishes gradually in Region I, and eventually in Region II, the slope of the curve B′D′ is the same as that of the curve CD but the position of the curve has shifted vertically by ($S_B{}^R$ - $S_C{}^R$). Based on this observation, it can be concluded that the curve AB′ and the curve B′D′ represent re-establishment of damage in the healed zone and damage growth in virgin material, respectively.

Accurate modeling of the changes in S^R during and after rest periods requires two internal state variables: one for the increase of S^R during rest periods due to microdamage healing (S_2) and the other for the reduction in S^R after rest periods due to damage evolution (S_3). A careful study of the experimental data resulted in the following equation for the healing function H:

$$H = [S^R_{B,i} + C_2(S_2)]C_3(S_3) - C_1(S_{1n}) - \sum_{j=1}^{i-1}(S^R_{B,j} - S^R_{C,j}) \quad when\ S^R > S^R_{B,i}\ (Region\ I)$$

or

$$H = \sum_{j=1}^{i} (S_{B,j}^{R} - S_{C,j}^{R}) \quad when\ S^{R} < S_{B,i}^{R}\ (Region\ II) \tag{22}$$

where $S_{B,i}^{R}$ = S^R before the i^{th} rest period,
$S_{C,i}^{R}$ = S^R without rest period at the point when S^R is equal to S_B^R for the case with a rest period,
$C_2(S_2) = C_{20} + C_{21}(S_2)^{C_{22}}$ = a function representing the increase of S^R during rest periods due to microdamage healing, and
$C_3(S_3) = C_{30} - C_{31}(S_3)^{C_{32}}$ = a function representing the reduction in S^R after rest periods due to damage evolution.

The recovery of S^R during the rest period is represented by the function C_2 (i.e., $(S_A^R - S_B^R)$ in equation (22), while the function C_3 (i.e., S^R/S_A^R) represents the reduction in S^R due to damage re-evolution in the healed material after the rest period. The relationship between C_2 and S_2 and C_3 and S_3 is presented in Figure 11.

The most general form of the constitutive model proposed in this study is summarized in Table 3 with descriptions of all the parameters employed in the model.

Model Coefficients for AAD and AAM Mixtures

According to the model described above, the constitutive behavior of asphalt-aggregate mixtures is mainly dependent on the three internal state functions, $C_1(S_{1n})$, $C_2(S_2)$, and $C_3(S_3)$. The coefficients of these functions for AAD and AAM mixtures are summarized in Table 4.

Some observations are made on the internal state functions using the model coefficients summarized in Table 4. The ISV functions C_1 and C_3 represent the damage growth in virgin materials and healed materials, respectively. The coefficients of C_1 and C_3 are similar. The coefficients C_{10} and C_{30} are close to 1 simply because the functions C_1 and C_3 are determined by normalizing S^R by the initial S^R value. The AAD mixture has a smaller C_{11} and larger C_{12} values than the AAM mixture, indicating slower decrease in C_1 at very early cycles but overall faster reduction of C_1. This trend is well displayed in Figure 9.

Another observation based on table 4 data is the difference in C_{21} and C_{22} values between AAD and AAM mixtures. The AAD mixture has a smaller value of C_{22} and a larger value of C_{21} than the AAM mixture, indicating the AAD mixture's ability to heal quicker in short rest durations and the AAM mixture's strength in continuous healing over long rest duration.

In order to determine which mixture has higher microdamage healing potential, one needs to examine both C_2 and C_3 functions. That is, it is important to know not only how much increase in S^R has occurred during a certain duration of rest (C_2 function), but also the rate of damage after the rest (C_3 function).

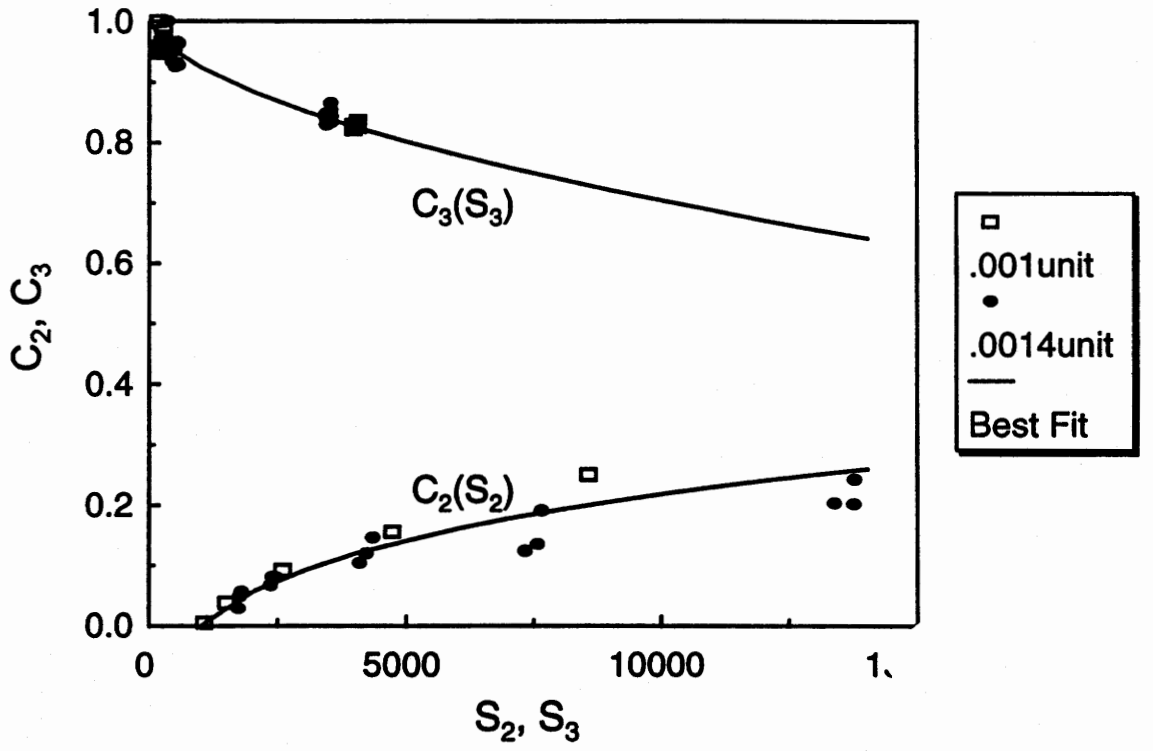

Figure 11. Increase in Pseudo Stiffness During Rest Period $C_2(S_2)$, and Re-evolution of Damage after Rest Periods $C_3(S_3)$.

CHAPTER 5: VALIDATION OF THE CONSTITUTIVE MODEL

For verification purposes, cyclic loading tests with random durations of rest under multi-level stress/strain amplitudes were performed on both mixtures. The strain and stress histories used in the controlled-strain and -stress tests are illustrated in Figures 12(a) and 12(b), respectively. Also, the constitutive model was applied to constant-strain-rate monotonic tests of varying strain rates on AAD mixtures. Stresses in all the verification studies were calculated using the constitutive equation (19), individual functions (20) through (22), and the model coefficients tabulated in Table 4. Strain values measured throughout the testing were used in the calculation of pseudo strains. Figure 4 presents

Table 4. Model Coefficients for AAD and AAM Mixtures.

Mix	C_{10}	C_{11}	C_{12}	C_{20}	C_{21}	C_{22}	C_{30}	C_{31}	C_{32}
AAD	0.99	0.489	0.44	-0.375	0.0941	0.20	1.01	0.0019	0.55
AAM	1.10	0.530	0.20	0.0015	0.0004	0.62	1.01	0.0114	0.30

the validation results for the monotonic tests. Figures 13 and 14 present the validation results from the controlled-strain cyclic tests of AAD mixture, and Figures 15 and 16 for the controlled-stress cyclic tests of AAM mixtures.

Constant-Strain-Rate Monotonic Tests

In general, a good agreement is found between the predicted and the measured stresses regardless of strain rate used (Figure 4). The satisfactory prediction of the monotonic behavior using the model developed from the cyclic tests demonstrates the model's versatility due to its basis on fundamental principles and parameters employed in this study. Also, the model accurately predicted rate-dependent stress-strain behavior of asphalt concrete.

Controlled-Strain Cyclic Test

Four different strain amplitudes between 0.0008 unit and 0.0015 unit were used in this validation. In order to verify that the constitutive model is independent of strain amplitude, the strain amplitudes that were not used in the characterization of the constitutive model were selected. Also, five different lengths of rest periods, which were not used in the characterization of the constitutive model between 50 and 800 seconds, were selected for the validation study. Sequences of both strain amplitudes and rest periods were random. The strain history used in this test was composed of eight groups of strain applications as shown in Figure 12(a). The last loading group (Group 8) was

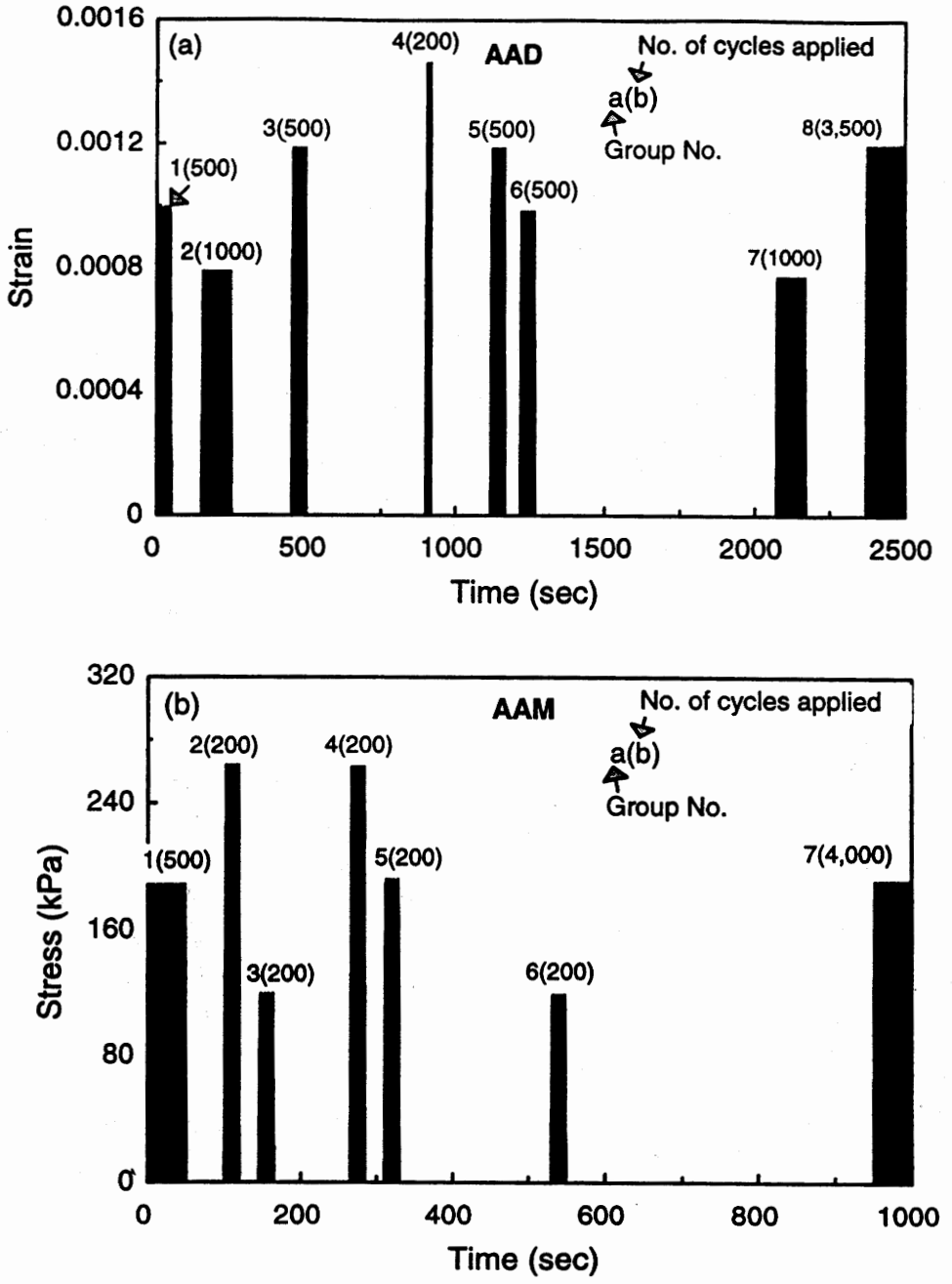

Figure 12. Validation Loading Histories: (a) Controlled-Strain Mode; (b) Controlled-Stress Mode.

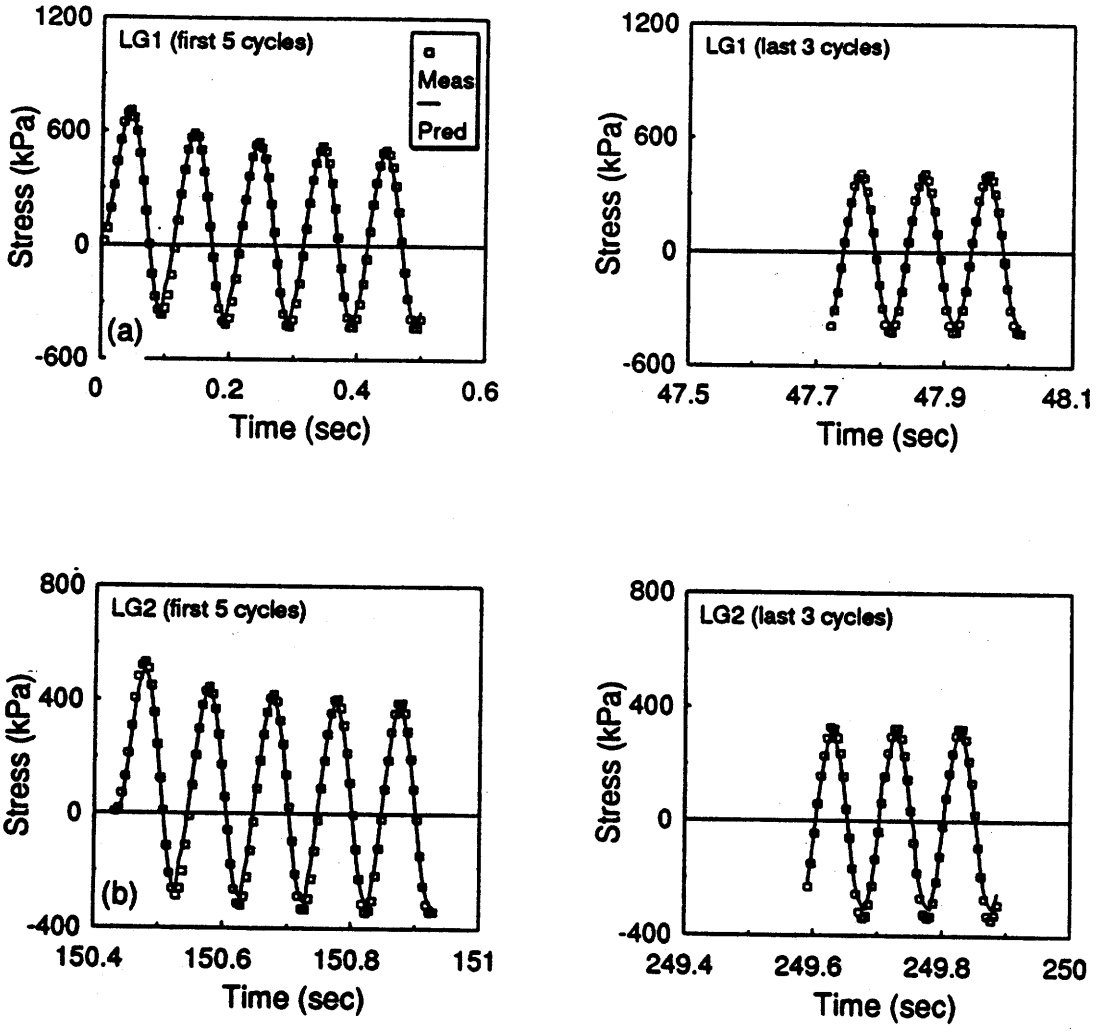

Figure 13. Prediction of Stresses for Different Loading Groups in the Controlled-Strain Validation History for AAD Mixture: (a) Loading Group 1; (b) Loading Group 2; (c) Loading Group 4; (d) Loading Group 8.

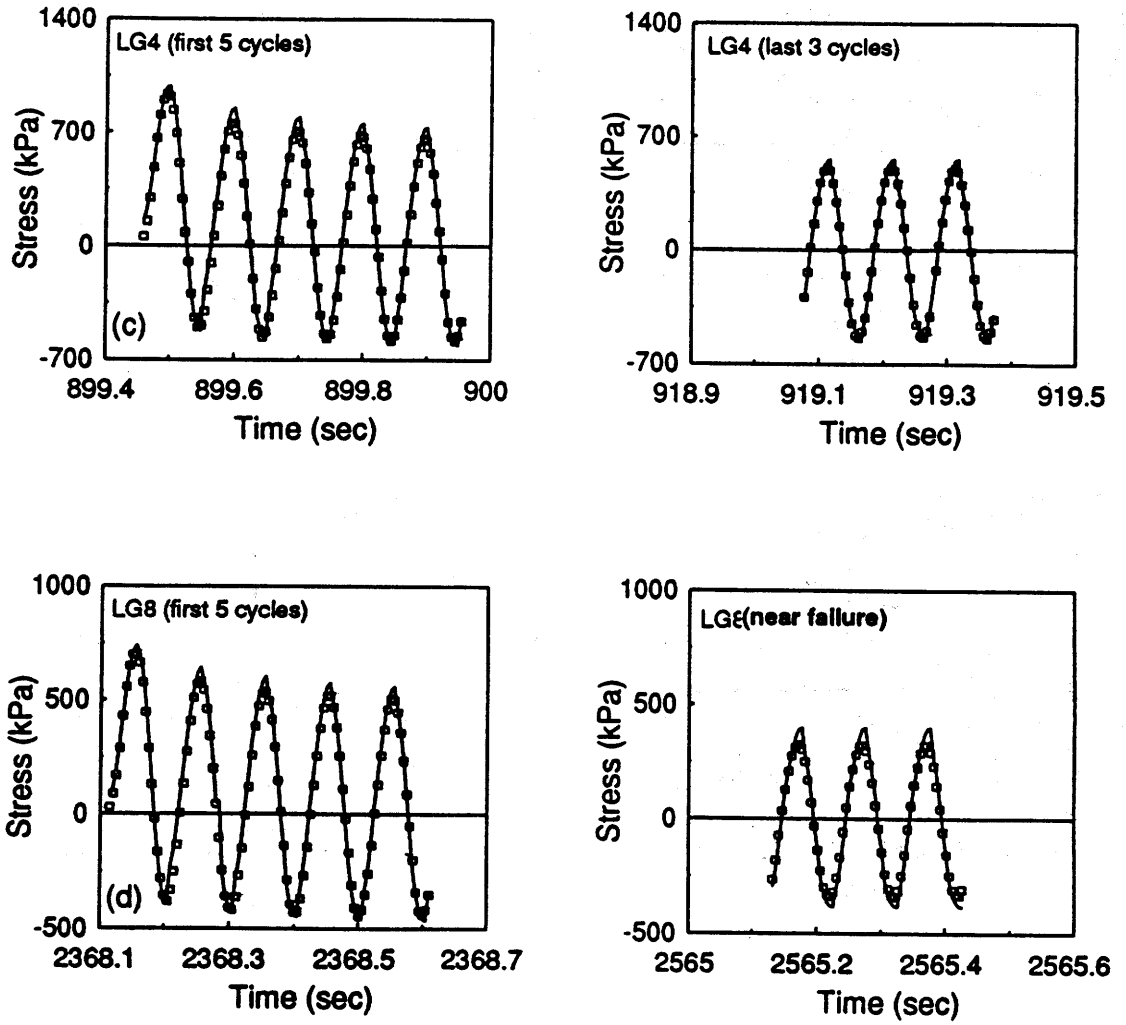

Figure 13. Continued

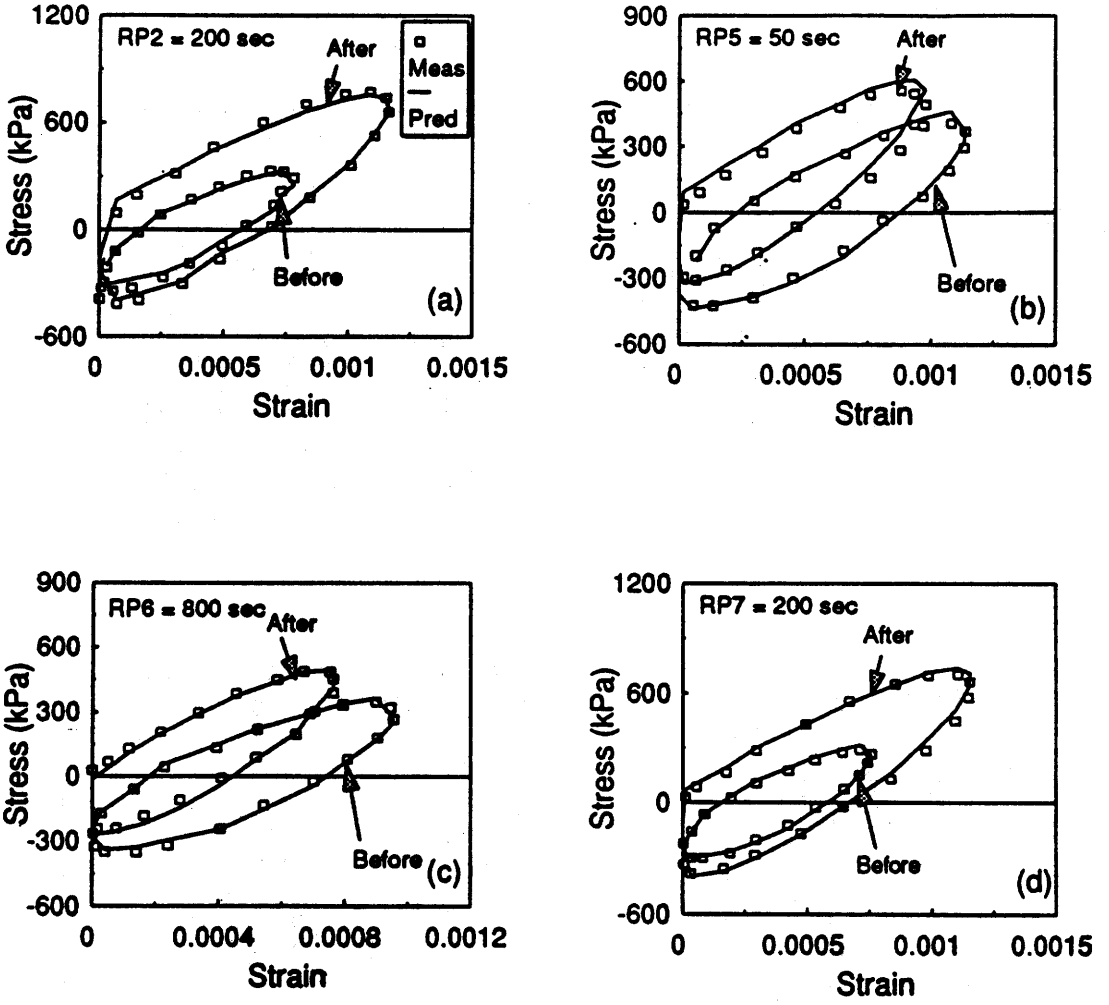

Figure 14. Prediction of Stresses Before and after Varying Rest Periods for Controlled-Strain Mode: (a) 200 S; (b) 50 S; (c) 800 S; (d) 200 S.

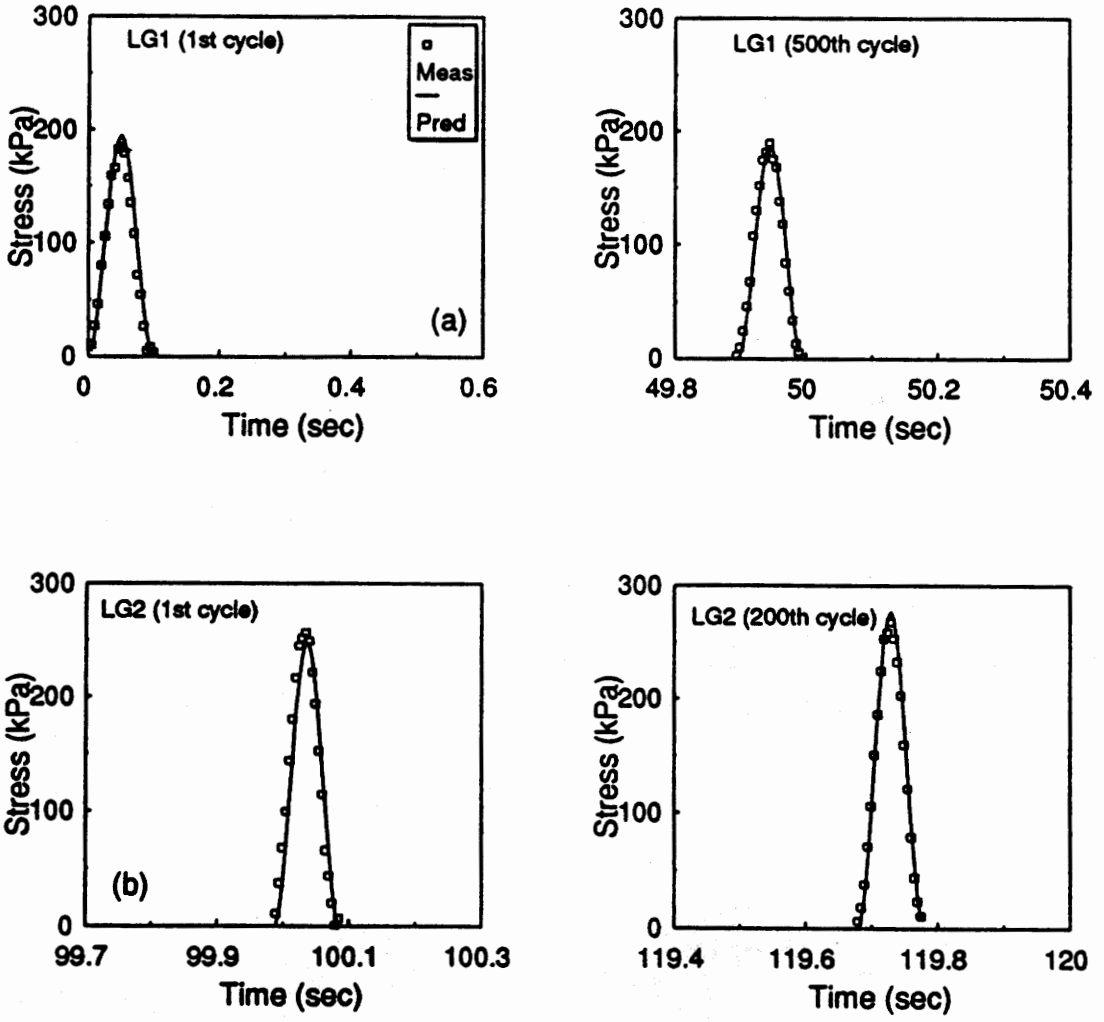

Figure 15. Prediction of Stresses for Different Loading Groups in the Controlled-Stress Validation History for AAM Mixture: (a) Loading Group 1; (b) Loading Group 2; (c) Loading Group 3; (d) Loading Group 5.

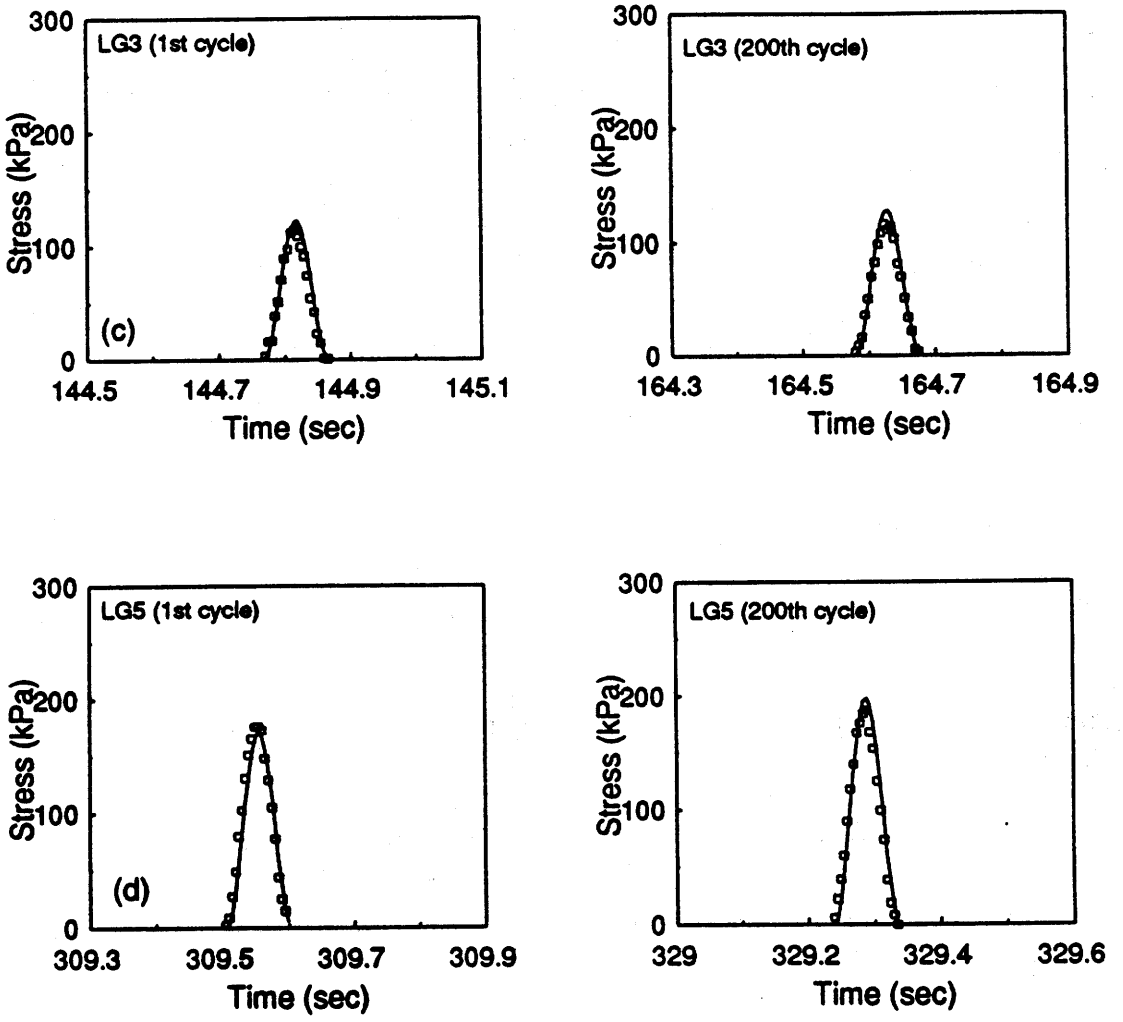

Figure 15. Continued

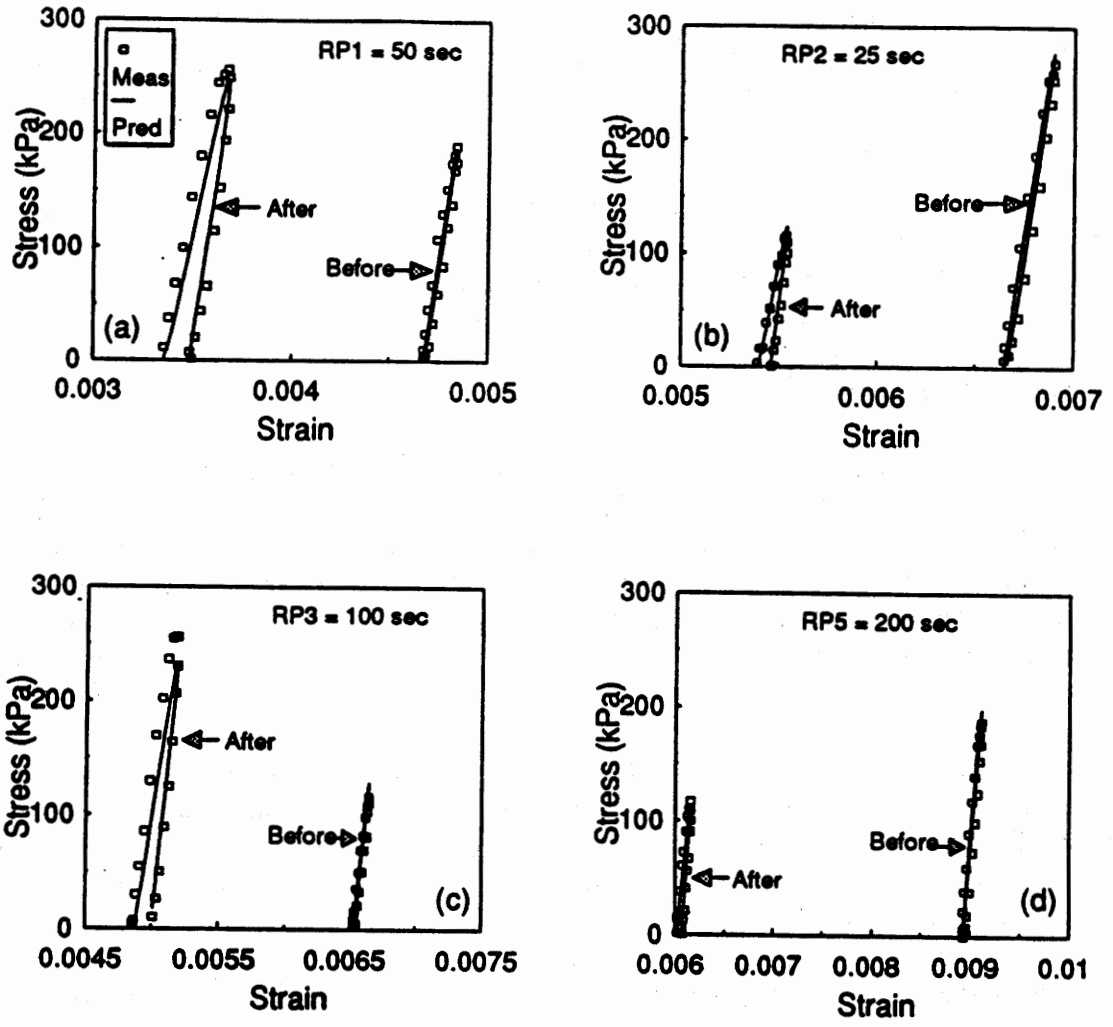

Figure 16. Prediction of Stresses Before and after Varying Rest Periods for Controlled-Stress Mode: (a) 50 s; (b) 25 s; (c) 100 s; (d) 200 s.

applied until the specimen failed. The strain amplitude in each loading group was held constant.

The measured and predicted stresses for loading groups 1, 2, 4, and 8 were plotted against loading time in Figure 13. The constitutive model successfully predicts the reduction in stress due to cyclic loading regardless of strain amplitudes applied during the tests. Figure 13(d) shows the accuracy of the prediction near the point of failure. These results verify that the constitutive model developed in this study is independent of strain amplitudes. Since the same loading time (0.1 second) was used throughout testing, different strain amplitudes produced different strain rates for each loading group. Thus, the verification results also demonstrate that the model can account for the coupling effects of rate-dependence and damage.

In Figure 14, the measured and predicted stresses before and after rest periods are plotted against strains. The predictions made by the constitutive equation (19) are satisfactory. The increases in stress after varying lengths of rest periods were predicted accurately, as were the effects of different sequences of varying load levels.

Controlled-Stress Cyclic Test

Three stress amplitudes (117, 190, and 265 kPa) and five rest periods between 25 and 400 seconds were randomly applied to create the stress history shown in Figure 12(b). Again, the cyclic loading continued in loading group 7 until failure. The pseudo strain values were calculated using the measured strain responses. The stresses were then predicted using the constitutive equation (17) and compared with the measured stresses in Figure 15. Figure 16 displays the validation results for the cycles before and after varying lengths of rest period.

In general, the accuracy of prediction in the controlled-stress cyclic test is acceptable, but a little poorer than the controlled-strain case. It must be noted here that the coefficients in the constitutive model used in the prediction were obtained solely from the controlled-strain cyclic tests. The extrapolation from the controlled-strain mode to the controlled-stress mode might have affected the accuracy. Another reason for the reduced accuracy is attributed to some errors associated with the calculation of pseudo strain in the controlled-stress case due to inaccurate representation of strain history. Unlike the controlled-strain case where the strain history is simple and known a priori, the strain in the controlled-stress mode is the response and needs to be measured during the entire testing period. It is impossible, or at least extremely impractical, to acquire all the stress-strain data up to failure in long-term fatigue tests because of the limitation in computer memory capacity. Therefore, the strain histories in the controlled-stress tests are generated from a limited number of data sets that were collected at different stages of fatigue testing. Strains that were not measured were interpolated using the measured

strain values, which introduce some errors in the pseudo-strain calculation, resulting in less accurate prediction of stresses in Figures 15 and 16.

Although the prediction within each cycle is not as good as the controlled-strain case, the constitutive model reasonably predicts the stresses up to failure, demonstrating the applicability of the constitutive model to different modes of loading. Due to the inherent difficulties of calculating pseudo-strain values in controlled-stress fatigue tests, controlled-strain cyclic tests are recommended for fatigue characterization of asphalt concrete.

CHAPTER 6: FATIGUE PERFORMANCE PREDICTION

When equation (19) is used for fatigue performance prediction (i.e., prediction of the number of cycles to failure, N_f), only the functions F and H are needed, which represent the changes in S^R during cyclic loading and rest periods, respectively. The function G is required to predict hysteretic stress-strain behavior during loading and unloading paths. It is an important component for accurate constitutive modeling, but is not needed in predicting N_f, because peak stress and strain values in each cycle are sufficient to model the change in S^R. Therefore, the fatigue performance prediction using equation (19) boils down to accurate modeling of the change in S^R as a function of loading cycles under complex loading histories.

When continuous loading is applied without rest, an S-shape curve (Figure 9) is observed between C_1 (normalized S^R) and S_1 with a quick drop in C_1 near the failure. The reduction in S^R by 50 percent from the initial S^R value (or C_1 value of 0.5) can be used as the failure criterion irrespective of mode of loading and stress/strain amplitude, which has also been validated by visual observation of specimens failure during fatigue tests.

These findings lead to the following fatigue performance prediction model:

$$\textit{Failure occurs when } C_1 + H \leq 0.5 \tag{23}$$

Since H is a function of $C_2(S_2)$ and $C_3(S_3)$, the left-hand term is represented by the three functions, $C_1(S_{1n})$, $C_2(S_2)$, and $C_3(S_3)$. The coefficients of these functions for the two mixtures are summarized in Table 4.

A validation study has been performed on the fatigue performance prediction model (23) using fatigue test data from AAD and AAM mixtures under controlled-strain mode. The controlled-stress fatigue test data were not used in the validation study because of the inherent difficulties of calculating pseudo-strain values in controlled-stress fatigue tests as discussed in the preceding section "Validation of the Constitutive Model." The results are shown in Figure 17. The data points in this figure represent a total of 16 tests with various combinations of strain amplitudes and rest durations.

Three specimens represented by the three points above the line of equality failed much earlier than expected and resulted in the percentage of error between the predicted and measured N_f's ranging from 70 to 120 percent. An additional test was conducted for each of the three points, and the replicates all fell below 10 percent error, indicating that the sample-to-sample variation affected the prediction accuracy in these three tests. In all other tests, the percentage of error was kept below 10 percent. Hence, less than 10 percent error in 13 out of 16 cases is deemed satisfactory.

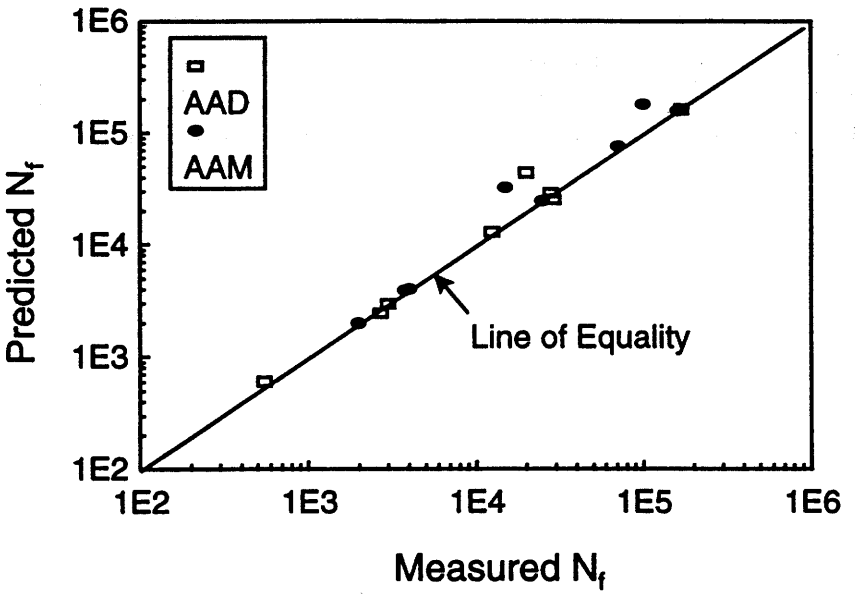

Figure 17. Validation of the Fatigue Prediction Model.

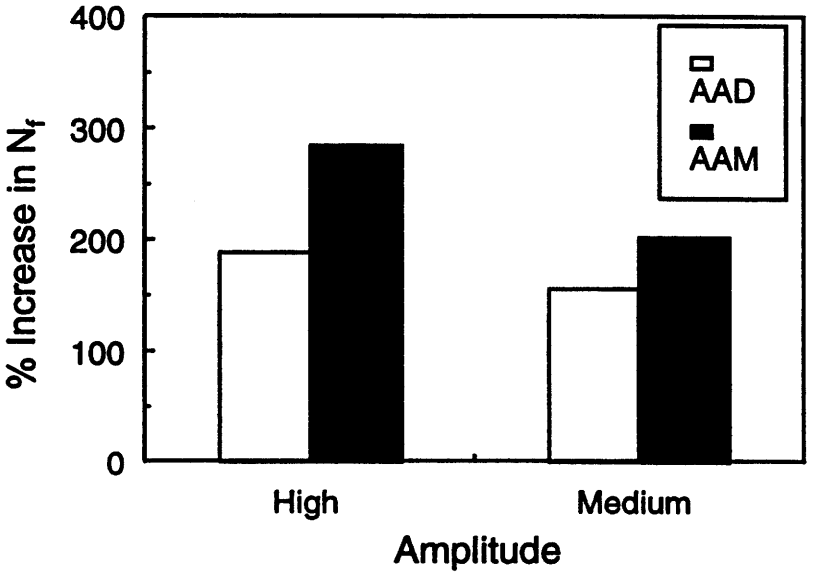

Figure 18. Percentage Increase in Fatigue Life of Two Mixtures Due to Rest Periods.

The numbers of cycles to failure with and without rest periods were measured from the fatigue tests and used for the calculation of percent increase in N_f due to the rest periods. Figure 18 presents the average percentage of increase in N_f of the two mixtures in controlled-stress mode. Regardless of stress amplitudes used in testing, AAM mixture benefits more from introducing rest periods. The greater strength regain from AAM mixture due to rest periods was also found from a series of third-point-load fatigue tests in Task 3 with and without rest periods on AAD and AAM beam specimens.

CHAPTER 7: A PROPOSED UNIAXIAL FATIGUE TESTING PROTOCOL

As shown in equation (23), the fatigue performance prediction (i.e., prediction of the number of cycles to failure, N_f) requires only the functions C_1 and H, which represent the changes in S^R during cyclic loading and rest periods, respectively. The function H is composed of two internal state functions, C_1 and C_2. Therefore, the fatigue performance prediction using equation (23) reduces down to the characterization of the functions C_1, C_2, and C_3. To characterize these functions, the following uniaxial tensile fatigue testing protocol has been developed as a standard, specification-type test method for fatigue damage and microdamage healing evaluation.

Test Specimens

The laboratory fabricated specimens shall be prepared in accordance with the procedures described in Appendix A. The specimens shall have a height of 203 ±1.6 mm (8 ±1/16 in). The diameter shall be 102 mm (4 in).

Test Procedure

The apparatus used for testing in the tensile mode shall be such that eccentricities in loading are minimized and the specimen is properly aligned with the loading ram. The testing system must be able to accurately measure load and deflection data through the duration of testing. Appropriate load cells and LVDTs shall be used to ensure adequate resolution in measurements for the entire test.

The asphalt concrete cores shall be placed in a controlled temperature chamber and brought to the specified test temperature. The samples must remain in the chamber for a minimum of 3 hours at the testing temperature prior to the start of the test. Testing shall be conducted while the specimen is located in the temperature-controlled chamber to maintain specimen temperature.

To determine the viscoelastic material properties E(t), $|E^*|$, and δ, a uniaxial tensile creep test shall be performed at 25°C (77°F). The loading time shall be 700 seconds. The load level shall be such that the material remains in the linear viscoelastic range (i.e., no significant damage). The appropriate load shall be determined by performing creep tests on a specimen at incremental load levels. Adequate time must be allowed between subsequent tests to allow complete relaxation in the specimen. The highest load at which the creep compliance curve overlaps the curve from the previous load level shall be used.

The electronic measuring and data acquisition systems shall be adjusted and the gains set as necessary. Prior to testing, a seating load equivalent to 5 percent of the testing load shall be applied for a minimum of 30 minutes to condition the test setup.

The data acquisition system shall be set up to record data at a minimum of 200 points per second for the first 15 seconds of loading. One point per second shall be collected for the remainder of the test.

The creep compliance shall be converted to E(t), $|E^*|$, and δ using the procedure described in the following section.

To characterize the material functions C_1, C_2, and C_3, uniaxial tensile fatigue tests in the controlled-strain mode shall be performed at 25°C (77°F). A haversine loading pattern with 0.1 second loading time shall be used. The sampling rate for data acquisition shall be 200 points per second.

Continuous cyclic loading tests at two strain amplitudes shall be conducted to characterize the C_1 material function. The strain amplitudes shall be chosen such that the target number of cycles to failure (N_f) are approximately 5,000 and 100,000 cycles.

To characterize material functions C_2 and C_3, cyclic loading tests with rest periods shall be performed at two strain amplitudes. The strain amplitudes shall be the same as those for the continuous cyclic loading. The length and sequence of rest periods shall be as follows: 20s, 1m, 3m, 10m, 30m, 30m, 10m, 3m, 1m, 20s. The number of load repetitions before each rest period shall be $N_{f,w/oRP} / 20$. After the last rest period, continuous cyclic loading to failure shall be applied.

The coefficients for functions C_1, C_2, and C_3 shall be determined following the procedure described below.

Characterization of Relaxation Modulus

1. From the creep compliance data, determine D_0, D_i, and τ_i in the following equation using the collocation method described at the end of this subsection:

$$D(t) = D_0 + \sum_{i=1}^{M} D_i(1 - e^{-\frac{t}{\tau_i}}) \qquad (24)$$

where $D(t)$ = uniaxial tensile creep compliance,
t = time,
D_0, D_i = regression coefficients,
τ_i = retardation times, and
M = number of decades in a logarithmic time scale (10 is recommended).

2. Calculate N and E_∞ using the following equations:

$$N = M \tag{25}$$

$$\frac{1}{E_\infty} = D_0 + \sum_{i=1}^{M} D_i \tag{26}$$

Determine the remaining coefficients, E_i's, based on the following steps:

2.1 Calculate values of 1/ using the following equation:

$$\tilde{D} = D_0 + \sum_{i=1}^{M} \frac{D_i}{s\tau_i + 1} \tag{27}$$

2.2 Assume approximate values of relaxation times ρ_i (i = 1,2,...,N). Values between 10^{-6} and 10^{4} are recommended.

2.3 Determine E_i's by minimizing square errors between the values of $1/\tilde{D}$ and mathematical expression of $\tilde{E}$ in the following equation:

$$\tilde{E} = E_\infty + \sum_{i=1}^{N} \frac{E_i s}{s + \frac{1}{\rho_i}} \tag{28}$$

3. The coefficients obtained from Step 2 are used to represent the relaxation modulus in the following equation:

$$E(t) = E_\infty + \sum_{i=1}^{N} E_i e^{-\frac{t}{\rho_i}} \tag{29}$$

Collocation Method: Rather than calculating the retardation time τ_i by collocation (which would lead to a nonlinear system of equations), one can specify values for the time constants prior to collocating the exponential series. In general, if the τ_i's are separated by no more than one decade, a smooth curve is obtained. The values of τ_i's will be selected to be exactly one decade apart, as described below.

First, collocation points are selected one decade apart:

$$t_i = 10^{(i-c)} \qquad \text{for } i = 1, 2, 3, \ldots, M \tag{30}$$

In the above equation, c and M are determined based on the time range of the measured creep data. For example, if the creep compliances are measured in the time range of 10^{-3} s to 10^{4} s, then c=4 and M=8. Further, select each τ_i according to

$$\tau_i = k10^{(i-c)} \qquad \text{for } i = 1, 2, 3, \ldots, M \tag{31}$$

where k is an arbitrary constant.

Equate the time dependent part of D(t) to that of the creep compliance, $D(t)-D_0$, at the M point of t_i:

$$D(t) - D_0 = \sum_{i=1}^{M} D_i(1 - e^{-\frac{t}{\tau_i}}) \tag{32}$$

which is a linear system of equations for the M unknowns, t_i. That is, an MxM matrix can be constructed as follows:

$$\begin{bmatrix} A_{11} & A_{12} & \cdot & \cdot & \cdot & A_{1M} \\ A_{21} & \cdot & \cdot & \cdot & \cdot & \cdot \\ \cdot & \cdot & \cdot & \cdot & \cdot & \cdot \\ \cdot & \cdot & \cdot & \cdot & \cdot & \cdot \\ A_{M1} & \cdot & \cdot & \cdot & \cdot & A_{MM} \end{bmatrix} \begin{Bmatrix} D_1 \\ D_2 \\ \cdot \\ \cdot \\ D_M \end{Bmatrix} = \begin{bmatrix} D(t_1) - D_0 \\ D(t_2) - D_0 \\ \cdot \\ \cdot \\ D(t_M) - D_0 \end{bmatrix} \tag{33}$$

where $A_{ij} = 1 - e^{-t_i/\tau_j}$. Once the inverse matrix $[A]^{-1}$ is determined, [D] can be easily obtained. If the fitting curve is not smooth enough, adjust the value of k in equation (31). Then determine D_i values again following the procedure described above.

Characterization of Dynamic Modulus and Phase Angle

1. Calculate the storage compliance (D') and the loss compliance (D") from equation (24) using the following equations:

$$D' = D_0 + \sum_{i=1}^{M} \frac{D_i}{\omega^2 \tau_i^2 + 1} \quad (34)$$

$$D'' = \sum_{i=1}^{M} \frac{\omega \tau_i D_i}{\omega^2 \tau_i^2 + 1} \quad (35)$$

where $\omega = 2\,\pi\,f = 2\,\pi\,(0.08/t)$.

2. Determine the dynamic compliance and the phase angle using the following equations:

$$|D^*| = [(D')^2 + (D'')^2]^{1/2} \quad (36)$$

$$\delta = tan^{-1}\left(\frac{D'}{D''}\right) \quad (37)$$

3. Determine the dynamic modulus, $|E^*|$, using the following equation:

$$|E^*| = \frac{1}{|D^*|} \quad (38)$$

Characterization of Internal State Functions

Function C_1 and Constant α_1:

1. Use the two test data sets obtained from cyclic loading tests without rest periods.

2. Calculate an initial value of α_1 using $\alpha_1 = (1+1/m)$ where m is the slope of the middle linear portion of the creep compliance versus time curve in a logarithmic scale.

3. Calculate the value of the damage parameter at the i^{th} cycle, $S_{1(i)}$, corresponding to current pseudo stiffness $C_{1(i)}$ using the following equation:

$$S_{1(i=N)} \cong \sum_{i=1}^{N} \left[\frac{I}{2}(\varepsilon_{mi}^{R})^2 (C_{1(i-1)} - C_{1(i)})\right]^{\frac{\alpha_1}{(1+\alpha_1)}} (t_1 - t_{i-1})^{\frac{1}{(1+\alpha_1)}} \quad (39)$$

where I = initial pseudo stiffness (pseudo stiffness at the 1st cycle may be used for the value of I),

$C_{1(i)}$ = pseudo stiffness at the i^{th} cycle ($=\sigma_{m(i)} / (/\varepsilon_{m(i)}^{R})$),

$\varepsilon_{m(i)}^{R}$ = peak pseudo strain in the i^{th} cycle, and

t_i = time corresponding to $C_{1(i)}$ at the i^{th} cycle.

4. Plot the values of C_1 against the S_1 values using two data sets.

5. Adjust the value of α_1 (resulting in the change in S_1 values) until all the data from two data sets fall on the same curve.

6. Perform a regression analysis between the C_1 and S_1 values resulting from Step 5 to determine the coefficients (C_{11}, C_{12}, and C_{13}) of the function $C_1(S_1)$ shown below:

$$C_1(S_1) = C_{10} - C_{11}(S_1)^{C_{12}} \quad (40)$$

Function C_2 and Constant α_2:

1. Use the two test data sets obtained from cyclic loading tests with rest periods.
2. Determine an initial value of α_2 using $\alpha_2 = (1+1/m)$ where m is the slope of the middle linear portion of the creep compliance versus time curve in a logarithmic scale.
3. Calculate the value of the healing parameter at the i^{th} cycle, $S_{2(i)}$, corresponding to the i^{th} rest period using the following equation:

$$S_{2(i)} \cong \left[\frac{I}{2}(\varepsilon_{m(i)}^{R})^2 (S_A^R - S_B^R)\right]^{\frac{\alpha_2}{(1+\alpha_2)}} t_{RP(i)}^{\frac{1}{(1+\alpha_2)}} \quad (41)$$

where I = initial pseudo stiffness (pseudo stiffness at the 1st cycle may be used for the value of I),

C_2 = $S_A^R - S_B^R$

S_A^R = pseudo stiffness right after the i^{th} rest period,

S_B^R = pseudo stiffness right before the i[th] rest period,

$\varepsilon_{m(i)}^R$ = peak pseudo strain right before the i[th] rest period, and

$t_{RP(i)}$ = duration of the i[th] rest period.

4. Plot the values of C2 ($=S_A^R - S_B^R$) against the S_2 values calculated from the two data sets.
5. Adjust the value of α_2 (resulting in the change in S_2 values) until all the data from two data sets fall on the same curve.
6. Perform a regression analysis between the C_2 and S_2 values resulting from Step 5 to determine the coefficients (C_{21}, C_{22}, and C_{23}) of the function $C_2(S_2)$ shown below:

$$C_2(S_2) = C_{20} - C_{21}(S_2)^{C_{22}} \tag{42}$$

Function C_3 and Constant α_3:

1. Use the two test data sets obtained from cyclic loading tests with rest periods.

2. Determine an initial value of α_3 using $\alpha_3 = (1+1/m)$ where m is the slope of the middle linear portion of the creep compliance versus time curve in a logarithmic scale.

3. Calculate the value of the damage parameter at the i[th] cycle, $S_{3(i)}$ corresponding to the value of $C_{3(i)}$ after a rest period using the following equation:

$$S_{3(i=N)} \cong \sum_{i=1}^{N} \left[\frac{IS_A^R}{2}(\varepsilon_{mi}^R)^2 (C_{3(i-1)} - C_{3(i)}\right]^{\frac{\alpha_3}{(1+\alpha_3)}} (t_i - t_{i-1})^{\frac{1}{(1+\alpha_3)}} \tag{43}$$

where I = initial pseudo stiffness (pseudo stiffness at the 1[st] cycle may be used for the value of I),

$C_{3(i)}$ = normalized pseudo stiffness at the i[th] cycle after the rest period ($=S^R/S_A^R$),

S_A^R = pseudo stiffness right after the rest period,

$\varepsilon_{m(i)}^R$ = peak pseudo strain at the i[th] cycle after the rest period, and

t_i = elapsed time after the rest period that corresponds to $\varepsilon_{m(i)}^R$.

4. Calculate the values of C_3 ($=S^R/S_A^R$) and S_3 after each rest period.

5. Plot the values of C_3 against the S_3 values calculated from the two data sets.

6. Adjust the value of α_3 (resulting in the change in S_3 values) until all the data from two data sets fall on the same curve.

7. Perform a regression analysis between the C_3 and S_3 values resulting from Step 6 to determine the coefficients (C_{31}, C_{32}, and C_{33}) of the function $C_3(S_3)$ shown below:

$$C_3(S_3) = C_{30} - C_{31}(S_3)^{C_{32}} \tag{44}$$

Validation of the Proposed Test Protocol

In order to validate the fatigue test procedure described above, uniaxial tensile cyclic loading tests with and without rest periods were performed on the AAD mixture. Two strain amplitudes, 0.0009 and 0.0012 units, were used in the validation tests. The function C_1 was successfully characterized using the data obtained from the cyclic loading tests without rest periods under two different strain amplitudes. The functions C_2 and C_3 were characterized using the data obtained from cyclic loading tests with rest periods. The coefficients for the functions C_1, C_2, and C_3 are presented in Table 5.

Table 5. Model Coefficients Obtained from the Proposed Fatigue Testing Protocol.

Mix	C_{10}	C_{11}	C_{12}	C_{20}	C_{21}	C_{22}	C_{30}	C_{31}	C_{32}
AAD	1.0	0.5	0.41	-0.182	0.036	0.25	1.0	0.0018	0.54

CHAPTER 8: CONCLUSIONS

Damage accumulation under uniaxial tensile cyclic loading and microdamage healing during rest periods was modeled using the elastic-viscoelastic correspondence principle and work potential theory. The pseudo-strain transformation greatly simplified the task of evaluating damage growth and microdamage healing of asphalt concrete while separating out viscoelastic behavior. The resulting constitutive model successfully predicts the damage growth of asphalt concrete under monotonic loading of varying strain rates and damage growth as well as recovery due to complex cyclic loading histories, in both controlled-strain and controlled-stress modes, composed of randomly applied multi-level loading with different loading rates and varying durations of rest.

Fatigue lives of AAD and AAM mixtures are predicted using the constitutive model for constant stress/strain amplitude cyclic loading histories with and without rest periods. In 13 out of 16 different loading histories with various combinations of strain amplitudes and rest durations, the error between the predicted and the measured numbers of cycles to failure was less than 10 percent. Comparison of fatigue lives with and without rest periods indicates that the beneficial effects of rest periods on fatigue performance are more pronounced in AAM mixtures than in AAD mixtures.

Based on the constitutive model developed in this task, a fatigue test protocol that is suitable for standard, specification-type testing is developed. This test protocol employs a set of uniaxial tensile tests for viscoelastic characterization as well as the characterization of internal state functions representing the fatigue damage growth and microdamage healing in asphalt-aggregate mixtures. A stepwise analysis procedure based on viscoelasticity and work potential theory is also developed for determination of model coefficients.

APPENDIX A

SPECIMEN PREPARATION PROTOCOL FOR ROLLING WHEEL COMPACTION

APPENDIX A

SPECIMEN PREPARATION PROTOCOL FOR ROLLING WHEEL COMPACTION

This appendix describes the details on how to prepare hot mix asphalt concrete and compact a slab using the rolling wheel compactor. The protocol is designed to minimize both sample-to-sample variation and the density variation within each sample. Compaction and coring directions for cylindrical and beam specimens are shown in Figure A.1.

1. GENERAL PROCEDURE

(i) Heating of Materials for Mixing

Mixing Temperatures

AAD : 140°C (285°F)
AAM : 140°C (285°F)

Premixing Heating Time

Asphalt : 2 hrs (stirring) at mixing temperature
Aggregate : Overnight (covered) for mixing in the morning
Equipment : 2 hrs at mixing temperature

(ii) Mixing

Mixing 4 minutes with the continuous, uniform application of heat under the mixing bowl

(iii) Preparation for Compaction

Heating the mixture for 2 hrs at 240°F (116°C)

(iv) Compaction with the Rolling Wheel Compactor

(v) Removing Mold

24 hrs after the compaction

(vi) Coring

After 2 days in 25°C (77°F)

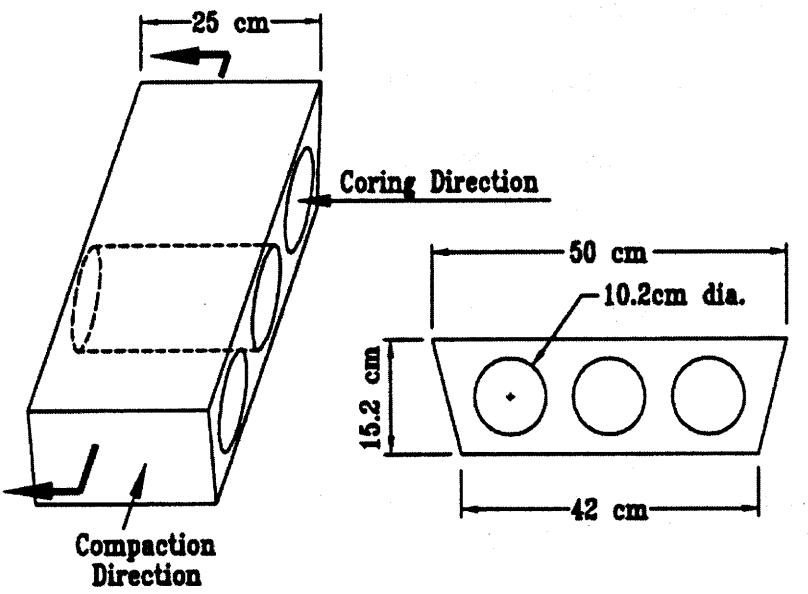

Figure A.1. Schematic Diagram of Compaction and Coring for Cylindrical and Beam Specimens.

2. PREPARATION OF MATERIALS FOR MIXING

Aggregate

A. Place a bowl on a balance and make the balance zero.

B. According to the attached Form-1, put certain amount of aggregate into the bowl for each sieve size.

C. Cover the bowl with aluminum foil.

D. Make a note on the foil.

E. Repeat the steps A to D for a total number of batches.

F. Check and adjust the oven temperature (not by the set temperature in front of the oven, but by the temperature of sands in the oven) to the mixing temperature (140°C (285°F)).

G. Dry the aggregates contained in the bowls overnight in the oven.

Asphalt

A. Heat the asphalt contained in a 5-gallon container (47 lbs) for distribution to small cans (called the first heating).

-Temperature : 266°F (130°C)
-Period : 3□ hours

B. Distribute the heated asphalt into the small cans as soon as possible. The asphalt cannot be reheated for distribution.

C. Attach ID labels on the small cans.

D. In the morning, put the small cans containing asphalt into the oven.

Note: The maximum period for each asphalt in the oven should not exceed 3 hours.
Recommendation: Four (4) cans at a time with one hour interval.

E. Heat all the mixing tools in the oven (at mixing temperature) at least for an hour.

3. MIXING

A. Start the mixing after the asphalt temperature has reached the mixing temperature (normally 11/2 to 2 hours).

B. Prepare torch for the mixing.

C. Place a mixing bowl on the balance and zero the balance.

D. Pour one batch of heated aggregate into the mixing bowl and check the aggregate weight for verification.

E. Quickly mix the aggregate and make an interior pocket on the aggregate for asphalt.

F. Zero the balance.

G. Add asphalt to the aggregate.

H. Install mixer and mixing bowl.

I. Mix the asphalt and aggregate for 4 minutes with uniform and constant application of torch.

J. Pour and scrape the mixture from the mixing bowl into a pan.

K. Cover the pan with aluminum foil and write an identification.

L. Reheat the mixing equipment.

M. Repeat the steps C to L for the rest of batches.

4. CALCULATION OF TOTAL NUMBER OF BATCHES FOR A SLAB

Watsonville Granite Aggregate + AAD Asphalt

A. Wt. of dry aggregate per batch: 5,000 g

B. Percent of asphalt by wt. of dry aggregate : 5.263 %

C. Wt. of asphalt (A*B/100): 263.16 g

D. Wt. of mixture per batch (A+C): 5263.16 g

E. Rice maximum specific gravity of the mixture: 2.565

F. Volume of slab:

Top (V_T): 9,491 cm^3
Bottom (V_B): 8,624 cm^3

G. Target air voids:

Top (a_T): 4.0 %
Bottom (a_B): 4.04 % (adjusted for the effect of top layer)

H. Wt. of the mixture needed for a slab:

Top (W_T):
$W_T = V_T(1-a_T)*E = 23,371$ g
Bottom (W_B):
$W_B = V_B(1-a_B)*E = 21,227$ g
Total (W):$W = W_T + W_B = 44,598$ g

I. Total number of batches:

H / D = 9

FORM-1 Weights of Materials to Assemble a Batch

Sieve Size	% Passing	% Retained	Cumulative Wt. per Batch (2,500 g)	Cumulative Wt. per Batch (5,000 g)
1"	100	0	0	0
3/4"	95	5	125	250
1/2"	79	16	525	1050
3/8"	67	12	825	1650
#4	47	20	1325	2650
#8	33	14	1675	3350
#16	22	11	1950	3900
#30	14	8	2150	4300
#50	9	5	2275	4550
#100	5	4	2375	4750
#200	-	5	2500	5000

APPENDIX B

CONSTITUTIVE MODELING OF ASPHALT CONCRETE USING VISCOELASTICITY AND CONTINUUM DAMAGE MECHANICS

APPENDIX B

CONSTITUTIVE MODELING OF ASPHALT CONCRETE USING VISCOELASTICITY AND CONTINUUM DAMAGE MECHANICS

This appendix describes the details of the constitutive modeling work conducted under Task 2. The major subjects included herein are:

1. Theory of Viscoelasticity and Damage Mechanics
2. Testing Programs
3. Determination of Viscoelastic Material Properties
4. Experimental Study of Correspondence Principle
5. Constitutive Modeling of Asphalt Concrete with Growing Damage
6. Constitutive Modeling of Asphalt Concrete with Growing Damage and Micro Damage Healing
7. Conclusions and Recommendations

Theory of Viscoelasticity and Damage Mechanics

In modeling the hysteretic behavior of asphalt-aggregate mixtures under multi-level repetitive loading with random durations of rest, the following constitutive factors are deemed important:

1. viscoelasticity of the matrix that causes hysteretic behavior under cyclic loading and relaxation during rest periods,
2. fatigue damage growth during cyclic loading,
3. healing during rest periods, and
4. temperature dependence of asphalt matrix.

Effects of temperature on the constitutive behavior can be included in viscoelastic material properties, such as creep compliance and relaxation modulus, using the time-temperature superposition principle. In this study, temperature effects are not considered because only one temperature is used in fatigue testing. The major difficulty in evaluating the effects of the remaining three factors arises from the fact that these mechanisms occur simultaneously under cyclic loading with rest periods. For instance, during loading and unloading paths, the inelastic response of the material can be due to damage incurred in the material and/or the viscoelastic nature of the material. Relaxation and healing also occur at the same time during rest periods. Therefore, it is very important to separate the viscoelasticity from damage and healing in order to accurately predict the inelastic response of the material.

The modeling approach taken in this study categorizes these constitutive factors into the following three components: (1) linear viscoelasticity, (2) fatigue damage, and (3) microdamage

healing. Microdamage healing includes all the mechanisms, except linear viscoelastic relaxation, contributing to the recovery of stiffness or strength during rest periods, such as fracture healing, steric hardening, nonlinear viscoelastic relaxation, etc. The correspondence principle using the pseudo-strain concept is used to eliminate the time-dependence of the material from the hysteretic stress-strain behavior. Work potential theory (Schapery, 1990), a continuum damage theory based on irreversible thermodynamics principles, is employed to model the damage and microdamage healing. Damage parameter (Schapery, 1981), based on the generalization of the crack growth law, is also used in the modeling of the damage growth as an alternative approach to work potential theory.

Theory of Viscoelasticity

Viscoelastic Constitutive Equations

Viscoelastic materials, including asphalt concrete, have a time- or rate-dependence. The response of such materials depends not only on current state of input, but also on all past history of input and, in a general sense, the materials have a memory for all past history of input. For these viscoelastic materials, theory of viscoelasticity has been successfully used to describe the history-dependent behavior. The response of a linear viscoelastic body to any loading histories can be expressed in terms of a convolution integral (i.e., the viscoelastic body is considered to be simply a *linear black box*). If the system is linear, the following two conditions should be satisfied:

a. Homogeneity: $R\{AI\} = A\,R\{I\}$ (B.1)

b. Superposition: $R\{I_1 + I_2\} = R\{I_1\} + R\{I_2\}$ (B.2)

where I_1, I_2 = input histories,
R = response, and
A = arbitrary constant.

The symbol { } represents that the response is a function of input history.

For non-aging linear viscoelastic materials, the stress-strain relationship is

$$\sigma_{ij} = \int_0^t C_{ijkl}(t-\tau)\frac{d\varepsilon_{kl}}{d\tau}\,d\tau \qquad \text{(B.3)}$$

where C_{ijkl} are relaxation functions that are mechanical properties of the material. This equation is often called a *convolution integral* or *hereditary integral*. In the original convolution integral, the lower limit in the integration is $-\infty$, but can be reduced to 0 if the motion starts at time $t=0$ and $\sigma_{ij}=\varepsilon_{kl}=0$ for $t < 0$. In order to allow for the possibility of a discontinuous change in ε_{kl} at time $t=0$, the lower limit in (B.3) and succeeding convolution integrals should be interpreted as 0^-

unless indicated otherwise. If current strain is determined by the current value and past history of stress, an alternative form of the viscoelastic stress-strain relation is as follows:

$$\varepsilon_{ij} = \int_0^t S_{ijkl}(t-\tau)\frac{d\sigma_{kl}}{d\tau}\,d\tau \qquad \text{(B.4)}$$

where S_{ijkl} are creep functions that represent mechanical properties of the material.

Elastic-Viscoelastic Correspondence Principle

Theory of viscoelasticity allows viscoelastic problems to be transformed so that they are mathematically equivalent to elastic problems with the substitution of elastic moduli. This correspondence can be made by taking an appropriate transformation of the governing field and boundary equations of viscoelastic problems with respect to time. In general, the principle employs the Laplace transformation for linear viscoelastic materials.

As shown in Table B.1, all the field equations and boundary conditions for non-aging linear viscoelastic media are identical to those of the linear elastic case except that the constitutive equation of the linear viscoelastic media is in a convolution form. However, if one takes the Laplace transform of both constitutive equations, they can be reduced as follows:

a. Linear Elastic:

$$\bar{\sigma}_{ij} = C_{ijkl}\bar{\varepsilon}_{kl} \qquad \text{(B.5)}$$

b. Linear Viscoelastic:

$$\bar{\sigma}_{ij} = \tilde{C}_{ijkl}\bar{\varepsilon}_{kl} \qquad \text{(B.6)}$$

where $\bar{f}$ ≡ Laplace transform of f, and
$\tilde{f} = s\,\bar{f}$ ≡ Carson transform of f.

Therefore, the linear viscoelastic constitutive equation (B.6) is identical to the linear elastic constitutive equation (B.5) except the Carson-transformed elastic moduli are in place of the elastic moduli. It is noted here that, when elastic moduli are constant, the Carson-transformed elastic moduli are elastic moduli themselves.

Schapery (1984) proposed the extended elastic-viscoelastic correspondence principle which can be applicable to both linear and nonlinear viscoelastic materials. He suggested that constitutive equations for certain viscoelastic media are identical to those for the elastic cases, but

stresses and strains are not necessarily physical quantities in the viscoelastic body. Instead, they are *pseudo variables* in the form of convolution integrals such that:

$$u_{ij}^{R} = \frac{1}{E_R}\int_0^t E(t-\tau)\frac{\partial u_{ij}}{\partial \tau}\,d\tau \qquad \text{(B.7)}$$

$$\sigma_{ij}^{R} = E_R\int_0^t D(t-\tau)\frac{\partial \sigma_{ij}}{\partial \tau}\,d\tau \qquad \text{(B.8)}$$

where σ_{ij}, u_{ij} = physical stresses and physical displacements,
σ_{ij}^{R}, u_{ij}^{R} = pseudo stresses and pseudo displacements,
E_R = reference modulus, which is an arbitrary constant, and
E(t), D(t) = relaxation modulus and creep compliance, respectively.

Using the concept of pseudo variables, Schapery (1984) introduced the three different correspondence principles for time-dependent, quasi-static solutions to nonlinear elastic and viscoelastic boundary value problems. In this study, his second correspondence principle was employed.

Table B.1 Governing Equations for Linear Elastic and Linear Viscoelastic Materials

Field Equations	**Linear Elastic**	**Linear Viscoelastic**
Equilibrium equations	$\sigma_{ij,j} + F_i = 0$	$\sigma_{ij,j} + F_i = 0$
Stress-displacements equations	$\varepsilon_{ij} = \frac{1}{2}(u_{i,j} + u_{j,i})$	$\varepsilon_{ij} = \frac{1}{2}(u_{i,j} + u_{j,i})$
Constitutive equations	$\sigma_{ij} = C_{ijkl}\,\varepsilon_{kl}$	$\sigma_{ij} = \int_0^t C_{ijkl}(t-\tau)\frac{d\varepsilon_{kl}}{d\tau}\,d\tau$
Boundary Conditions		
	$\sigma_{ij}\,n_j = T_i$ on S_T	$\sigma_{ij}\,n_j = T_i$ on S_T
	$u_i = U_i$ on S_u	$u_i = U_i$ on S_u

Correspondence Principle II:

If the surface of a traction boundary increases with time ($dS_T / dt \geq 0$), the solution for a viscoelastic case is

$$\sigma_{ij} = \sigma_{ij}^R \tag{B.9}$$

$$u_i = E_R \int_0^t D(t-\tau) \frac{\partial u_i^R}{\partial \tau} d\tau \tag{B.10}$$

where σ_{ij}^R and u_i^R satisfy equations of the reference elastic problem. Correspondence principle II states that the viscoelastic problem can be reduced to an elastic case by using physical stresses and pseudo strains. This correspondence principle is useful when applied to the case of a growing traction boundary surface, such as crack growth problem.

For linear viscoelastic materials, a uniaxial stress-strain relationship is:

$$\sigma = \int_0^t E(t-\tau) \frac{d\varepsilon}{d\tau} d\tau \tag{B.11}$$

Using the definition of pseudo strain in (B.7), (B.11) can be rewritten as:

$$\sigma = E_R \varepsilon^R \tag{B.12}$$

where

$$\varepsilon^R = \frac{1}{E_R} \int_0^t E(t-\tau) \frac{\partial \varepsilon}{\partial \tau} d\tau \tag{B.13}$$

A correspondence can be found between (B.12) and a linear elastic stress-strain relationship.

For nonlinear viscoelastic materials or viscoelastic materials with damage, the explicit form of the constitutive equation between stresses and pseudo strains is dependent on material type and loading geometry. Therefore, experimental studies are essential to establish the analytical representation of the constitutive model for a material of interest.

Damage Mechanics

In studying the constitutive behavior of a material with damage, two general approaches are usually considered: a micromechanical approach and a continuum approach. In the micromechanical approach, defects that constitute the damage are described by microscopic

geometrical parameters, such as microcrack size, orientation, and density. These parameters are evaluated through an appropriate microstructural evolution law, such as microcrack growth law. Mechanics is then typically applied on an idealized representative volume element to determine the effects of distributions of micro-defects on the macroscopic constitutive parameters, such as the effective stiffness of the damaged body. Such analyses are, in general, difficult to perform because of the intrinsic complexity of the microstructure and the micromechanisms and also due to the interactions among defects. Therefore, without proper simplifications and assumptions both in modeling and analysis, the micromechanical approach may fail to provide realistic information on the macroscopic constitutive framework for modeling the progressive degradation of mechanical properties of solids (Park, 1994). The micromechanical approach has been used particularly in studying behavior of various composites including concrete (Wu, 1985; Krajcinovic and Fanella, 1986; Sumarac and Krajcinovic, 1987; Ju, 1991).

In the continuum approach, or in so-called continuum damage mechanics, the damaged body is represented as a homogeneous continuum on a scale that is much larger than the flaw sizes. The state of damage is quantified by internal state variables (ISV's) within the context of thermodynamics of irreversible processes. The growth of damage is governed by an appropriate damage evolution law. The choice and interpretation of the internal state variables are somewhat arbitrary, and the functional form of the thermodynamic potential (typically Helmholtz or Gibbs free energy) and the resulting stress-strain relations are usually postulated on a phenomenological basis. The stiffness of the material, which varies with the extent of damage, is determined as a function of the internal state variables by fitting the theoretical model to available experimental data. The phenomenological continuum damage models provide a viable constitutive framework for efficient modeling of macroscopic mechanical behavior of materials with distributed damage without requiring explicit descriptions of microstructural evolution kinetics (Park, 1994). Initiated by Kachanov (1958), continuum damage mechanics has been extensively explored and applied to various engineering materials by many researchers. General reviews on continuum mechanics are given by several authors (Lemaitre, 1984; Kachanov, 1986; Krajcinovic 1984, 1989).

Most damage models that have generality are based on general principles of thermodynamics, because the inelastic mechanical behavior of engineering materials is intrinsically linked to irreversible thermodynamic processes accompanying energy dissipation and physical changes of the microstructure. In general, a continuum damage model consists of three major components: (1) selection of damage variables, (2) definition of strain energy density (as a function of damage variables and other state variables), and (3) a damage evolution law. In the following, work potential theory based on thermodynamics of irreversible processes is discussed.

Work Potential Theory

1. Elastic Behavior With Changing Microstructure

Schapery (1990) applied the method of thermodynamics of irreversible processes to develop a theory applicable to describing the mechanical behavior of elastic media with growing damage and other structural changes. The theory is general enough to allow for strong nonlinearitites and coupling between the internal state variables and to describe a variety of mechanisms, including micro- and macro-crack growth in composite materials. In the following, the elements of Schapery's theory are briefly reviewed.

The behavior of elastic media with changing structure will be expressed in terms of relationships between generalized forces Q_j and independent generalized displacements q_j (j=1,2,...,J). As is customary, these variables are to be selected for any given application such that

$$Q_j \delta q_j = \delta W' \tag{B.14}$$

for each virtual displacement δq_j, where $\delta W'$ is virtual work.

A basic assumption of material or structural response used in the work potential theory is that a so-called strain energy function $W=W(q_j, S_m)$ exists with the property that

$$Q_j = \frac{\partial W}{\partial q_j} \tag{B.15}$$

where q_j (j=1,2,...,J) = generalized displacements,
Q_j (j=1,2,...,J) = generalized forces, and
S_m (m=1,2,...,M) = internal state variables (or damage parameters).

S_m are the only independent thermodynamic state variables, besides q_j, needed to account for changes in the strain energy. We also assume $\partial W/\partial q_j$ is continuously differentiable in q_j and S_m. The term internal state variable (ISV) and damage parameter, will be used interchangeably throughout this report to refer to S_m, even though the changes in the structure are not necessarily deleterious to the material's behavior. The strain energy may vary significantly with the environmentally related parameters, such as temperature and moisture. For simplicity, these effects will not be included in illustrating the structure of the theory.

The total work done on the body by Q_j during an actual process, starting at some reference state, is denoted by W_T,

$$W_T \equiv \int Q_j dq_j \tag{B.16}$$

where the summation convention for repeated indices is used. The relationship between total work and strain energy may be derived by first noting that

$$dW = \frac{\partial W}{\partial q_j} dq_j + \frac{\partial W}{\partial S_m} dS_m = Q_j dq_j - f_m dS_m \tag{B.17}$$

where f_m is the *thermodynamic force* defined as follows:

$$f_m \equiv - \frac{\partial W}{\partial S_m} \tag{B.18}$$

Integrating equation (B.17) from an arbitrary state 1 at time t_1 to current state 2 at time t_2, and then solving for the work done during the time interval t_2-t_1 yield

$$\Delta W_T = W^{(2)} - W^{(1)} + \int_1^2 f_m dS_m \tag{B.19}$$

If we assume that a state function $W_S=W_S(S_m)$ exists such that

$$f_m = \frac{\partial W_S}{\partial S_m} \quad when \quad \dot{S}_m \neq 0 \tag{B.20}$$

where f_m is the *thermodynamic force*. Then, from (B.19) and (B.20),

$$\Delta W_T = W^{(2)} - W^{(1)} + W_S^{(2)} - W_S^{(1)} \tag{B.21}$$

For notational simplicity, it is helpful to introduce a reference state, which is an undeformed and undamaged state (i.e., $W^{(1)}=W_S^{(1)}=0$), and take W_T as the total work from t=0 up to current time. Thus,

$$W_T = W + W_S \tag{B.22}$$

Equation (B.22) states that the total work is the sum of the strain energy and the dissipated energy, which contributes to changes in the structure. It should be noted that equation (B.20) is similar to a crack growth law, and, in fact, it represents the evolution law for finding $S_m=S_m(q_j)$. The left-hand side of equation (B.20) is the available force for producing changes in

S_m, while the right side is the required force.

From equation (B.22) we deduce that W_T is a point function of q_j for those processes in which a set of S_m changes,

$$W_T = W(q_j, S_m) + W_S(S_m) = W(q_j, S_m(q_j)) + W_S(S_m(q_j)) \tag{B.23}$$

i.e.,

$$W_T = W_T(q_j) \tag{B.24}$$

Thus, from the definition of total work in equation (B.16),

$$Q_j = \frac{\partial W_T}{\partial q_j} \tag{B.25}$$

That is, the work W_T is not only a state function of q_j and S_m but is a potential function of q_j alone, thereby justifying the term *work potential*. Namely, the body exhibits hyperelasticity for each set of histories $q_j(t)$ that produces structural changes defined by the same set of parameters. Either equation (B.15) or (B.25) with (B.20) may be used in characterizing the mechanical behavior of an elastic body undergoing structural changes.

From equation (B.20) and the second law of thermodynamics, Schapery (1990) showed that the dissipated energy W_S never decreases in any physical process. In some cases, the fracture work may be zero, such as in crack healing and contact problems with or without surface energy (W_{sc}). For this case f_m=0 and the surface energy is included in the strain energy (Schapery, 1990).

2. Viscoelastic Behavior With Changing Microstructure

The elastic work potential theory reviewed in the previous section can be easily extended to viscoelastic behavior with structural changes using the extended correspondence principle (Schapery, 1984). According to the correspondence principle, the constitutive equation developed in the work potential theory for elastic media can be applied to viscoelastic media if the displacements q_j in equation (B.15) are replaced with pseudo displacements q_j^R as follows:

$$Q_j = \frac{\partial W^R}{\partial q_j^R} \tag{B.26}$$

where

$$q_j^R \equiv \frac{1}{E_R}\int_0^t E(t-\tau)\frac{\partial q_j}{\partial \tau}\,d\tau \tag{B.27}$$

The function W^R in equation (B.26) is like the strain energy function for elastic materials, but here it is a function of pseudo displacements. We shall call it pseudo strain energy function. All the hereditary effects of the viscoelastic body are taken care of by the pseudo displacements. As a result, the constitutive equation for viscoelastic body equation (B.26) is the same as the elastic constitutive equation (B.15) except q_j^R is in place of q_j.

As mentioned earlier, the rate-independent evolution law (B.20) is used for elastic materials. However, this evolution law cannot directly be transformed to an evolution law for viscoelastic materials through the correspondence principle. It is to be understood that not only the available force for the growth of S_m is rate-dependent through pseudo strains, but also the resistance against the growth of S_m is rate-dependent for most viscoelastic materials (Park et al., 1996). Therefore, a more generalized evolution law, which can account for the rate-dependent behavior of the materials, is needed. Based on the fact that the local crack growth rate obeys a power law in local J-integral, Schapery (1990) proposed the following form of the internal state evolution law:

$$\frac{dS_m}{dt} = A_m (f_m)^{\alpha_m} \tag{B.28}$$

where dS_m/dt is the damage evolution rate, $A_m=A_m(S_m)$, $f_m= - \partial W^R/\partial S_m$ is a thermodynamic force, and α_m is a regression constant related to material properties. The repeated index m is not to be summed hereinafter in this section unless otherwise specified.

The damage evolution law (B.28) can be reduced to the following simpler form without the function $A_m(S_m)$ through a change-of-variable technique (Park, 1994),

$$\frac{d\bar{S}_m}{dt} = \left(- \frac{\partial W^R}{\partial \bar{S}_m} \right)^{\alpha_m} \tag{B.29}$$

where

$$\bar{S}_m = \int [A_m(S_m)]^{-\frac{1}{1+\alpha_m}}\,dS_m \tag{B.30}$$

Finally, Schapery showed that the essential features of the elastic work potential model can be retained with the rate-type damage evolution law (B.29) when $\alpha_m >> 1$. Assuming that $\bar{S}_m = 0$ at t=0, integration of equation (B.29) yields,

$$\bar{S}_m = \int_0^t \left(-\frac{\partial W^R}{\partial \bar{S}_m}\right)^{\alpha_m} dt \tag{B.31}$$

Then, the α_m-th root of equation (B.31) is

$$\bar{S}_m^{\frac{1}{\alpha_m}} = \left[\int_0^t \left(-\frac{\partial W^R}{\partial \bar{S}_m}\right)^{\alpha_m} dt\right]^{\frac{1}{\alpha_m}} \tag{B.32}$$

The right-hand side of equation (B.32) is the so-called Lebesgue norm of the thermodynamic force. Approximating that $\alpha_m >> 1$ and the thermodynamic force has a power law relationship with time, equation (B.32) reduces to

$$-\frac{\partial W^R}{\partial \bar{S}_m} = \bar{S}_m^{\frac{1}{\alpha_m}} t^{-\frac{1}{\alpha_m}} \tag{B.33}$$

Testing Programs

All tests were conducted in a uniaxial tension mode using a servo-hydraulic closed-loop testing machine (Figure B.1). An environmental chamber was used to control the temperature of the specimens. A gluing jig (Figure B.2) and a uniaxial testing apparatus (Figure B.3) were developed to provide precise alignment of a cylindrical specimen with respect to the loading axis and to reduce eccentric stress concentration during tests. Also the locking mechanism employed in this device allows testing in both tension and compression. Each specimen was glued to the end plates, which were then connected to the loading frame through a load cell.

Test data were collected by a data-acquisition system with a multichannel 16-bit board. Displacements were measured in two different ways: one using two extensometers in the middle portion of the sample with a gauge length of 10.16 cm (4 in), and the other measuring between the top and bottom loading plates, which results in a 20.32-cm (8 in) gauge length. When fracture due to fatigue does not occur in the middle portion of the specimen, the displacement measured by the extensometers is not able to represent the overall behavior of the specimen.

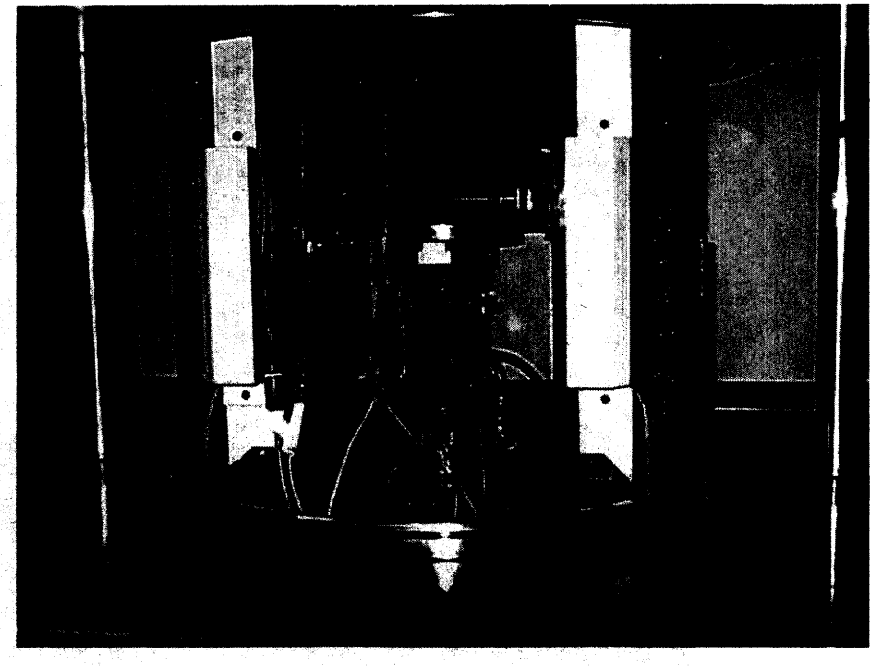

Figure B.1. Servo-hydraulic Closed Loop Testing Machine.

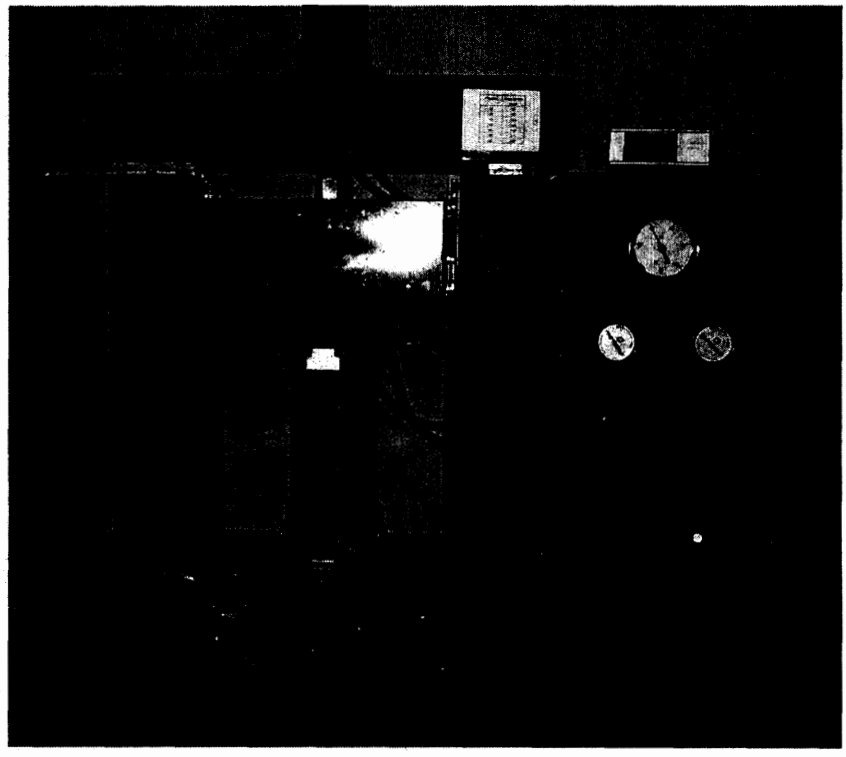

Figure B.2. Gluing Jig.

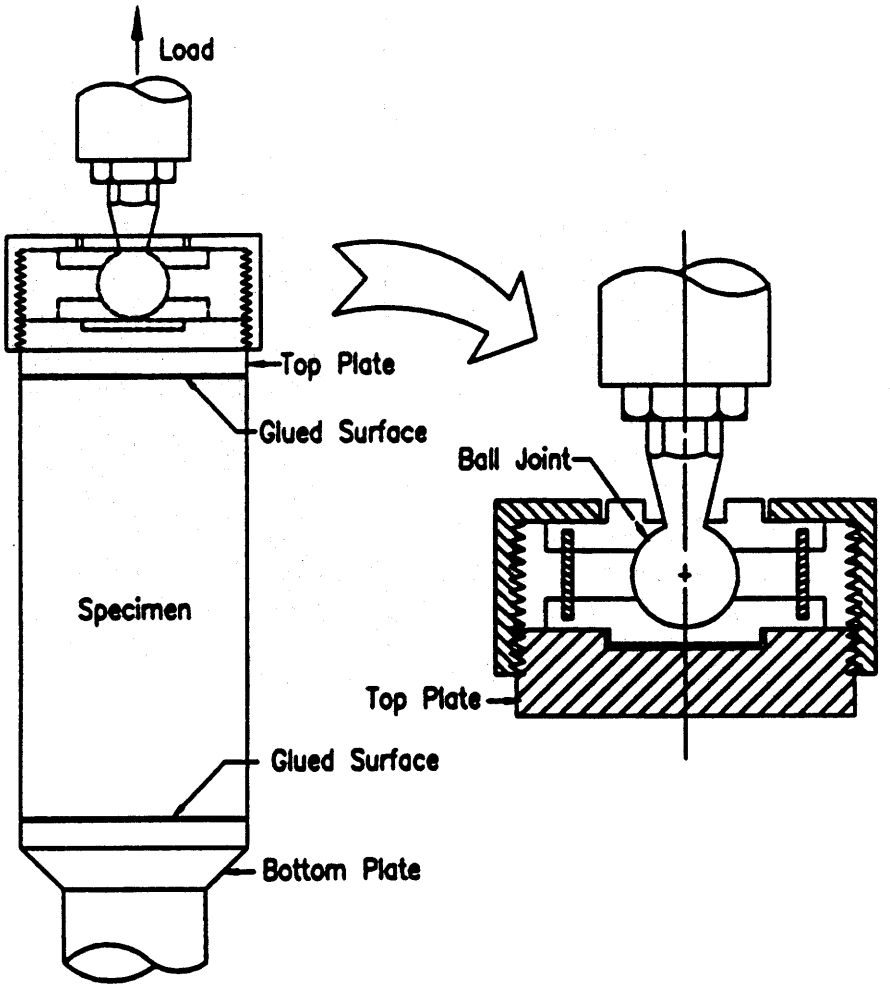

Figure B.3 Schematic Diagram of the Uniaxial Apparatus.

In this research, several data acquisition programs for creep, relaxation, and cyclic loading tests were developed using LabView graphical language developed by National Instrument. The data acquisition program collects the transducer voltages from axial deformation, load cell, and two extensometers, and records them in a plain text file format. The values of the transducer voltages are then converted into engineering values.

Stresses and strains used in the analysis were nominal (average) values calculated from the following equations:

$$\sigma = \frac{P}{A_0} \quad , \qquad \varepsilon = \frac{u}{L} \tag{B.34}$$

where P = load,
u = displacement,
A_0 = cross-sectional area of the sample, and
L = initial gauge length.

Uniaxial tensile creep, relaxation, and complex modulus tests were conducted at five different temperatures (ranging between -5 and 33°C) to obtain the viscoelastic material properties of the two mixtures. All other tests were conducted at 25°C. Uniaxial constant-strain-rate monotonic testing was conducted by controlling displacement measured from the 20.32-cm (8-in) gauge length. Then, in an attempt to validate the applicability of the correspondence principle to cyclic loading conditions, controlled-stress cyclic testing was performed at a relatively low stress amplitude to minimize any significant damage in the specimen. In order to characterize the damage growth and healing in asphalt concrete under cyclic loading for different control modes, controlled-stress and controlled-strain cyclic tests with and without rest periods were conducted with various loading amplitudes. Finally, for the verification of the constitutive model, multi-level cyclic loading tests with random durations of rest were performed. A haversine wave with 0.1 second loading time was used in cyclic loading.

Creep, Relaxation, and Complex Modulus Tests

Creep, relaxation, and complex modulus tests (ASTM D3497-79) were performed on several specimens at -5, 5, 15, 25, and 33°C to obtain thermoviscoelastic properties of the materials, such as creep compliance, relaxation modulus, dynamic modulus, and time-temperature shift factors. To minimize variation due to the inherent differences from sample to sample, a series of tests was performed on each individual specimen. First a creep test, then a relaxation test followed by a complex modulus test was performed on each specimen at each test temperature, increasing from -5°C to 40°C. A minimum 2-hour recovery period was allowed between tests. In the complex modulus tests, a haversine wave form at five different frequencies varying from 40Hz to 1Hz was applied to each specimen. Detailed test parameters are given in Table B.2.

Since the same specimen underwent various combinations of tests and temperatures, a relatively low stress/strain level was applied to the specimen to ensure negiligible damage during the entire testing period. The load/deformation level was reduced when testing was performed at higher temperatures. To check the extent of damage accumulated in the specimens during a series of tests, an additional creep test was performed at 25°C after all the tests were completed as a rheological fingerprint. It was found that the first creep compliance at 25°C is essentially the same as the second one, indicating a negligible change in the rheological properties during a series of tests. The specimens were conditioned to the testing temperatures for a minimum of 6 hours, except at 33°C where no more than 3-hours was allowed to minimize the hardening effect.

Table B.2 Creep, Relaxation, and Complex Modulus Test Parameters

Mixture	Creep		Complex Modulus		Relaxation	
	Temp. (°C)	Load (lbs)	Temp. (°C)	Amp. (lbs)	Temp. (°C)	Displ. (in)
A A D	- 5	300	5	200	5	0.001
	5	200	25	35	25	0.0005
	15	80	40	10	40	0.0001
	25	35	Frequencies (Hz): 1, 2, 5, 10, 20			
	33	5				
A A M	- 5	300	- 5	300		
	5	200	5	200		
	15	80	15	80		
	25	35	25	50		
	33	5	33	20		
			Frequencies (Hz): 2.5, 5, 10, 20, 40			

Constant-Strain-Rate Monotonic Test

A series of constant-strain rate monotonic loading tests with varying strain rates was performed to study the applicability of the correspondence principle to dealing with rate-dependence of the material. Four strain rates ranging from 0.0005 units/second to 0.0032

units/second were used in the tests. The tests were performed until the specimens failed. The axial deformations were calculated by multiplying the elapsed time by the constraint strain rate.

Test results are presented in Figures B.4(a) and B.4(b) for AAD and AAM mixtures, respectively. As can be seen in these figures, the stress responses for a specific strain level are strongly dependent upon the strain rates. Test data only up to the ultimate strength are presented and will be used in our analysis. Severe localization in deformation behavior can occur in each specimen beyond the ultimate load level until the specimen fails completely. Therefore, nominal stresses and strains after the ultimate load may no longer be adequate to describe the inelastic behavior of the specimen because the specimen can no longer be considered as a macroscopically homogeneous continuum.

Cyclic Loading Tests

In the cyclic loading tests, three types of loading histories were used for different purposes. These loading histories are summarized in the following:

1. Constant stress/strain amplitude cyclic loading histories without rest periods to model damage growth and hysteretic behavior of the material.

2. Constant stress/strain amplitude cyclic loading histories with rest periods for modeling of microdamage healing of the material.

3. Cyclic loading histories with multi-level stress/strain amplitudes and random durations of rest for the validation of the constitutive model developed from "a" and "b".

The loading histories "a"and "b" are presented in Figures B.5(a) and B.5(b), respectively.

1. Constant Amplitude Cyclic Loading Tests Without Rest Periods

The loading history "a" was used in this test to model damage growth in asphalt concrete. In order to characterize the short, intermediate, and long-term fatigue damage of asphalt concrete, three different stress/strain amplitudes were experimentally determined so that the specimens fail at approximately 5,000, 30,000, and 300,000 cycles.

It was impossible to collect all the load/deformation data up to failure in cyclic loading tests because of the limitation in computer memory capacity. Thus, only a limited number of data sets were collected at different stages of fatigue based on a logarithmic time scale. In each data set, load/deformation measurements were collected for 60 cycles (i.e., 6 seconds), with 20 data points per cycle.

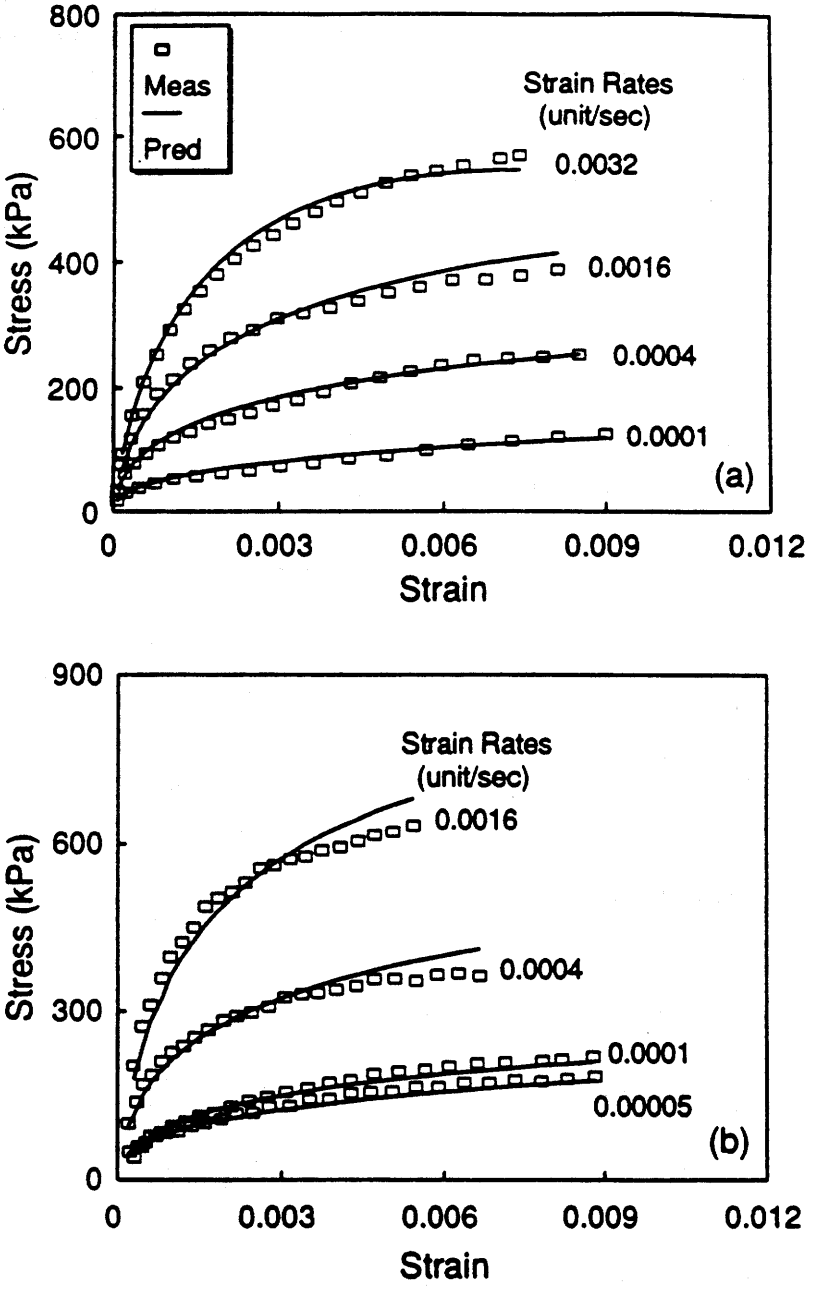

Figure B.4 Stress-strain Behavior at Various Strain Rates: (a) AAD Mixture; (b) AAM Mixture.

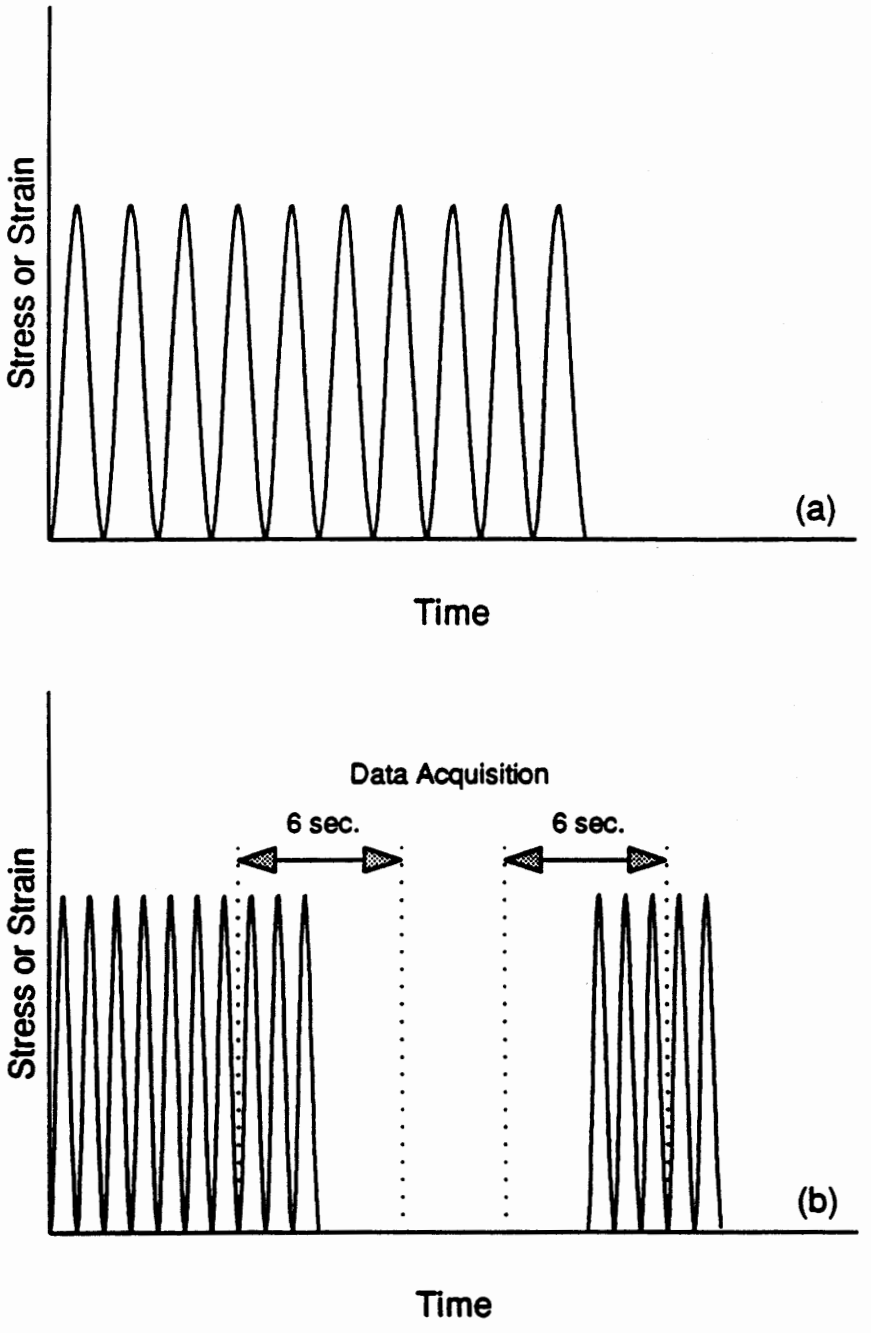

Figure B.5 Constant Strain Amplitude Cyclic Loading Histories: (a) Without Rest Periods; (b) With Rest Periods.

The data obtained from the short- and long-term fatigue tests were used in the characterization of the constitutive model, while the intermediate-term fatigue test data were used in the verification of the constitutive model. The fatigue lives obtained from the controlled-strain and -stress cyclic loading tests without rest periods are summarized in Tables B.3 and B.4, respectively.

2. Constant Amplitude Cyclic Loading Tests With Rest Periods

The loading history "b" was designed to evaluate and model the microdamage healing. The high and medium stress/strain amplitudes used in "a" were used in these tests. Seven different rest durations (0.5, 1, 16, 32, 120, 480, 1920 seconds) were randomly introduced between repetitive loading groups to minimize the effects of the sequence of the rest periods. The number of cycles in a loading group between two rest periods should be large enough to eliminate the effects of the previous rest period on the current rest period, and should create some additional damage in the specimen. With these issues in mind, three sequences of loading and rest periods were carefully designed. Typical sequences of loading and rest periods are presented in Table B.5. After applying these three sequences of loading and rest periods to the specimen, a continuous loading was applied until the specimen failed.

Like constant amplitude cyclic loading tests without rest periods, only a limited number of data sets were collected. The acquired data included 3 seconds of loading and 3 seconds of rest period data at the beginning and at the end of each loading group as illustrated in Figure B.5(b). The fatigue lives obtained from the controlled-strain and -stress cyclic loading tests with rest periods are summarized in Tables B.3 and B.4, respectively.

The loading history "c" was designed to validate the constitutive model developed in this research. Details on this loading history will be discussed later.

Table B.3 Summary of Average Fatigue Lives for Controlled-Strain Cyclic Tests

Mixture	Strain Amp. (unit)	N_f (cycles)	
		w/o Rest	w/ Rest
AAD	0.0014	2,850	13,000
	0.0009	28,500	N/A
	0.0006	170,000	N/A
AAM	0.0014	4,250	N/A
	0.001	38,800	71,000
	0.0007	130,500	N/A

N/A: Not available.

Table B.4 Summary of Average Fatigue Lives For Controlled-Stress Cyclic Tests

Mixture	Stress Amp. (kPa)	N_f (cycles)	
		w/o Rest	w/ Rest
AAD	121	4,250	12,300
	60	38,800	99,700
	33	223,700	N/A
AAM	247	4,800	18,500
	192	10,300	31,200
	66	351,000	N/A

Table B.5 Typical Sequences of Loading and Rest Period

No.	1st Sequence		2nd Sequence		3rd Sequence	
	No. of Cycles	Duration of Rest (sec)	No. of Cycles	Duration of Rest (sec)	No. of Cycles	Duration of Rest (sec)
1	500		2000		2000	
2		16		32		480
3	500		500		500	
4		480		120		1920
5	500		500		500	
6		120		16		1
7	500		500		500	
8		1		1		16
9	500		500		500	
10		32		1920		0.5
11	500		500		500	
12		0.5		480		32
13	500		500		500	
14		1920		0.5		120

Determination of Viscoelastic Material Properties

Since the relaxation function E(t) is an essential mechanical property for the calculation of pseudo strain given in (B.13), the relaxation modulus was predicted from the creep compliance. In order to convert the creep compliance to the relaxation modulus, an analytical representation of the creep response needs to be established a priori. The relaxation modulus is then predicted from the creep compliance through theory of linear viscoelasticity. In the following sections, several analytical representations of the creep response, such as the pure power law, the modified power law, and the Prony series representation, are discussed. The conversion of the creep compliance to relaxation modulus is then described. Finally, the interrelationship between the relaxation modulus and dynamic modulus are presented. Although the relaxation modulus is the mechanical property function used in the linear viscoelastic stress-strain relationship (B.11), sometimes the

mechanical response of the material can be more easily characterized in terms of the dynamic modulus, such as the steady-state vibration response.

Conversion of Creep Compliance to Relaxation Modulus

Since asphalt concrete is a *thermorheologically simple* material, the time- and temperature-dependent creep response can be represented by a single parameter, so-called *reduced time*, through time-temperature superposition principle. The creep master curves for two mixtures are presented in Figure B.6. The master curve for each mixture was constructed by horizontally shifting the creep curves at various temperatures to the creep curve at a reference temperature of 25°C. *Time-Temperature shift factors* a_T at different temperatures were obtained from the above shifting process and their dependency on temperature is illustrated in Figure B.7.

Several power laws can be used to analytically represent the master creep curve. The importance of using a power form that accurately represents the data in the entire time range was demonstrated by Kim et al. (1995). The pure power law (PPL) has been commonly used in representing time-dependent behavior of asphalt binder or mixture because of its simplicity, such that

$$D(\xi) = D_1 \xi^m \tag{B.35}$$

where $D(\xi)$ = master creep function corresponding to a certain reference temperature, and ξ = reduced time. For a constant temperature, the reduced time is defined as

$$\xi \equiv \frac{t}{a_T} \tag{B.36}$$

where a_T = time-temperature shift factor. The PPL in (B.35) may be good enough to compare the time-dependence of different materials; however, when the creep compliance is used in viscoelastic modeling, the PPL under-estimates and over-estimates the compliance at short and long loading times, respectively. For notational simplicity, the reduced time will be denoted by t, and the master creep function $D(\xi)$ and the master relaxation function $E(\xi)$ will be denoted by D(t) and E(t), respectively, unless otherwise noted.

If the entire time range of a material's behavior is needed, an analytical representation that can represent the creep data over a broader time scale should be used. This can be accomplished with either the modified power law (MPL) in equation (B.37) or the Prony series representation (often referred to as *generalized Voigt model* or *Kelvin model*) given in equation (B.38).

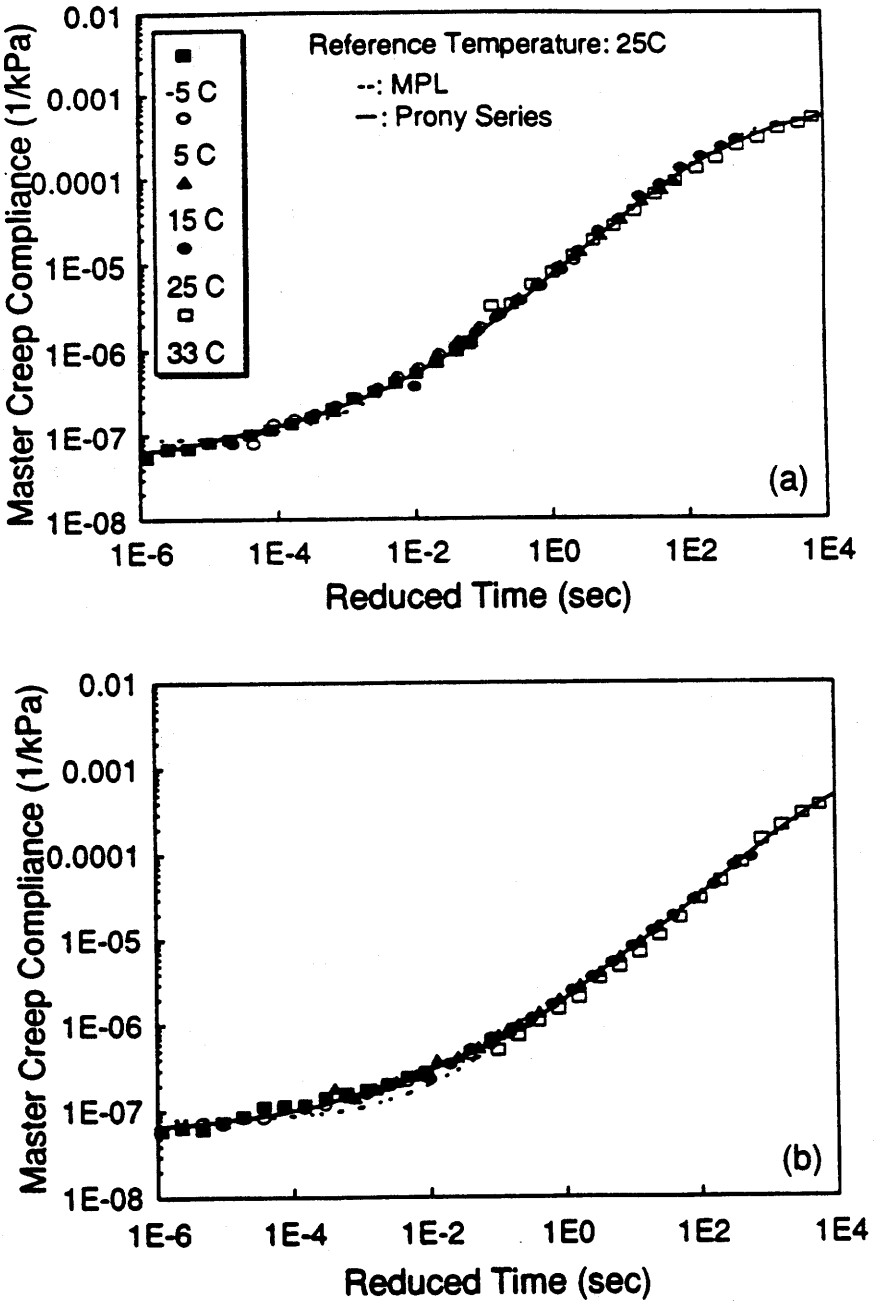

Figure B.6 Master Creep Curves at a Reference Temperature: (a) AAD Mixture; (b) AAM Mixture.

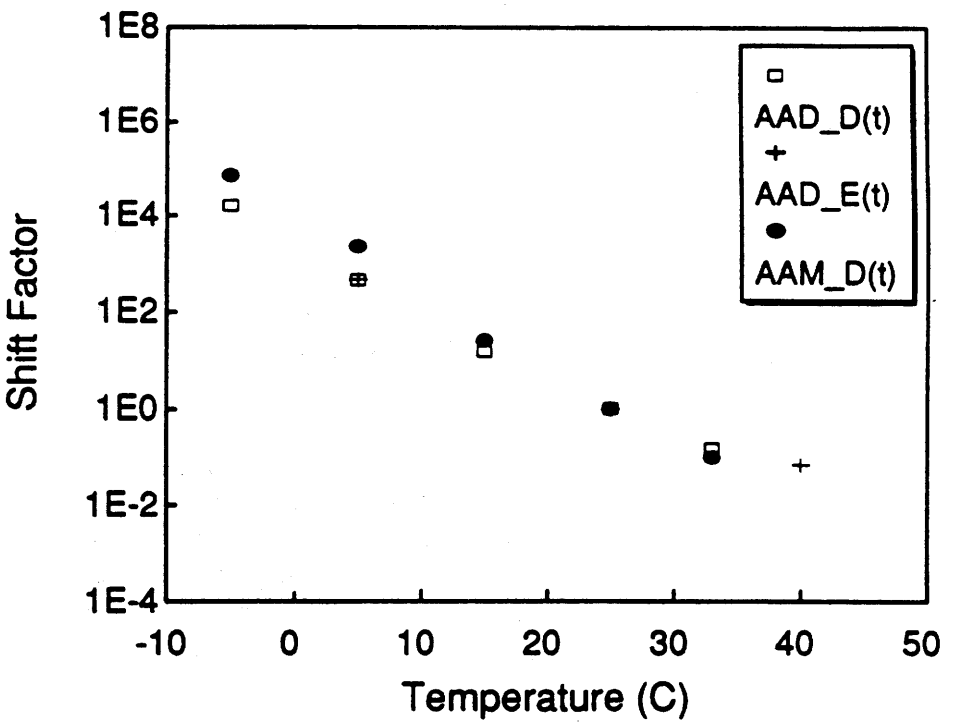

Figure B.7 Time-Temperature Shift Factors.

$$D(t) = D_0 + \frac{D_\infty - D_0}{(1 + \frac{\tau_0}{t})^n} \quad \text{(B.37)}$$

where D_0 = creep compliance at t = 0,
D_∞ = creep compliance at t = ∞,
τ_0 = time constant, and
n = slope of the middle linear portion of D(t) versus time curve in a logarithmic scale.

$$D(t) = D_0 + \sum_{i=1}^{M} D_i(1 - e^{-\frac{t}{\tau_i}}) \quad \text{(B.38)}$$

where τ_i = retardation time of the i^{th} Voigt element, and
D_0, D_i = material constants.

As can be seen in Figure B.6, both the MPL and Prony series successfully fit the measured creep data: however, the Prony series can fit the data more accurately than the MPL does, especially at short loading times. The prony series representation also has more efficiency in mathematical operation than the MPL. Therefore, the Prony series representation was adopted in this study to analytically represent the creep and relaxation curves.

There are different ways to find the model constants in the Prony series. One can minimize the square error between the measured creep data and the analytical representation. Another common approach to curve fitting is to equate the measured data and the analytical representation at several points. This matching procedure is so-called *collocation* method, and is the one used in this study. This collocation method is well reviewed by Huang (1993). The model constants in equation (B.38) for AAD and AAM mixtures are provided in Table B.6.

Prony series expression of the relaxation modulus is given as

$$E(t) = E_\infty + \sum_{i=1}^{N} E_i e^{-\frac{t}{\rho_i}} \quad \text{(B.39)}$$

where E_∞ is the long-time equilibrium modulus, E_i's are regression constants, and ρ_i's are relaxation times. This form is often referred as the *generalized Maxwell model* or *Wiechert model*.

Table B.6 Constants Used in the Prony Series Representation of Creep Compliance in Equation (B.38)

i	AAD		AAM	
	τ_i	D_i (1/kPa)	τ_i	D_i (1/kPa)
0	-	6.48E-08(D_0)	-	6.89E-08 (D_0)
1	1.00E-05	2.99E-08	5.00E-06	9.61E-09
2	1.00E-04	4.40E-08	5.00E-05	1.63E-08
3	1.00E-03	9.12E-08	5.00E-04	4.92E-08
4	1.00E-02	2.50E-07	5.00E-03	1.12E-07
5	1.00E-01	7.17E-07	5.00E-02	2.26E-07
6	1.00E+00	4.45E-06	5.00E-01	5.75E-07
7	1.00E+01	2.06E-05	5.00E+00	3.53E-06
8	1.00E+02	1.18E-04	5.00E+01	8.91E-06
9	1.00E+03	2.38E-04	5.00E+02	6.24E-05
10	1.00E+04	2.39E-04	5.00E+03	3.85E-04
11	1.00E+05	2.83E-04	5.00E+04	3.92E-04

Inasmuch as the uniaxial constitutive equation in (B.11) for linear viscoelastic media is valid for general strain histories, it can be expressed in terms of stress and strain in a creep test. The definition of creep compliance suggests that the strain history, $\varepsilon(t)$, measured in the creep test is the response to a unit stress input. Thus, equation (B.11) can be rewritten as:

$$1 = \int_0^t E(t-\tau)\frac{dD(\tau)}{d\tau}d\tau \qquad for\ t>0 \tag{B.40}$$

Equation (B.40) allows one to predict the relaxation modulus from the creep compliance. This prediction can be accomplished in different ways.

A direct numerical method can be used to calculate the values of the relaxation modulus from the measured creep data. In general, a very short time interval Δt is required to obtain an accurate prediction of the relaxation modulus because of the significant change in creep response

at short loading times. As a result, this method requires a long computation time.

Alternatively, taking Laplace transform of equation (B.40) yields

$$\tilde{E} = \frac{1}{\tilde{D}} \tag{B.41}$$

where $\tilde{f} = s\,\bar{f}$ = the Carson transform of f(t), $\bar{f}$ is the Laplace transform of f, and s is a real constant. The Carson transforms of D(t) and E(t) are, respectively,

$$\tilde{D} = D_0 + \sum_{i=1}^{M} \frac{D_i}{s\tau_i + 1} \tag{B.42}$$

and

$$\tilde{E} = E_\infty + \sum_{i=1}^{N} \frac{E_i s}{s + \frac{1}{\rho_i}} \tag{B.43}$$

Substituting equations (B.42) and (B.43) into equation (B.41) results in the following useful relationships between creep and relaxation coefficients when s becomes 0:

$$M = N \tag{B.44}$$

$$\frac{1}{E_\infty} = D_0 + \sum_{i=1}^{M} D_i \tag{B.45}$$

The remaining coefficients, E_i's, can be determined as follows:

1. calculate values of $1/\tilde{D}$ (i.e., $\tilde{\varepsilon}$ in equation (B.43)) at M different s values.
2. assume approximate values of relaxation times ρ_i (i=1,2,...,N).
3. obtain E_i's by minimizing square error between the values of $1/\tilde{D}$ and mathematical expression of $\tilde{\varepsilon}$ in equation (B.43).
4. get E(t) by substituting E_∞, E_i and ρ_i into equation (B.39).

The ρ_i may be specified in many different ways and normally be separated by no more than one decade to obtain a smooth curve.

Table B.7 Constants Used in the Prony Series Representation of Relaxation Modulus in Equation (B.39)

I	AAD		AAM	
	ρ_i	E_i (1/kPa)	ρ_i	E_i (1/kPa)
0	-	1106 (E_∞)	-	1172 (E_∞)
1	1.20E-05	5.87E+06	2.20E-05	3.10E+06
2	1.20E-04	3.64E+06	2.20E-04	4.31E+06
3	1.20E-03	3.34E+06	2.20E-03	3.46E+06
4	1.20E-02	1.94E+06	2.20E-02	2.02E+06
5	1.20E-01	5.39E+05	2.20E-01	1.27E+06
6	1.20E+00	7.27E+04	2.20E+00	2.72E+05
7	1.20E+01	1.99E+04	2.20E+01	6.59E+04
8	1.20E+02	3.65E+03	2.20E+02	1.45E+04
9	1.20E+03	1.43E+03	2.20E+03	1.52E+03
10	1.20E+04	6.99E+02	2.20E+04	7.10E+02
11	1.20E+05	2.90E+02	2.20E+05	5.88E+01

The predicted relaxation modulus for AAD mixture was plotted with the measured values in Figure B.8(a). At times longer than 10 seconds, it is difficult to compare the predicted and the measured data because of the limitation in the resolution of the data acquired. In general, a good match is observed between the predicted and the measured data that demonstrates the validity of the prediction scheme. Therefore, the relaxation testing was not performed on AAM specimens, and the predicted relaxation modulus is presented in Figure B.8(b). The model constants in (B.39) for the predicted relaxation modulus data shown in Figure B.8 are provided in Table B.7. These values are used in all the analysis performed in this study.

For the AAD mixture, the shift factors calculated from the relaxation data are compared with those obtained from creep data in Figure B.6. An excellent agreement of the factors from the creep and relaxation data proves the validity of these factors. These shift factors will be used in the conversion of the creep compliance to the dynamic modulus as a means of predicting mechanical behavior at various temperatures from the one measured at the reference temperature.

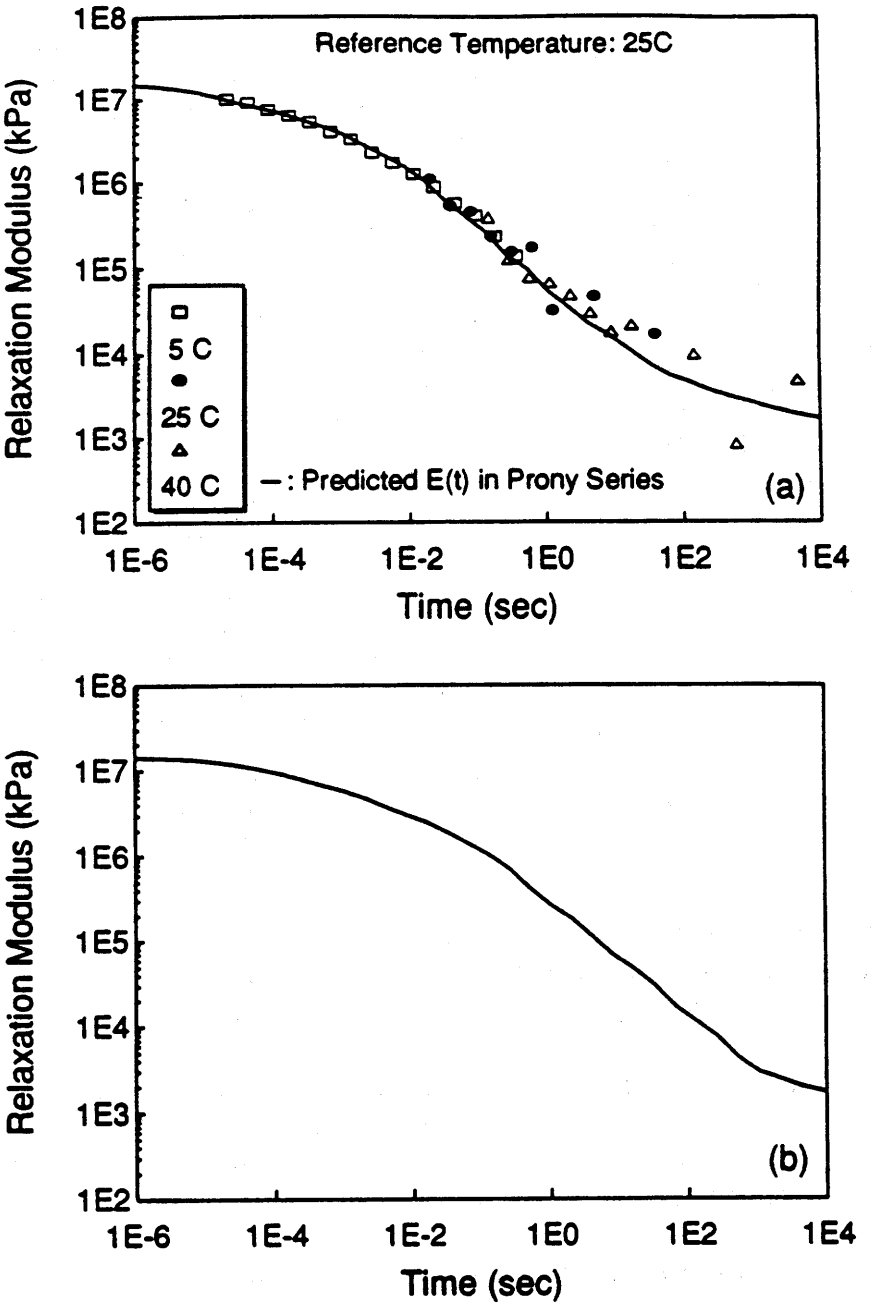

Figure B.8 Master Relaxation Curves at a Reference Temperature: (a) AAD Mixture; (b) AAM Mixture.

Conversion of Creep Compliance to Dynamic Modulus

It is known for a linear viscoelastic, non-aging material that

$$E^* \times D^* = 1 \tag{B.46}$$

The complex compliance D* is defined as

$$D^* = D' - iD'' \tag{B.47}$$

where D' and D" are the storage compliance and the loss compliance, respectively. Substituting the definitions of the complex modulus and complex compliance (B.47) into (B.46) yields

$$E' = \frac{D'}{|D^*|^2} \tag{B.48}$$

$$E'' = \frac{D''}{|D^*|^2} \tag{B.49}$$

where

$$|D^*| = [(D')^2 + (D'')^2]^{1/2} \tag{B.50}$$

Therefore, the determination of the dynamic modulus |E*| and phase angle ϕ reduces to calculating the storage and loss compliances, D' and D".

It can be shown by the theory of linear viscoelasticity that

$$D^* = \tilde{D}|_{s=i\omega} \tag{B.51}$$

where $\tilde{D}$ = Carson transform of D(t), and
ω = angular velocity equal to 2π multiplied by frequency f.

$$D^* = D_0 + \sum_{i=1}^{M} \frac{D_i}{i\omega\tau_i + 1} \tag{B.52}$$

Substituting the Carson transform of D(t) given in (B.42) into (B.51) yields

$$D' = D_0 + \sum_{i=1}^{M} \frac{D_i}{\omega^2 \tau_i^2 + 1} \tag{B.53}$$

and

$$D'' = \sum_{i=1}^{M} \frac{\omega \tau_i D_i}{\omega^2 \tau_i^2 + 1} \tag{B.54}$$

As discussed earlier, since the time and temperature effects were expressed in terms of the reduced time in the creep compliance, ω in the above equations (B.52)-(B.54) should be interpreted as *reduced frequency*, ζ, defined as follows (Christensen, 1982):

$$\zeta = \omega a_T \tag{B.55}$$

where a_T is the time-temperature shift factor. This equation states that a_T obtained from creep or relaxation data can be used in the determination of the reduced frequency. Now, the dynamic modulus $|E^*|$ and phase angle ϕ at various temperatures can be calculated using (B.48), (B.49), (B.53), and (B.54) with (B.55) from the Prony series representation of the creep compliance.

Using individual dynamic modulus curves at various temperatures, the master dynamic modulus curves were constructed at the reference temperature of 25°C and presented in Figure B.9 for different mixtures. The shift factors obtained from the creep data shown in Figure B.7 were used in this shifting process. Also the dynamic moduli were predicted according to the conversion scheme described above, and illustrated as the continuous lines in this figure.

As can be seen in Figure B.9, the dynamic moduli were predicted up to the frequency value of 80,000Hz because the measured creep compliance values were not available above that frequency limit. That is, there is an approximate relationship between time and frequency (Sias, 1996) that

$$f = \frac{0.08}{t} \tag{B.56}$$

Using this approximate relationship, one can determine a frequency value that corresponds to a certain loading time. The shortest loading time of the measured creep compliance is 1E-6 seconds, and then the corresponding frequency to this loading time is 80,000Hz based on equation (B.56). Thus, the dynamic moduli were predicted from the measured creep compliance up to the frequency value of 80,000Hz.

Although, the complete master curves were not obtained because of the insufficient data, in general, a good agreement between the measured and predicted moduli is found, which proves the validity of the conversion scheme introduced in this section. Comparing Figures B.9(a) and B.9(b), the AAD mixture shows higher stiffness especially at lower frequencies (or higher temperatures) and more time-dependent behavior (i.e., a greater change in the dynamic modulus as a function of frequency) than the AAM mixture.

Experimental Study of Correspondence Principle

Calculation of Pseudo Strain Using Superposition

Pseudo strain is an essential parameter for applying Schapery's correspondence principle (1984) to the hysteretic stress-strain behavior of asphalt concrete. As shown in equation (B.13), the value of pseudo strain at current time t is a function of the relaxation modulus E(t) and the strain history $\varepsilon(t)$ from time zero to time t. As was discussed earlier, it is impossible, or at least extremely impractical, to acquire all the stress-strain data in cyclic loading tests up to failure because of the limitation in computer memory capacity. An alternate way to calculate the pseudo strain is to present the relaxation modulus and the strain as analytical functions of time and integrate the product of these functions. Therefore, the strain histories used in the calculation of pseudo strains are generated from a limited number of data sets that were collected at different stages of fatigue testing. Strains that were not measured were interpolated using the measured strain values.

A superposition technique was employed to analytically represent the strain histories in the cyclic loading tests. This approach is valid because the definition of pseudo strain in equation (B.13) is linear: that is, it satisfies the homogeneity and superposition properties in equations (B.1) and (B.2), respectively. In this section, an analytical solution of pseudo strain under constant-strain-monotonic loading is first described. A closed form solution of pseudo strain is then derived for the multi-level cyclic strain history under the controlled-strain mode. Also, an approach of calculating pseudo strain values for more sophisticated strain responses under the controlled-stress mode is described at the end of this section.

Under Constant-Strain-Rate Monotonic Loading

For constant-strain-rate monotonic loading, the strain history at current time t is

$$\varepsilon(t) = CtH(t) \tag{B.57}$$

where C is a constant strain rate, and H(t) is heaviside step function that H=0 when t<0, and H=1 when t>0. Using the first derivative of the strain function (B.57) and the relaxation modulus represented by the Prony series (B.39), the pseudo strain can be obtained from (B.13):

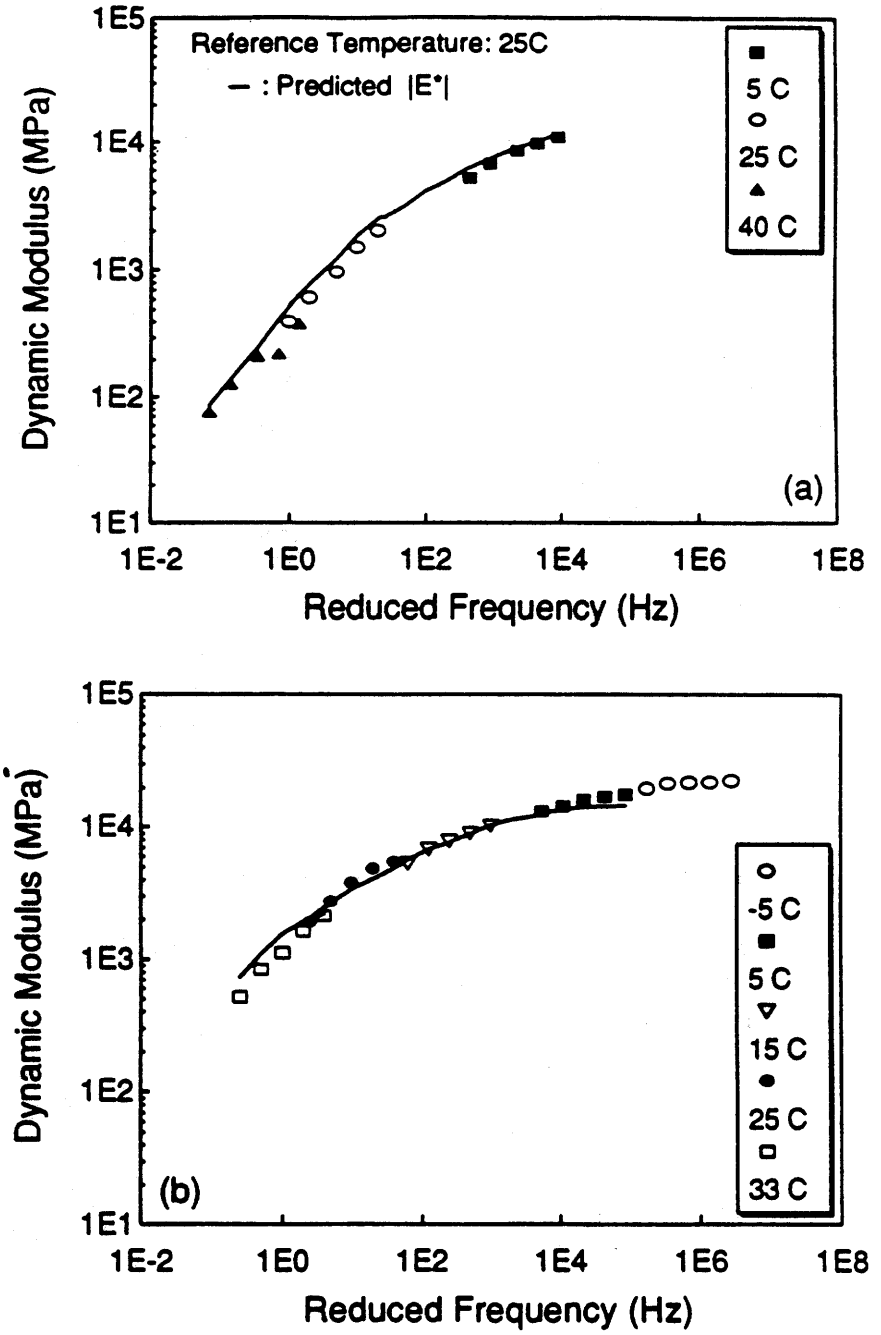

Figure B.9 Master Dynamic Modulus Curves at a Reference Temperature: (a) AAD Mixture; (b) AAM Mixture.

$$\varepsilon^R(t) = \frac{C}{E_R}[E_\infty t + \sum_{i=1}^{N} E_i \rho_i (1 - e^{-t/\rho_i})] \qquad \text{(B.58)}$$

Under Controlled-Strain Cyclic Loading

The multi-level cyclic strain history with rest periods presented in Figure B.10 can be simply represented in an analytical function composed of a step loading function ε_1 and a harmonic sinusoidal function ε_2 based on the superposition principle in equation (B.2). In this figure, the first loading group is the strain history between time t=0 and t=t_1. Similarly, the N^{th} loading group is the strain history between time t=t_{2N-2} and t=t_{2N-1}. The analytical representations of those two strain components, ε_1 and ε_2, at time t in the N^{th} loading group are given in (B.59) and (B.60), respectively.

$$\varepsilon_1(t) = \varepsilon_{0,1} H(t) - \varepsilon_{0,1} H(t - t_1) + \varepsilon_{0,2} H(t - t_2) - \ldots + \varepsilon_{0,N} H(t - t_{2N-2}) \qquad \text{(B.59)}$$

$$\begin{aligned} \varepsilon_2(t) = {} & \varepsilon_{0,1} \sin(\omega t + \theta_1)[H(t) - H(t - t_1)] + \varepsilon_{0,2} \sin(\omega t + \theta_2) H(t - t_2) \\ & - \ldots + \varepsilon_{0,N} \sin(\omega t + \theta_N) H(t - t_{2N-2}) \end{aligned} \qquad \text{(B.60)}$$

where $\varepsilon_{0,N}$ = strain amplitude in the N^{th} loading group,
ω = angular velocity, and
θ_N = regression constants.

Using the definition of pseudo strain (B.13), the respective pseudo strains for the strain inputs, ε_1 and ε_2, at current time t in the N^{th} loading group were obtained and provided in (B.61) and (B.62).

$$\varepsilon_1^R(t) = \frac{1}{E_R}[\sum_{i=1}^{N-1} \varepsilon_{0,i}(E(t - t_{2i-2}) - E(t - t_{2i-1})) + \varepsilon_{0,N} E(t - t_{2N-2})] \qquad \text{(B.61)}$$

$$\varepsilon_2^R(t) = \frac{1}{E_R}[\varepsilon_{0,N} |E^*| \sin(\omega t + \theta_N + \phi)] \qquad \text{(B.62)}$$

It is noted that the pseudo strain ε_2^R in equation (B.62) for the sinusoidal loading is only a function of current strain, while the pseudo strain ε_1^R in equation (B.61) for the step loading is a function of all the past strain history. For the simplicity of analysis, the value of 1 will be used for

the reference modulus E_R in the remaining analysis. Now, using the superposition property, the pseudo strain for the strain history presented in Figure B.10 can be determined by adding ε_1^R calculated from the first strain component ε_1 to ε_2^R calculated from the second strain component ε_2. Pseudo strains in the N^{th} loading group (i.e., $t_{2N-2} < t < t_{2N-1}$) can be calculated using the following equation:

$$\varepsilon^R(t) = \sum_{i=1}^{N-1} \varepsilon_{0,i}[E(t-t_{2i-2}) - E(t-t_{2i-1})] + \varepsilon_{0,N}E(t-t_{2N-2}) + \varepsilon_{0,N}|E^*|\sin(\omega t + \theta_N + \phi) \qquad \text{(B.63)}$$

As can be seen from this equation, the dynamic modulus and phase angle as well as relaxation modulus are required to calculate the pseudo strain.

In the fatigue characterization of asphalt concrete, which will be discussed in the following section, only the peak pseudo strain in each cycle is required. Whenever the sine function in equation (B.63) becomes 1, the pseudo strain reaches the peak pseudo strain in each cycle such that

$$\varepsilon_m^R(t) = \varepsilon_{0,N}|E^*| + \sum_{i=1}^{N-1} \varepsilon_{0,i}[E(t-t_{2i-2}) - E(t-t_{2i-1})] + \varepsilon_{0,N}E(t-t_{2N-2}) \qquad \text{(B.64)}$$

where ε_m^R is the peak pseudo strain in each cycle.

When constant strain amplitude of loading without rest periods is used as an input, equations (B.63) and (B.64) reduce to (B.65) and (B.66), respectively:

$$\varepsilon^R(t) = \varepsilon_0 E(t) + \varepsilon_0|E^*|\sin(\omega t + \theta + \phi) \qquad \text{(B.65)}$$

and

$$\varepsilon_m^R(t) = \varepsilon_0[|E^*| + E(t)] \qquad \text{(B.66)}$$

Thus, as long as the mechanical properties of the material and the strain amplitude are given, the peak pseudo strain at current time can be easily obtained from equation (B.66).

Under Controlled-Stress Cyclic Loading

Unlike the controlled-strain case, it is difficult in the controlled-stress mode to represent the strain history in an analytical function because the average strain and the strain amplitude in each cycle increase as cyclic loading continues due to the viscoelasticity and damage growth in

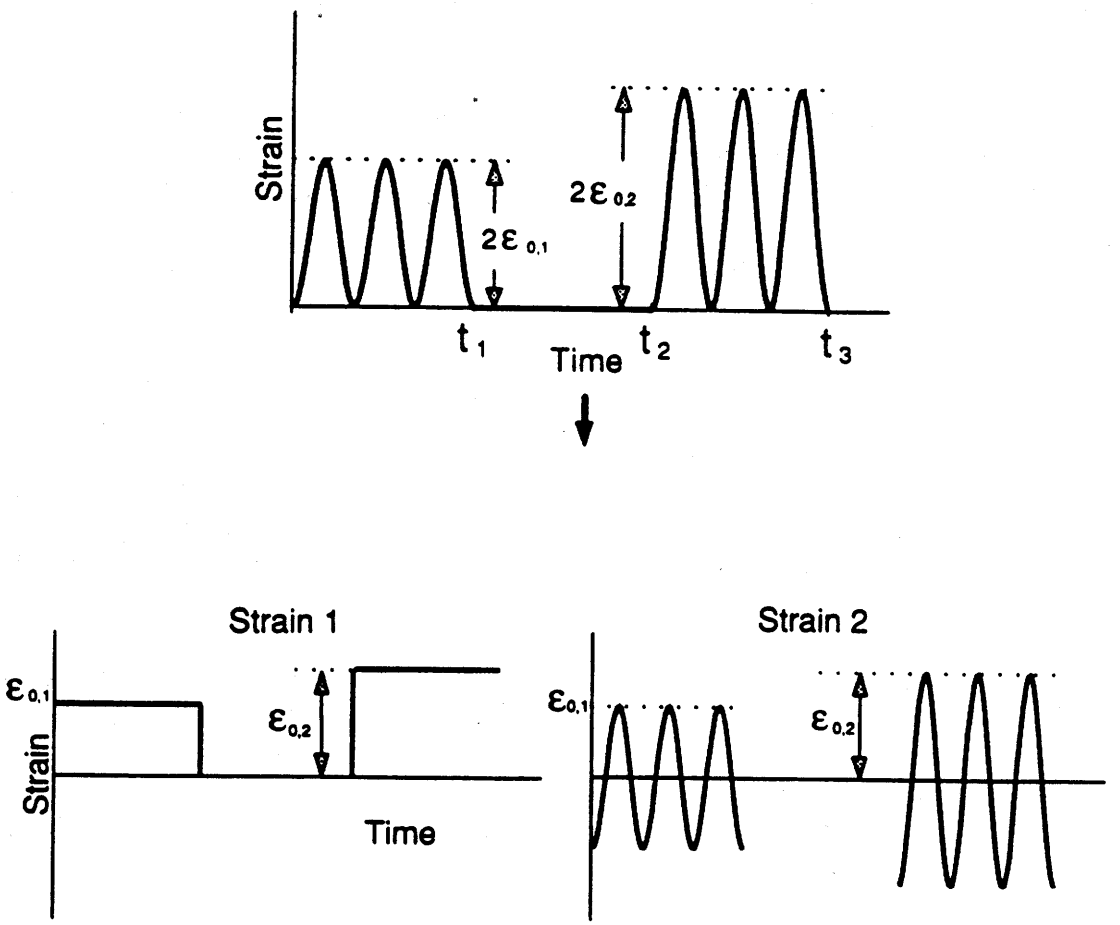

Figure B.10 Multi-level Strain History With Rest Periods.

asphalt concrete. Before discussing the multi-level cyclic loading history with rest periods, let us consider a simpler case, constant stress amplitude of cyclic loading without rest periods.

A typical strain response under constant stress amplitude of cyclic loading without rest periods is shown in Figure B.11(a), and can be separated into the following two strain components:

$$\varepsilon_1(t) = A + Bt^{\alpha} + \sum_{i=1}^{l} C_i t^i \tag{B.67}$$

$$\varepsilon_2(t) = \varepsilon_0(t) \sin(\omega t + \theta) \tag{B.68}$$

where $\varepsilon_0(t)$ is amplitude of strain response that is a function of time. A, B, C_i, α,θ are regression constants. l in equation (B.67) is a polynomial order whose typical values are in the range of 3 to 5. The strain components, ε_1 and ε_2, represent the average strain response and the sinusoidal strain response, respectively. The regression constants in the strain functions (B.67) and (B.68) can be obtained by minimizing the square error between the measured strain data and the analytical representations of strain history.

With the Prony series representation of relaxation modulus (B.39), obtaining a closed form solution of pseudo strain for the strain histories (equations (B.67) and (B.68)) is very difficult because of the power law in time in equation (B.67) and the amplitude function in equation (B.68). Thus, a numerical integration method was employed to calculate the pseudo strains. Using the superposition property, the total pseudo strain was determined by adding the pseudo strain calculated from the first strain component, ε_1, to the pseudo strain calculated from the second strain component, ε_2.

To validate this approach, the measured and the generated strains are compared in Figure B.11(a). Then, pseudo strain values were calculated for the entire loading history from the measured strains and from the generated strains using the superposition principle. A typical stress pseudo-strain curve is presented in Figure B.11(b). A good agreement between the pseudo-strains from the measured strains and from generated strains demonstrates the validity of this approach for the strain histories analyzed in this study.

For the multi-level cyclic loading with rest periods, the strain response is more complex than the constant level of cyclic loading without rest periods because of the strain recovery occurring during rest periods. After a detailed study of the experimental data, it was observed that the average strain responses under both loading and rest periods can be represented by equation (B.67), and the sinusoidal strain responses during loading periods can be represented by equation (B.68). Of course, there is no sinusoidal response during rest periods. To calculate the pseudo-strains, all regression constants in equations (B.67) and (B.68) were determined for each strain history during loading and rest periods, and then the numerical integration method was used.

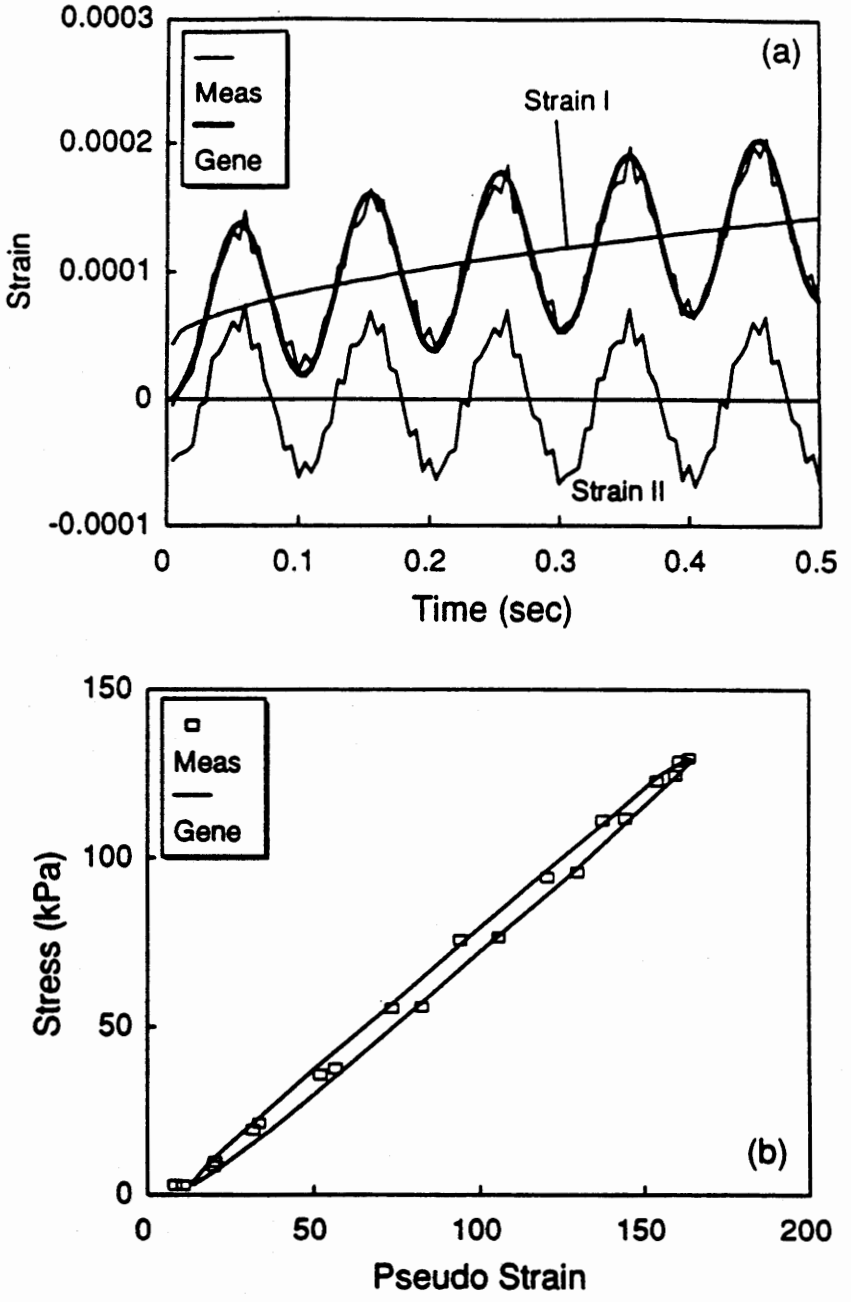

Figure B.11 Verification of the Prediction Method for Pseudo-strains in Long-term Fatigue Tests: (a) Strain-time; (b) Stress-pseudo Strain.

Experimental Verification of Correspondence Principle

Prior to constitutive modeling, the material's hysteretic behavior was studied with the application of the correspondence principle. Two types of uniaxial tensile testing were used in this task:

1. controlled-stress cyclic loading tests with rest periods.
2. constant-strain-rate monotonic loading tests with varying strain rates.

In the cyclic loading tests, a loading amplitude of 156 N (35 lbs) was used, which was low enough not to induce any significant damage. Typical hysteretic stress-strain behavior is presented in Figure B.12(a) at selected cycles. As expected, the stress-strain loops shift to the right-hand side with the reduction of dissipated energy determined from the area inside the stress-strain curve. In Figure B.12(b), the same stresses are plotted against pseudo strains. As can be seen from Figures B.12(a) and B.12(b), hysteretic behavior due to both loading-unloading and repetitive loading has disappeared using the pseudo strains, except the first cycle during which some minor adjustments occur within the test setup. It is also noted that the stress-pseudo strain behavior in Figure B.12(b) is linear.

The same approach was employed to investigate the applicability of the correspondence principle to accounting for the effect of rest period. Figure B.13(a) presents the hysteresis loops before and after a rest period of 8 seconds. Pseudo strains were calculated and displayed against the stresses in Figure B.13(b). The use of pseudo strain successfully accounts for the change in strain due to the relaxation during the rest period. Different lengths of rest periods were applied after cyclic loading and yielded the same conclusion.

Using the monotonic loading tests data shown in Figure B.4, pseudo-strains were calculated from equation (B.58) and plotted against σ/I in Figure B.14. The initial pseudo stiffness I, defined as the ratio of stress to pseudo strain at the early linear part of a stress-pseudo strain curve, was necessary to account for the effect of sample-to-sample variability. The curves representing different loading rates fall on the same line at lower stress levels, and then the discrepancy in the stress-pseudo strain curves among the different loading rates becomes greater. This behavior implies that the correspondence principle can successfully eliminate the rate dependency of the material when the damage is negligible. However, if a significant level of damage is induced in the sample, additional variables should be employed in a constitutive equation to represent the damage growth in the system. Additional results on experimental verification of the correspondence principle are documented by Kim et al. (1995) using uniaxial cyclic data of asphalt concrete under a wide range of test conditions.

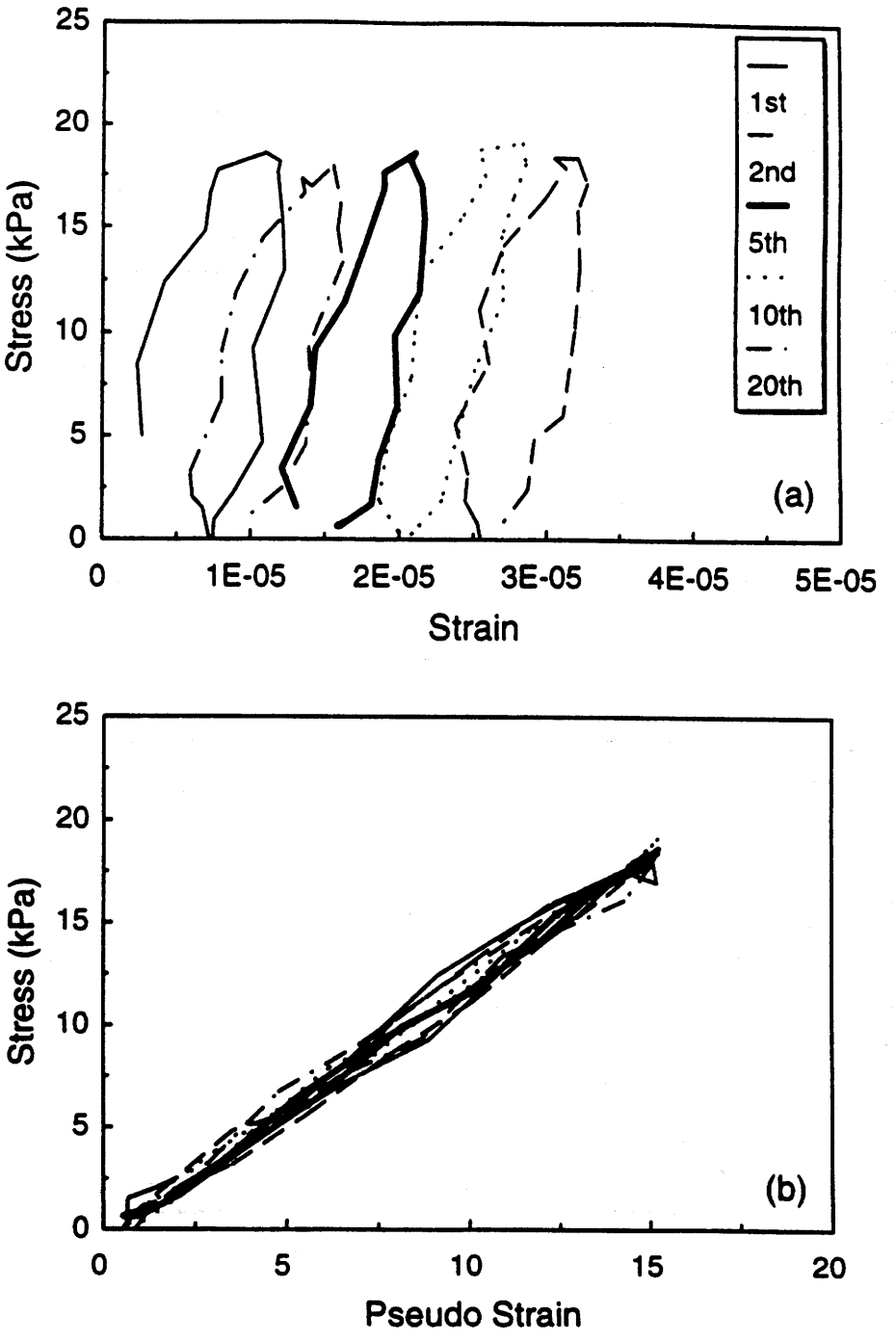

Figure B.12 Application of CP to Cyclic Data with Negligible Damage: (a) Stress-strain; (b) Stress-pseudo Strain.

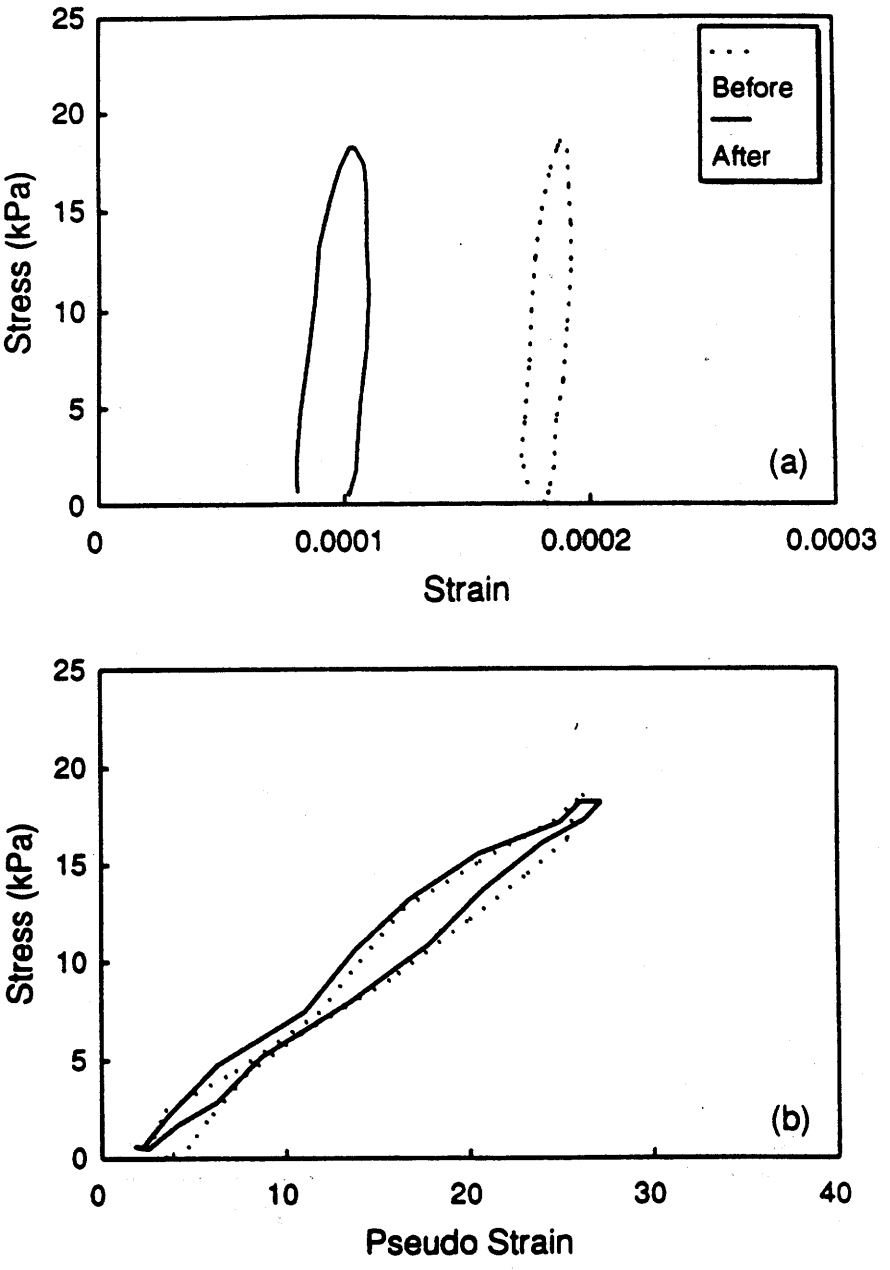

Figure B.13 Application of CP to Cyclic Data with Negligible Damage Before and Afer 8-sec Rest Period: (a) Stress-strain; (b) Stress-pseudo Strain.

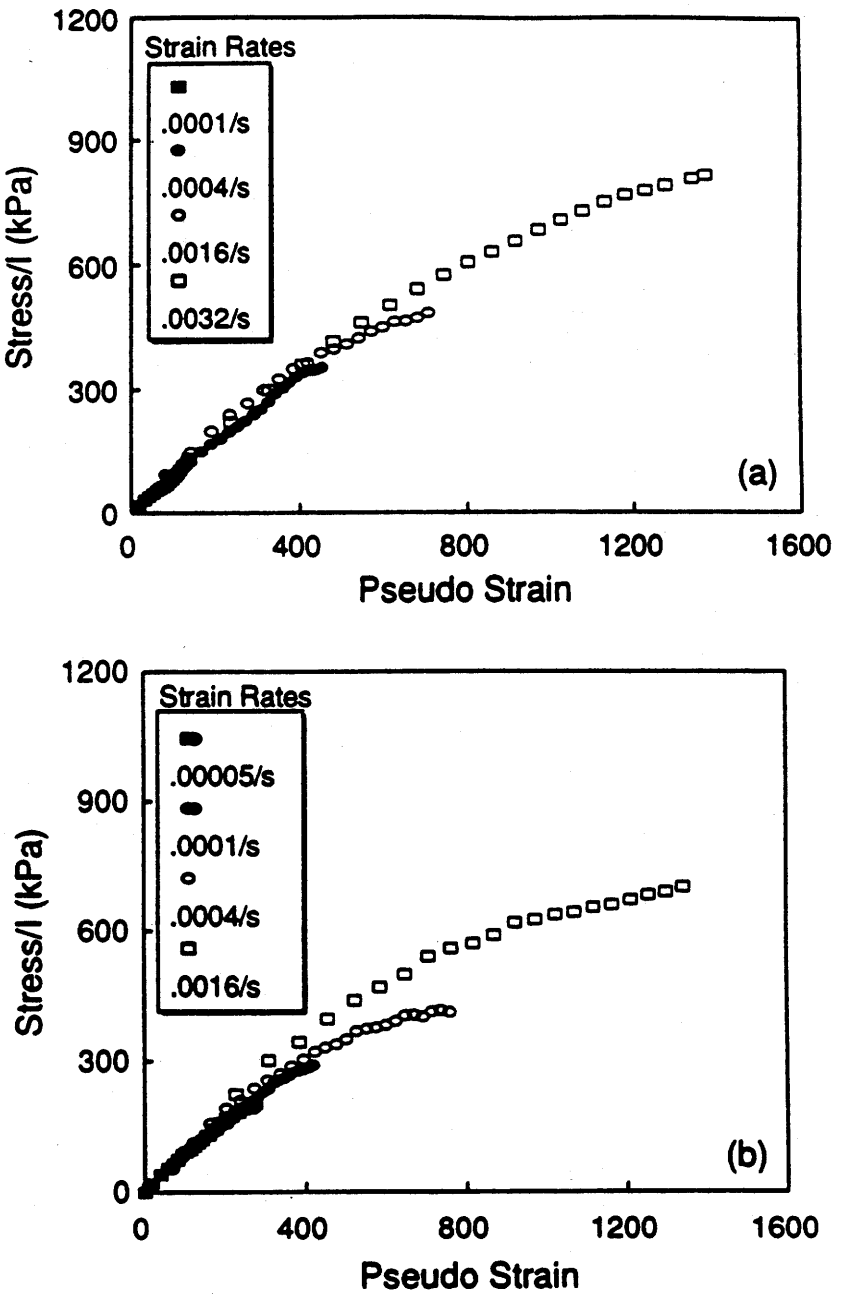

Figure B.14 Application of CP to Monotonic Data: (a) AAD Mixture; (b) AAM Mixture.

Constitutive Modeling of Asphalt Concrete With Growing Damage

Modeling the mechanical behavior of asphalt concrete considering both time-dependent damage growth and microdamage healing is a sophisticated problem. Therefore, a stepwise approach is adopted in this study. First, a constitutive model that accounts for time-dependence and growing damage was established using experimental data obtained from constant amplitude cyclic tests without rest periods. The description of modeling approach for the time-dependence and damage growth is presented in this section. The constitutive model was then extended to account for the microdamage healing.

Determination of Internal State Variables

Using the ISV formulation, the following form of constitutive relationship was proposed for asphaltic materials by Kim and Little (1990):

$$\sigma_{ij} = \sigma_{ij}(\varepsilon_{kl},\ t,\ T,\ \frac{\partial T}{\partial x_n},\ S_m) \tag{B.69}$$

where σ_{ij} = stresses in a body; $\varepsilon_{kl} = \varepsilon_{kl}(x_n, t)$ = strains in a body; t = time elapsed from the first application of loading; T = temperature; $\partial T/\partial x_n$ = spatial temperature gradients in a body; S_m = internal state variables; i,j,k,l,n = 1, 2, 3; and m = 1, 2, 3, ..., M. Assuming that the temperature is constant spatially and the pseudo strain accounts for all the viscoelastic hereditary effects of the material associated with a given strain history, equation (B.69) reduces to

$$\sigma_{ij} = \sigma_{ij}(\varepsilon^R_{kl},\ T,\ S_m) \tag{B.70}$$

In this study, only the uniaxial case with constant temperature is considered; therefore, equation (B.70) reduces to

$$\sigma = \sigma(\varepsilon^R,\ S_m) \tag{B.71}$$

In order to identify the basic structure of equation (B.71), the following uniaxial version of constitutive equations for linear elastic and linear viscoelastic bodies without and with damage is presented. They also show how models of different complexity may evolve from simpler ones.

Elastic Body without Damage:	$\sigma = E_R\,\varepsilon$	(B.72)
Elastic Body with Damage:	$\sigma = C(S_m)\,\varepsilon$	(B.73)
Viscoelastic Body without Damage:	$\sigma = E_R\,\varepsilon^R$	(B.74)
Viscoelastic Body with Damage:	$\sigma = C(S_m)\,\varepsilon^R$	(B.75)

where E_R is a constant and $C(S_m)$ indicates that C is a function of ISV's (or damage parameters) S_m. E_R in equation (B.72) is Young's modulus. The function $C(S_m)$ represents the changing *stiffness* of the material due to changes in microstructure of the material, e.g., growing damage or

healing. It is seen that equations (B.74) and (B.75) take the form of equations (B.72) and (B.73), respectively; i.e., a useful elastic-viscoelastic correspondence exists between the two sets of equations. This observation is supported by the correspondence principle described in a preceding section, and therefore, the viscoelastic behavior can be described by the elastic equations with physical variables replaced by corresponding pseudo variables. The form of equation (B.75) is also supported by the observations made earlier from monotonic loading data in Figure B.14 that, when the induced damage is negligible, the material behaves like a linear elastic material with the substitution of strain with pseudo strain and that the stiffness changes as damage grows.

Equation (B.75) is a more specific version of equation (B.71), and the constitutive modeling of asphalt concrete under cyclic loading reduces to determination of the explicit form of $C(S_m)$ in equation (B.75) using the ISV's that account for damage growth. In order to obtain necessary experimental data for this task, constant stress/strain amplitude cyclic tests without rest periods were performed. Two stress/strain levels high enough to induce some damage to the specimens were used in the tests.

Figures B.15(a) and B.15(b) show typical stress-strain hysteresis loops at different numbers of cycles in the controlled-strain and -stress modes, respectively. The same stresses in these figures were plotted against pseudo strains in Figure B.16(a) for the controlled-strain, figure B.16(b) for the controlled-stress mode. Unlike the negligible damage case in Figure B.12(b), the following three characteristics are noticeable in these figures due to the damage incurred in the specimens:

a. nonlinear behavior of the loading and unloading paths in each cycle,
b. change in the slope of each σ-ε^R cycle (i.e., reduction in the stiffness of the material) as cyclic loading continues, and
c. shift of the σ-ε^R loop from the origin as cyclic loading continues in the controlled-stress mode.

The first two characteristics of the σ-ε^R behavior, "a" and "b", are observed from both modes of loading, while the third characteristic, "c", is unique in the controlled-stress mode. In the following, more insights on these characteristics are discussed.

Hysteretic Behavior of Stress-Pseudo Strain Curve

As can be seen from the loading and unloading curves in Figure B.16(a), there are two different stresses associated with one ε^R value. On the loading path, the stress is a function of current ε^R only, while on the unloading path, the stress is a function of current ε^R and the largest ε^R during the ε^R history up to that time (ε_L^R). This observation suggests the use of $\varepsilon^R/\varepsilon_L^R$ in identifying whether the point of interest is on the loading path or on the unloading path (Kim and Little, 1990). That is, $\varepsilon^R/\varepsilon_L^R = 1$ during the loading path, and $\varepsilon^R/\varepsilon_L^R < 1$ during the unloading path.

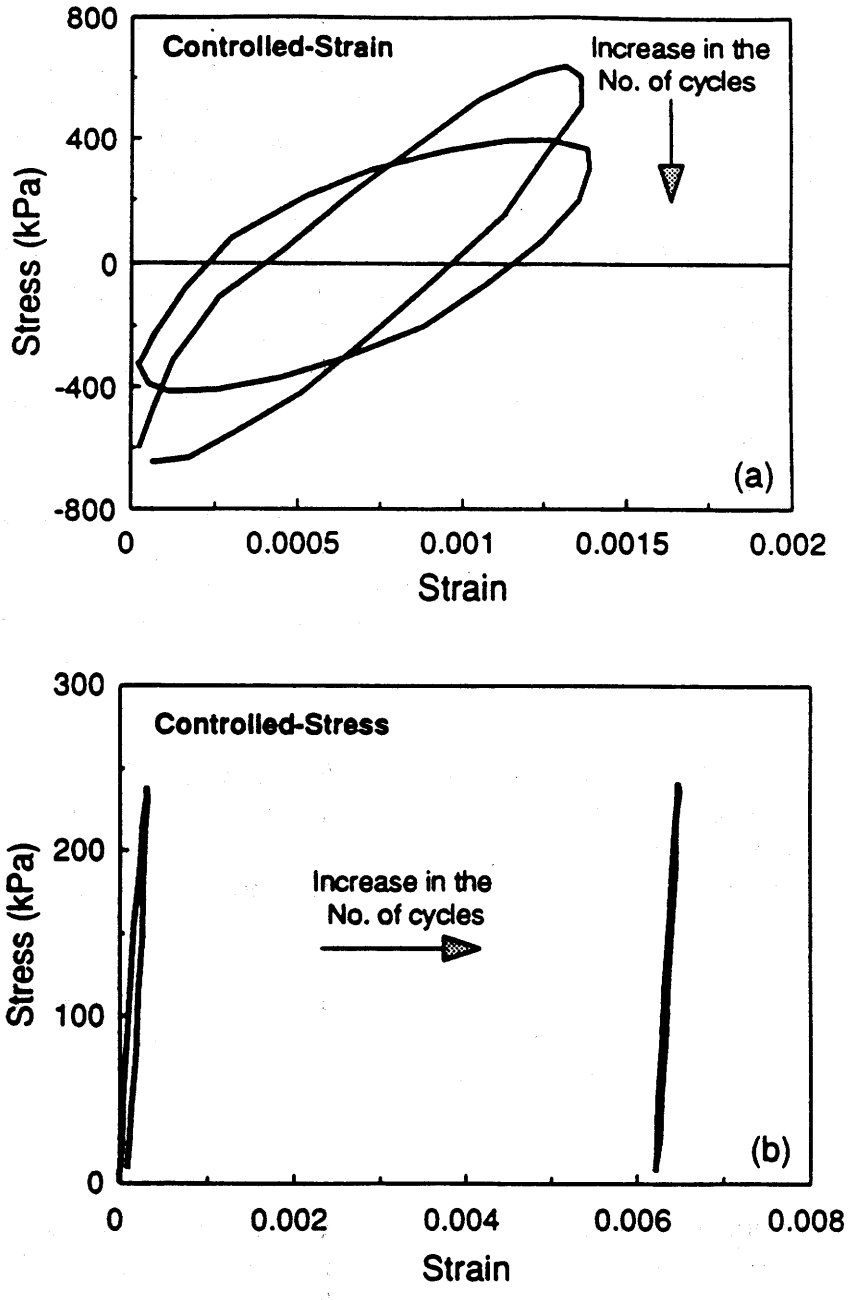

Figure B. 15 Stress-strain Behavior With Damage Growth Under Cyclic Loading: (a) Controlled-strain Mode; (b) Controlled-stress Mode.

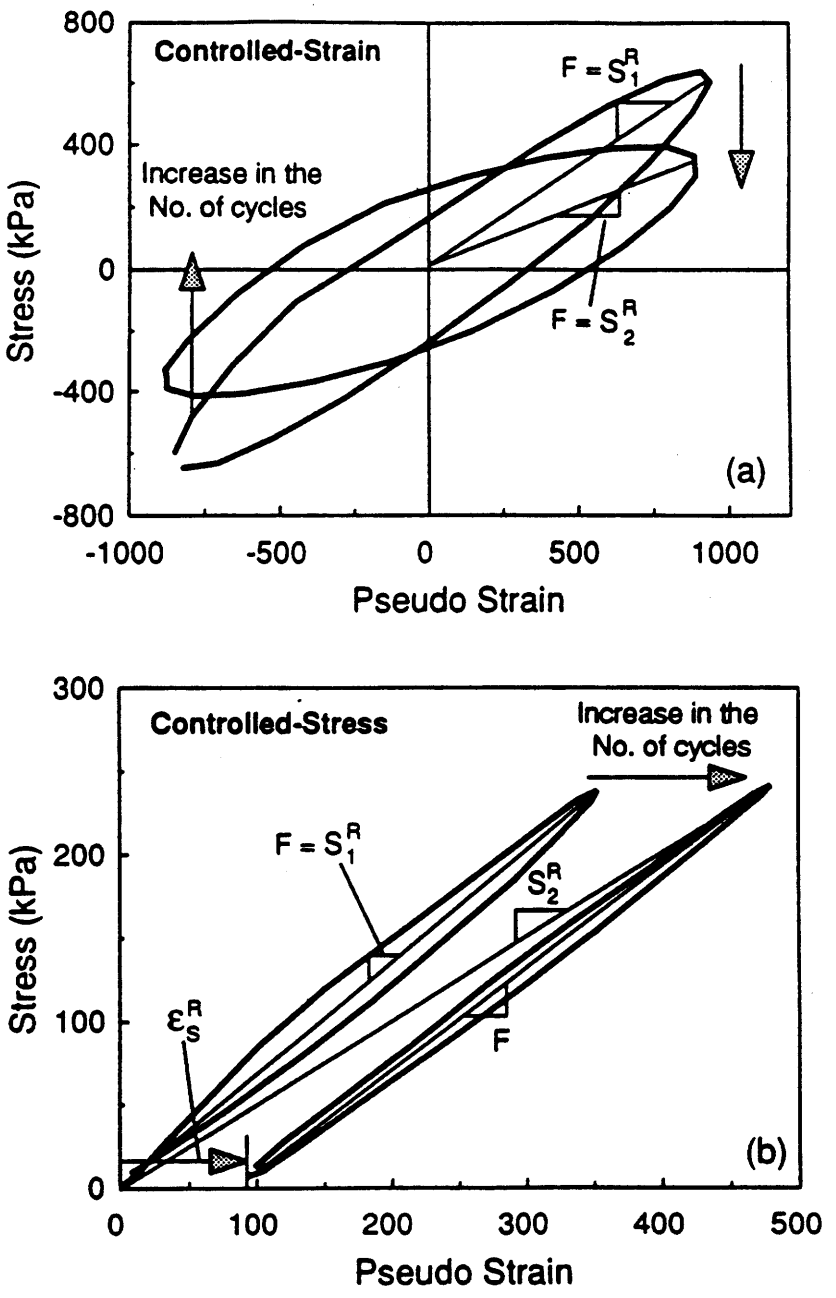

Figure B.16 Stress-pseudo Strain Behavior and Pseudo Stiffness Changes In: (a) Controlled-strain Mode; (b) COntrolled-stress Mode.

It was found from the experimental data that the size of each stress-pseudo strain hysteresis loop was dependent upon the stress amplitude incurred in a specimen. That is, the larger the stress amplitude, the bigger the hysteresis loop. Since $\sigma \sim |\varepsilon^R|^N$, the amplitude of pseudo strain, denoted by ε_0^R, is selected as another ISV to represent the effect of the stress amplitude on the hysteresis loops.

The above observations suggest the use of two ISV's, $\varepsilon^R/\varepsilon_L^R$ and ε_0^R, for describing the hysteretic stress pseudo-strain behavior undergoing damage. Thus, the constitutive equation (B.75) becomes:

$$\sigma = \varepsilon^R C(\frac{\varepsilon^R}{\varepsilon_L^R}, \varepsilon_0^R, S_m) \tag{B.76}$$

where $m = 3, 4, ..., M$.

Secant Pseudo Stiffness

As can be seen in Figures B.16(a) and B.16(b), the slope of each stress pseudo-strain loop decreases as cyclic loading continues due to fatigue damage. To represent the change in the slope, including the effect of the shift in the controlled-stress mode, *secant pseudo stiffness* S^R (hereinafter called pseudo stiffness for simplicity), was defined as

$$S^R = \frac{\sigma_m}{\varepsilon_m^R} \tag{B.77}$$

where ε_m^R = peak pseudo strain in each stress pseudo-strain cycle and
σ_m = stress corresponding to ε_m^R.

Since S^R is determined from stress and pseudo strain values, instead of physical strain, the change in S^R represents damage growth separately from the time-dependence. This allows a simple function of S^R to describe mechanisms under complicated loading histories.

Although $\varepsilon^R/\varepsilon_L^R$ and ε_0^R are sufficient to model the hysteretic behavior in each cycle, another ISV is needed to model the change in the slope of each cycle as cyclic loading continues. Knowing the reduction in this slope is related to the fatigue crack growth, the damage parameter S_1 is employed in the constitutive model as another ISV. Thus, equation (B.77) becomes

$$\sigma = \varepsilon^R C(S_1, \frac{\varepsilon^R}{\varepsilon_L^R}, \varepsilon_0^R, S_m) \tag{B.78}$$

where $m = 4, 5, ..., M$.

Permanent Pseudo Strain

A major difference in the characteristics of the stress pseudo-strain behavior between the controlled-strain and -stress modes is that the hysteresis loop shifts away from the origin in the controlled-stress mode as cyclic loading continues (Figure B.16(b)). This shift is called *permanent pseudo strain* and denoted by ε_S^R.

To understand the characteristics of ε_S^R, it is helpful to study the analytical solution of pseudo strain for the strain history under the controlled-stress mode given in equations (B.67) and (B.68). Since the first term B_0 and the last term in the right-hand side of equation (B.67) have little effect on the average strain in each cycle, $\varepsilon_1(t)$ is simplified to $B_1 t^{\alpha}$. Also, a constant strain amplitude ε_0 is assumed instead of $\varepsilon_0(t)$ in equation (B.68) for the simplicity of analysis. Using the first derivatives of these strain functions and the relaxation modulus in the form of pure power law (i.e., $E(t)=E_1 t^{-m}$), the following pseudo strain can be obtained:

$$\varepsilon^R(t) = P_0 t^{(\alpha-m)} + P_1 \sin(\omega t + \theta + \phi) \tag{B.79}$$

where

$$P_0 = \frac{B_1 E_1 \Gamma(1-m)\Gamma(1+m)}{\Gamma(\alpha-m+1)} \tag{B.80}$$

$$P_1 = \varepsilon_0 |E^*| = \varepsilon_0 E_1 \Gamma(1-m)\omega^m \tag{B.81}$$

Γ is Gamma function defined as

$$\Gamma(m) \equiv \int_0^{\infty} t^{m-1} e^{-t}\, dt \tag{B.82}$$

The value of ε_S^R can be obtained by subtracting the amplitude of pseudo strain from the average pseudo strain of each cycle (i.e., $P_0 t^{(\alpha-m)} - P_1$). For a linear viscoelastic case, $\alpha \approx m$ and $P_0=P_1$ because the pseudo strain and stress are equivalent (i.e., $\sigma = \sigma_0 + \sigma_0 \sin(\omega t+\theta+\phi)$) based on the definition of pseudo strain (B.13) when $E_R = 1$. Thus, $\varepsilon_S^R = 0$, as seen in figure B.12(b). When the load level is high enough to induce some damage to a specimen, $\alpha > m$ resulting $\varepsilon_S^R > 0$, as shown in Figure B.16(b).

Considering the above observations and increasing deformation in the controlled-stress test in tension, it can be said that the presence of ε_S^R is mainly due to the permanent deformation accumulated in the specimen during the tensile fatigue test. Therefore, it is proposed that ε_S^R be used as the last ISV accounting for the difference between the controlled-strain and -stress modes in the constitutive modeling.

Viscoelastic Model With Growing Damage

Using the elastic-viscoelastic correspondence principle (Schapery, 1984) and a time-dependent damage parameter S_p (Schapery, 1981), Lee and Kim (1997) proposed a constitutive model that describes the mechanical behavior of asphalt concrete under uniaxial tensile cyclic loading without rest periods as follows:

$$\sigma = I(\varepsilon_e^R)[F + G] \tag{B.83}$$

where, $\varepsilon_e^R = \varepsilon^R - \varepsilon_S^R$,

$\varepsilon_{me}^R = \varepsilon_m^R - \varepsilon_S^R$,

F = damage function, and

G = hysteresis function.

The function F represents the change in the slope of each σ-ε^R loop shown in Figure B.16, while the hysteresis function G represents the difference between loading and unloading paths in each cycle. The effective pseudo strain, ε_e^R, was used to account for the permanent pseudo strain ε_S^R accumulated in the controlled-stress mode shown in Figure B.16(b). The details on the mathematical expressions of the functions F and G can be found in Lee and Kim (1997). In the validation study, this model successfully predicted the mechanical behavior of asphalt concrete all the way up to failure under both controlled-strain and -stress modes.

Although the damage parameter S_p successfully described the damage growth in asphalt concrete, it may not be directly used to describe the microdamage healing because this damage parameter is developed based on the generalization of the microcrack growth law. Since the purpose of this research is developing a constitutive model that can account for both the growing damage and microdamage healing, the work potential theory seemed to be more appropriate for this purpose because of its generality (Lee, 1996).

In Lee and Kim's study, it was observed that two different material functions, $F(S_p)$ and $G(\varepsilon^R/\varepsilon_L^R, \varepsilon_0^R)$, were required to model the mechanical behavior of asphalt concrete. In addition to these functions, the so-called mode factor $(1+\varepsilon_S^R/\varepsilon_{me}^R)$ and the effective pseudo strain ε_e^R were employed to account for the effects of different modes of loading. Our experimental study showed that the functions F and G are independent of each other. Based on these observations, it is assumed that two material functions, $C_1(S_1)$ and $C_2(\varepsilon^R/\varepsilon_L^R, \varepsilon_0^R)$ say, are necessary to model the constitutive behavior of asphalt concrete. That is, S_1 is an ISV that describes the change in S^R due

to fatigue damage growth, and the ISV's, $\varepsilon^R/\varepsilon_L{}^R$ and $\varepsilon_0{}^R$, describe the inelastic behavior of loading and unloading paths.

In the following, a uniaxial viscoelastic model with growing damage is proposed based on the above observations for the controlled-strain mode. This model is then extended to account for the controlled-stress mode using the mode factor and effective pseudo strain described earlier.

The pseudo-strain energy density function $W^R = W^R(\varepsilon^R, S_m)$ with three ISV's is proposed as follows:

$$W^R = \frac{I}{2}C_1(S_1)(\varepsilon^R)^2 + \frac{I}{2}C_2(\frac{\varepsilon^R}{\varepsilon_L^R}, \varepsilon_0^R)(\varepsilon^R)^2 \tag{B.84}$$

where I is the initial pseudo stiffness used to account for inherent sample-to-sample variability. From equations (B.26) and (B.84), we can obtain the following stress-strain relationship:

$$\sigma = \frac{\partial W^R}{\partial \varepsilon^R} = I[C_1(S_1) + C_2(\frac{\varepsilon^R}{\varepsilon_L^R}, \varepsilon_0^R)]\,\varepsilon^R \tag{B.85}$$

To take the effects of mode of loading into consideration, first ε^R in equation (B.84) will be replaced with $\varepsilon_e{}^R$ (i.e., ε^R-$\varepsilon_S{}^R$), and then the mode factor $(1+\varepsilon_S{}^R/\varepsilon_{me}{}^R)$ will be included in equation (B.84). Now, equation (B.84) becomes

$$W^R = \frac{IM}{2}C_1(S_1)(\varepsilon_e^R)^2 + \frac{I}{2}C_2(\frac{\varepsilon^R}{\varepsilon_L^R}, \varepsilon_0^R)(\varepsilon_e^R)^2 \tag{B.86}$$

where $M = 1+\varepsilon_S{}^R/\varepsilon_{me}{}^R$ and $\varepsilon_e{}^R = \varepsilon^R - \varepsilon_S{}^R$. Then, the stress-strain relationship is

$$\sigma = I[MC_1(S_1) + C_2(\frac{\varepsilon^R}{\varepsilon_L^R}, \varepsilon_0^R)]\,\varepsilon_e^R \tag{B.87}$$

S_1 in equation (B.87) is the only undetermined ISV, and can be obtained from the time-dependent damage evolution law (B.29). For the first ISV S_1, equation (B.29) can be rewritten as follows without bar (-) notation for notational simplicity :

$$\dot{S}_1 = (-\frac{\partial W^R}{\partial S_1})^{\alpha_1} \tag{B.88}$$

Equations (B.86)-(B.88) constitute a model for the uniaxial stress-strain behavior of asphalt concrete with growing damage.

In the following subsection, general characterization procedures for obtaining the material function C_1 will be discussed. For the characterization purposes, it is useful to reduce the constitutive equations (B.86) and (B.87) to simpler forms. Since C_1 represents the change in S^R, it is constant within a σ-ε^R cycle. So, only the values of σ_m and ε_m^R in each cycle are needed to characterize the function C_1. When ε^R becomes ε_m^R, $G = 0$ because $C_1=(\sigma_m/I\ \varepsilon_m^R)$. Observing that $M\varepsilon_{me}^R = \varepsilon_m^R$, we can obtain the following forms of reduced constitutive equations (B.89) and (B.90) from equations (B.86) and (B.87).

$$W_m^R = \frac{I}{2} C_1(S_1)\, \varepsilon_m^R\, \varepsilon_{me}^R \tag{B.89}$$

and

$$\sigma_m = I C_1(S_1)\, \varepsilon_m^R \tag{B.90}$$

where W_m^R = pseudo strain energy density function when $\varepsilon^R = \varepsilon_m^R$,
ε_m^R = peak pseudo strain in each stress pseudo-strain cycle,
ε_{me}^R = $\varepsilon_m^R - \varepsilon_S^R$, and
σ_m = stress corresponding to ε_m^R.

W^R in the evolution law (B.88) is replaced with W_m^R as follows:

$$\dot{S}_1 = \left(-\frac{\partial W_m^R}{\partial S_1}\right)^{\alpha_1} \tag{B.91}$$

The reduced constitutive equations (B.89)-(B.91) describe the change in the slope of each σ-ε^R loop due to fatigue damage, and allow us to characterize the function C_1 more easily without considering the function C_2.

General Characterization Procedures

The material function $C_1(S_1)$ in equation (B.90) can be found by using a set of experimental data and the damage evolution law. Equation (B.90) together with the measured stresses gives C_1 that depends on the pseudo strains. In order to find their dependence on S_1, we need to first obtain the values of S_1 corresponding to the strain input by solving the evolution law. However, the

evolution law (B.91) is not convenient for finding S_1 because the equation itself requires a prior knowledge of $C_1(S_1)$ before the equations can be solved for S_1. There are several ways to overcome this problem. In this study, the following two approaches were considered. For notational simplicity, C_1, S_1, σ_m, ε_m^R, and W_m^R, will be denoted by C, S, σ, ε^R, and W^R respectively, in this subsection only.

Approach 1

This approach was proposed by Park et al. (1996). First, they recognized that the approximate form of the damage evolution law in equation (B.33) could be transformed further to a simple form, which does not contain the variable S, through a change-of-variable technique as follows:

$$-\frac{\partial W^R}{\partial \hat{S}} = t^{-\frac{1}{\alpha}} \tag{B.92}$$

where

$$\hat{S} = \frac{1}{(1+1/\alpha)} S^{(1+1/\alpha)} \tag{B.93}$$

Rewriting equations (B.89) and (B.90) in terms of the transformed damage variable $\hat{S}$, we obtain, respectively,

$$W^R = \frac{I}{2} C(\hat{S}) (\varepsilon^R)^2 \tag{B.94}$$

and

$$\sigma = I C(\hat{S}) \varepsilon^R \tag{B.95}$$

From equations (B.92) and (B.94),

$$-\frac{I}{2} \frac{dC(\hat{S})}{d\hat{S}} (\varepsilon^R)^2 = t^{-\frac{1}{\alpha}} \tag{B.96}$$

First, the pseudo stiffness C is obtained from equation (B.95) using the measured stresses and pseudo strains. The transformed variable $\hat{S}$ is then obtained from the following numerical

scheme:

$$\hat{S}(\varepsilon_{i+1}^R) = \hat{S}(\varepsilon_i^R) + \Delta\hat{S} \tag{B.97}$$

where

$$\Delta\hat{S} = \frac{C(\varepsilon_{i+1}^R) - C(\varepsilon_i^R)}{C'(\varepsilon_i^R)} \tag{B.98}$$

Also, ε_i^R (i=1,2,...,N) denotes discrete pseudo strain levels, C' = dC/d$\hat{S}$, and $\hat{S}(0) = 0$. Since we already obtained the values of C, as explained before, we can also obtain C' values from equation (B.96) with an appropriately assumed value of α. For the initial value of α, α=(1+1/m) is assumed. Now, the values of $\hat{S}$ can be obtained from equations (B.97) and (B.98). Cross-plotting the C values against the $\hat{S}$ values, we can obtain the function C($\hat{S}$). Finally, the function C(S) can be obtained from C($\hat{S}$) by replacing the transformed variable $\hat{S}$ with the original variable S according to equation (B.93). The constant α was carried over to the original model without being changed.

Recall that the evolution laws (B.91) and (B.92) are not exactly equivalent because equation (B.92) was obtained from equation (B.91) based on the assumption that $\alpha >> 1$. Therefore, the function C(S) and the constant α determined so far are approximate to the degree of accuracy involved in the derivation of (B.92) from (B.91). The *true* C(S) and α can be obtained by improving those obtained from equation (B.92) through a method of *successive approximations*. Namely, the tentative C(S) and α can be substituted into equation (B.89) and then equation (B.91), and S for each given ε^R is obtained by summing the incremental values of S over time with an initial condition $S|_{t=0} = 0$. Since we know C values for different ε^R values from equation (B.90), by plotting C against the new S for all ε^R values, we can obtain the refined function C(S). The same steps may be repeated until the new C(S) and α are not practically different from their preceding versions. Detailed steps involved in this procedure can be found in Park et al. (1996).

Approach 2

An efficient way of characterizing the function C(S) has been proposed by Lee (1996). This approach was motivated by observing the fact that S in the right-hand side of the evolution law (B.91) can be eliminated using the following chain rule:

$$\frac{dC}{dS} = \frac{dC}{dt}\frac{dt}{dS} \tag{B.99}$$

From equations (B.89) and (B.91),

$$\frac{dS}{dt} = [\,-\frac{I}{2}\frac{dC}{dS}(\varepsilon^R)^2\,]^{\alpha} \tag{B.100}$$

Substituting equation (B.99) into equation (B.100) yields

$$\frac{dS}{dt} = [\,-\frac{I}{2}\frac{dC}{dt}(\varepsilon^R)^2\,]^{\frac{\alpha}{(1+\alpha)}} \tag{B.101}$$

Integrating equation (B.101) with an initial condition $S|_{t=0} = 0$ results in

$$S = \int_0^t [\,-\frac{I}{2}\frac{dC}{dt}(\varepsilon^R)^2\,]^{\frac{\alpha}{(1+\alpha)}}\,dt \tag{B.102}$$

The significance of equation (B.102) is that we can obtain the S values directly from the experimental data without employing the successive approximations described in Approach 1. The function C and ε^R are dependent upon time t because $C=C(S(\varepsilon^R))$ and $\varepsilon^R=\varepsilon^R(\varepsilon, t, E(t))$. Thus, S in equation (B.102) may be obtained from the following numerical scheme:

$$S \cong \sum_{i=1}^{N} [\frac{1}{2}(\varepsilon_i^R)^2 (C_{i-1}-C_i)\,]^{\frac{\alpha}{(1+\alpha)}} (t_i - t_{i-1})^{\frac{1}{(1+\alpha)}} \tag{B.103}$$

where ε_i^R (i=1,2,...,N) denotes discrete pseudo strain values. When t = 0, $C = \varepsilon^R = 0$. Thus S = 0. The pseudo stiffness C_i corresponding to the current time t_i can be obtained from equation (B.90) using the measured stress σ_i and pseudo strain ε_i^R. Now, we can obtain S from equation (B.103) with an appropriately assumed value of α, such that $\alpha = (1+1/m)$. Finally, the function C(S) can be obtained by cross-plotting the measured C values against the S values.

The validity of the assumed value of α can be examined by cross-plotting the measured C against S obtained from equation (B.103). In general, at least two data sets that have different stress/strain levels are required in this process. If α is a true material constant, the two different load-level data should fall on the same curve. When there exists a discrepancy between the two data sets, the value of α may be adjusted through a trial-and-error process until a good match is achieved between the two data sets. In the remaining analysis, this Approach 2 was employed in characterizing the material functions and constants because of its simplicity.

Characterization of Material Function C_1 and Constant α_1

In order to determine the function C_1, the values of S_1 were first calculated from equation

(B.103) with the assumption that $\alpha_1 = (1+1/m)$. Typical m values obtained from the creep tests were 0.628 and 0.578 for the AAD and AAM mixtures resulting from the α_1 values of 2.595 and 2.73, respectively. The values of C_1 were calculated from equation (B.90) using the measured stresses and the pseudo strains calculated. The change in C_1 for AAD and AAM mixtures were plotted against the S_1 values in Figures B.17(a) and B.17(b), respectively. As can be seen from these figures, S_1 successfully accounts for the strain-level dependence of the materials providing the validity of the initial values of α_1. Therefore, $\alpha=(1+1/m)$ was used for the initial value of α_i in the remaining analysis. The regression analysis on the data shown in Figure B.17 resulted in the following equation for the function C_1:

$$C_1(S_1) = C_{10} - C_{11}'(S_1)^{C_{12}} \qquad \text{(B.104)}$$

The regression coefficients in equation (B.104) for the two mixtures are provided in Table B.8.

Table B.8 Model Coefficients for Functions C_1, C_2, and C_3

Function C_1	C_{10}	C_{11}'	C_{11}	C_{12}
AAD	0.99	0.00647	0.489	0.44
AAM	1.10	0.0764	0.530	0.20
Function C_2	**C_{20}**	**C_{21}**		**C_{22}**
AAD	-0.375	0.0941		0.20
AAM	0.0015	0.0004		0.62
Function C_3	**C_{30}**	**C_{31}**		**C_{32}**
AAD	1.01	0.0019		0.55
AAM	1.01	0.0114		0.30

Similarly, the values of C_1 and S_1 were determined using the controlled-stress cyclic test data and plotted in Figure B.18. Unlike the controlled-strain case, S_1 was not able to eliminate the stress level dependency. Thus, the values of α_1 were adjusted employing the trial-and-error procedure to achieve a good match between the two stress level data. The final values of α_1 are 1.65 and 1.6 for AAD and AAM mixtures, respectively, and are closer to $\alpha_1=1/m$ (i.e., 1.59 and 1.73 for AAD and AAM mixtures, respectively). This implies that $\alpha=1/m$ is a better assumption for the initial value of α_1 in the controlled-stress mode. A similar result has been observed in the S_p approach in Lee and Kim (1997).

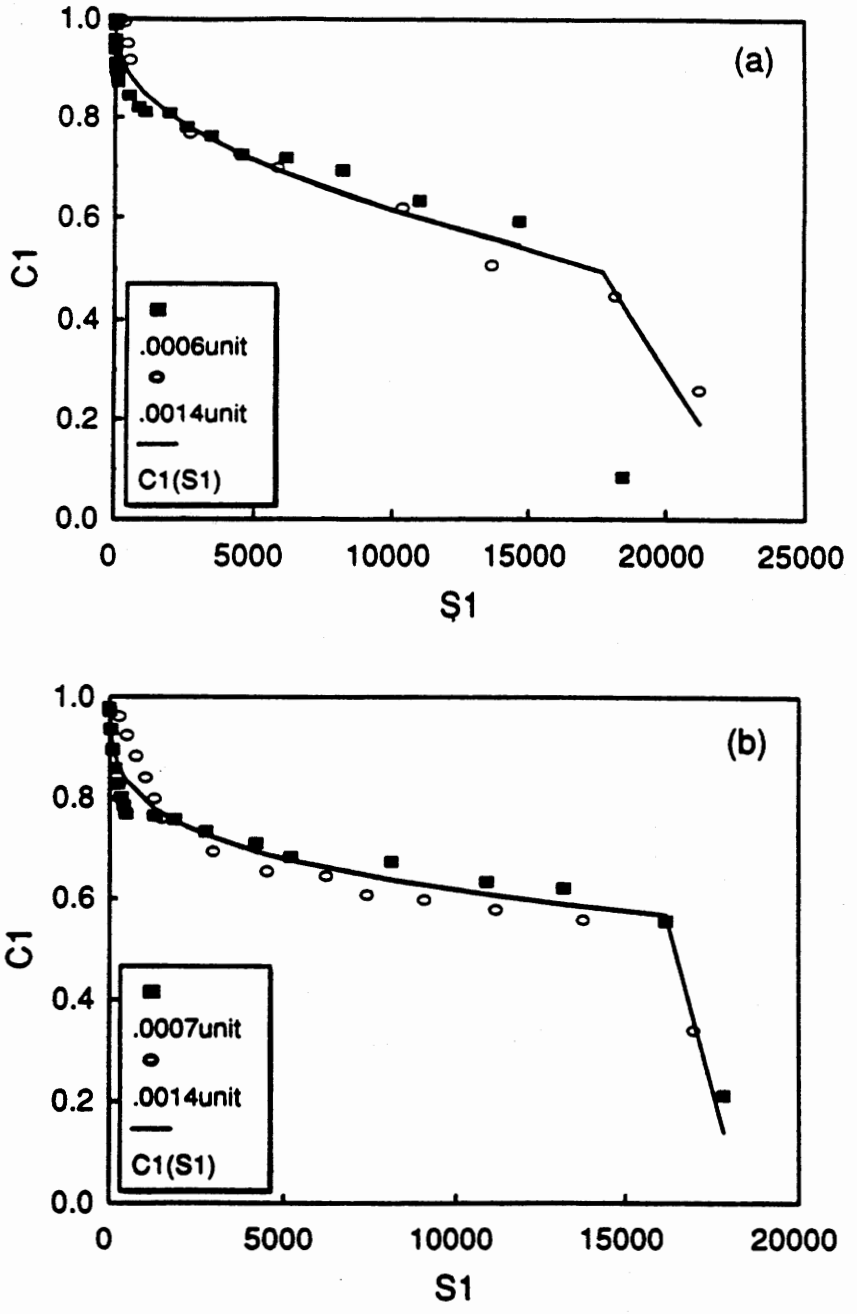

Figure B.17 Pseudo Stiffness S^R Versus S_1 Under Controlled-strain Mode: (a) AAD Mixture; (b) AAM Mixture.

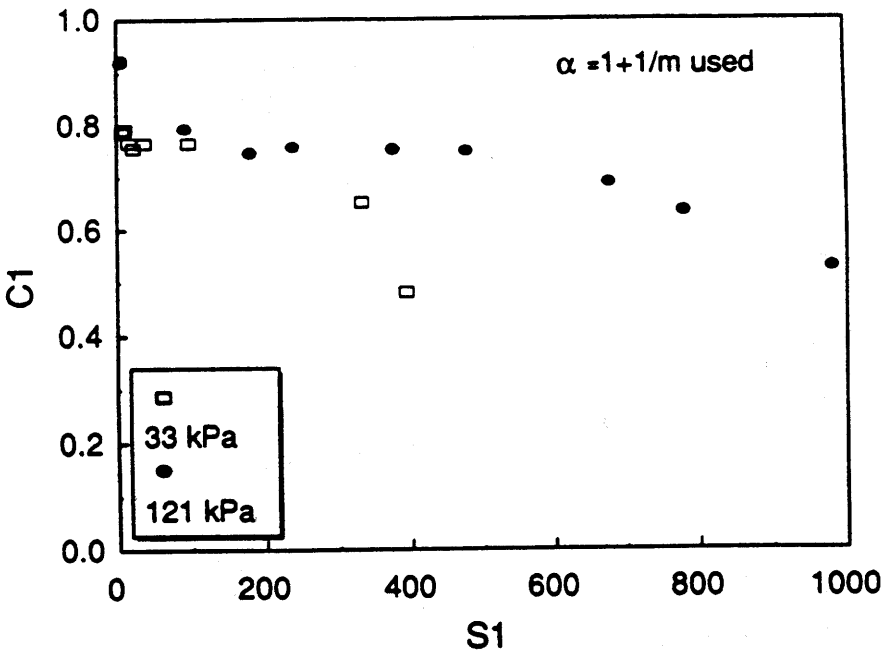

Figure B.18 Pseudo Stiffness S^R Versus S_1 Obtained Using $\alpha_1 = 2(1+2/m)$ Under Controlled-stress Mode.

To study the mode of loading effect on the C_1-S_1 behavior, both modes of loading data are presented in Figure B.19. As can be seen in this figure, the value of S_1 of the controlled-strain mode is larger than that of the controlled-stress mode for a certain value of C_1. Therefore, S_1 was normalized by using a value of S_1 at failure, denoted S_{1f}. To determine the value of S_{1f}, 50 percent reduction in the *initial pseudo stiffness* was employed for a failure criterion. In the controlled-strain mode, the S_{1f} values were 17,720 and 16,080 for AAD and AAM mixtures, respectively, and in the controlled-stress mode, 1,100 and 3,500 for AAD and AAM mixtures, respectively. A similar approach has been employed in the S_p approach in Lee and Kim (1997).

Normalized ISV S_{1n} was defined as follows:

$$S_{1n} = \frac{S_1}{S_{1f}} \tag{B.105}$$

The C_1 data in Figures B.19(a) and B.19(b) are plotted against S_{1n} in Figures B.20(a) and B.20(b), respectively. The difference in the C_1-S_1 behavior between controlled-strain and -stress modes has disappeared in these figures. The S_1 in equation (B.104) is now replaced with S_{1n}:

$$C_1(S_{1n}) = C_{10} - C_{11}(S_{1n})^{C_{12}} \tag{B.106}$$

where $C_{11} = C_{11}' (S_{1f})^{C12}$ is provided in Table B.8. The damage function $C_1(S_1)$ in the constitutive model (B.87) is replaced with equation (B.106).

Characterization of Material Function C_2

To find the explicit form of function C_2, the data obtained from the controlled-strain cyclic tests was used. For notational simplicity, C_2 is denoted by G hereinafter. The values of F were subtracted from $\sigma/(I\varepsilon^R)$ (hereinafter, called back-calculated G) and then plotted against $\varepsilon^R/\varepsilon_L{}^R$. In order to investigate the effects of fatigue damage, the data at different stages of fatigue damage, from the beginning to near failure, were used. As shown in Figure B.21, a strong power relationship was observed between the back-calculated G and $\varepsilon^R/\varepsilon_L{}^R$. In this figure, the value of $\varepsilon^R/\varepsilon_L{}^R$ increases during loading (Loading I for the negative values of $\varepsilon^R/\varepsilon_L{}^R$ and Loading II for the positive values of $\varepsilon^R/\varepsilon_L{}^R$) while it decreases during unloading (Unloading I for the positive values of $\varepsilon^R/\varepsilon_L{}^R$ and Unloading II for the negative values of $\varepsilon^R/\varepsilon_L{}^R$). The study of these data produced the following form of the function G:

$$G = G_0 + G_1 \left| \frac{\varepsilon^R}{\varepsilon_L^R} \right|^{G_2(\varepsilon_0^R)} \tag{B.107}$$

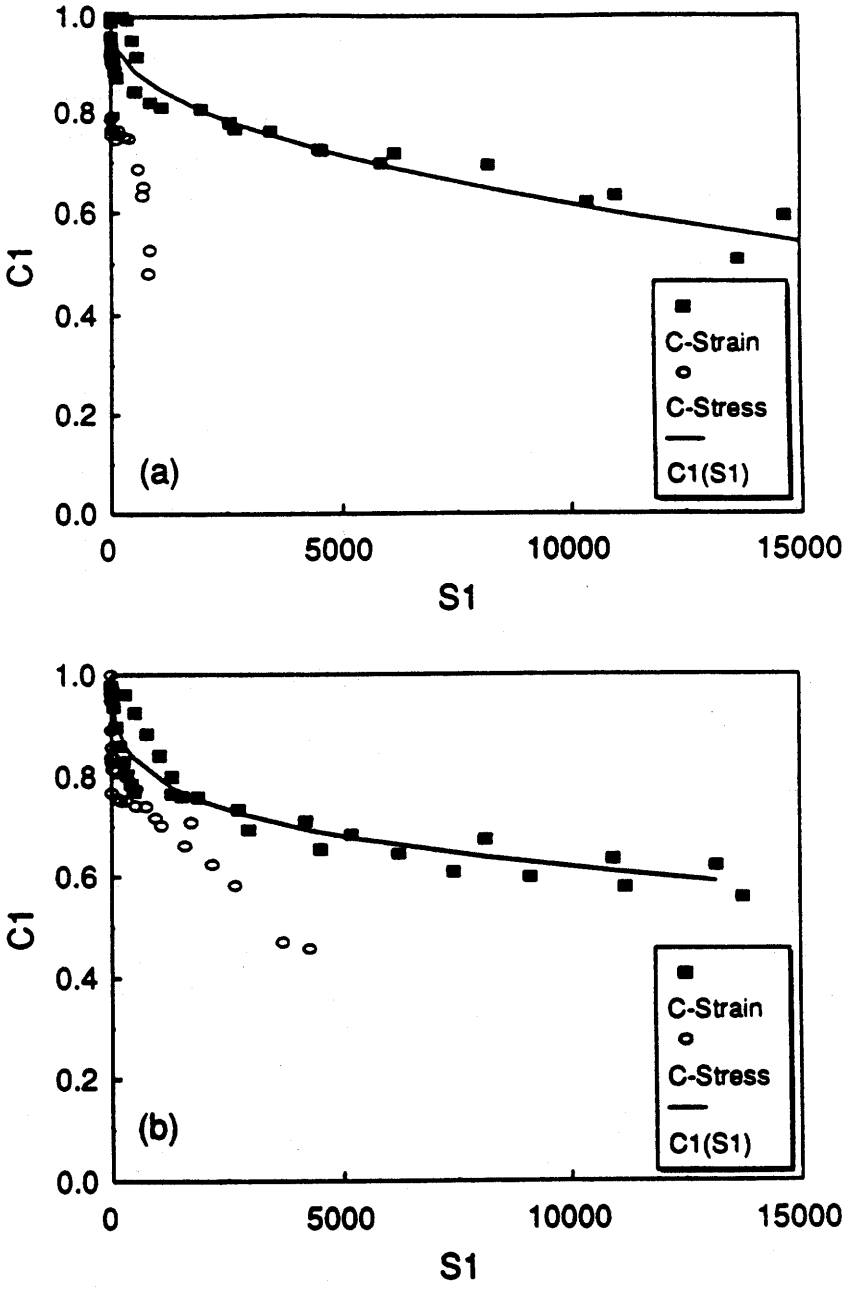

Figure B. 19 Pseudo Stiffness S^R Versus S_1 Under Both Modes of Loading: (a) AAD Mixture; (b) AAM Mixture.

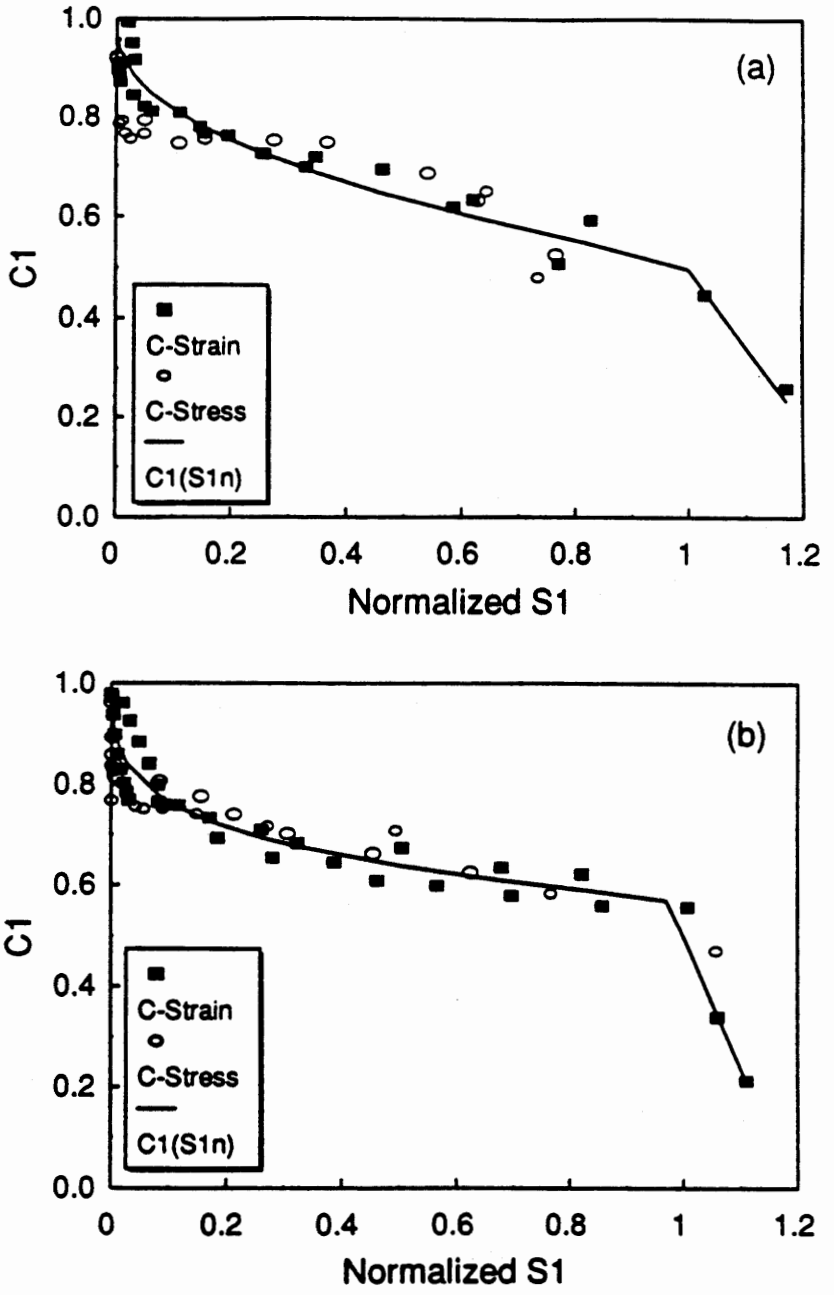

Figure B.20 Pseudo Stiffness S^R Versus S_{1n} Under Both Modes of Loading: (a) AAD Mixture, (b) AAM Mixture.

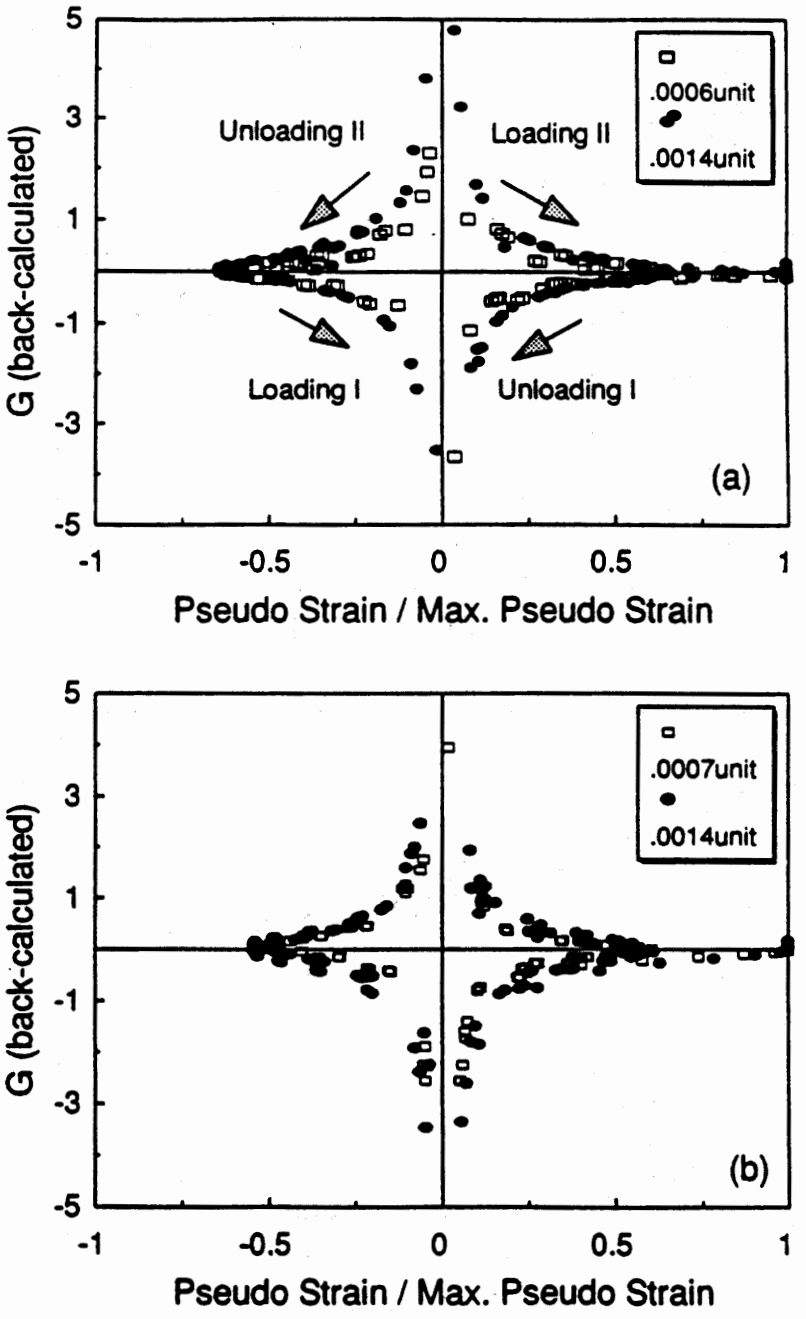

Figure B.21 Back-calculated Function G Versus ϵ^R/ϵ_L^R: (a) AAD Mixture;; (b) AAM Mixture.

The regression coefficients, G_0 and G_1, are summarized in Table B.9 for the two mixtures.

Table B.9 Coefficients in Equation (B.107)

Mix	Zone	G_0	G_1	G_{2R}	R^2
AAD	Loading I	0.1917	-0.1765	-1.00	0.889
	Loading II	-0.0933	0.0912	-1.30	0.949
	Unloading I	0.1573	-0.1653	-1.00	0.947
	Unloading II	-0.6945	0.5713	-0.63	0.846
AAM	Loading I	0.5684	-0.3789	-0.75	0.917
	Loading II	-0.3025	0.2526	-0.80	0.973
	Unloading I	0.0008	-0.0760	-1.20	0.976
	Unloading II	-0.3848	0.2481	-0.90	0.828

Since the size of the stress-pseudo strain hysteresis loop is dependent upon the amplitudes of pseudo strain incurred in the specimens, the exponent G_2 in equation (B.107) is a function of ε_0^R instead of a constant value.

All the values of G_2 at different strain amplitudes were obtained from regression analysis on the experimental data. Since there were four values of G_2 depending on the loading zone for one strain-amplitude data, they were normalized through division by a reference value of G_2, denoted by G_{2R}, for each loading zone. The values of G_2 at the strain amplitude of 0.0014 units for both mixtures in Table B.9 were selected as the G_{2R} values. The normalized G_2 values were then plotted against ε_0^R in Figures B.22(a) and B.22(b) for AAD and AAM mixtures, respectively. As shown in these figures, it was desirable to have more data near the origin to obtain regression curves because only two strain-amplitude data were available for each mixture. As discussed earlier, there was no stress pseudo-strain hysteresis loop developed (i.e., $G_2 = 0$) when the damage was negligible (i.e., in a linear viscoelastic range). Therefore, from the study of monotonic loading data, the ε_0^R value of 200 was assumed for both mixtures as an upper limit of this linear viscoelastic range. The regression analysis on the data shown in the figure resulted in the following form:

$$G_2(\varepsilon_0^R) = G_{2R}[\beta_0 + \frac{\beta_1}{\varepsilon_0^R}] \qquad \text{(B.108)}$$

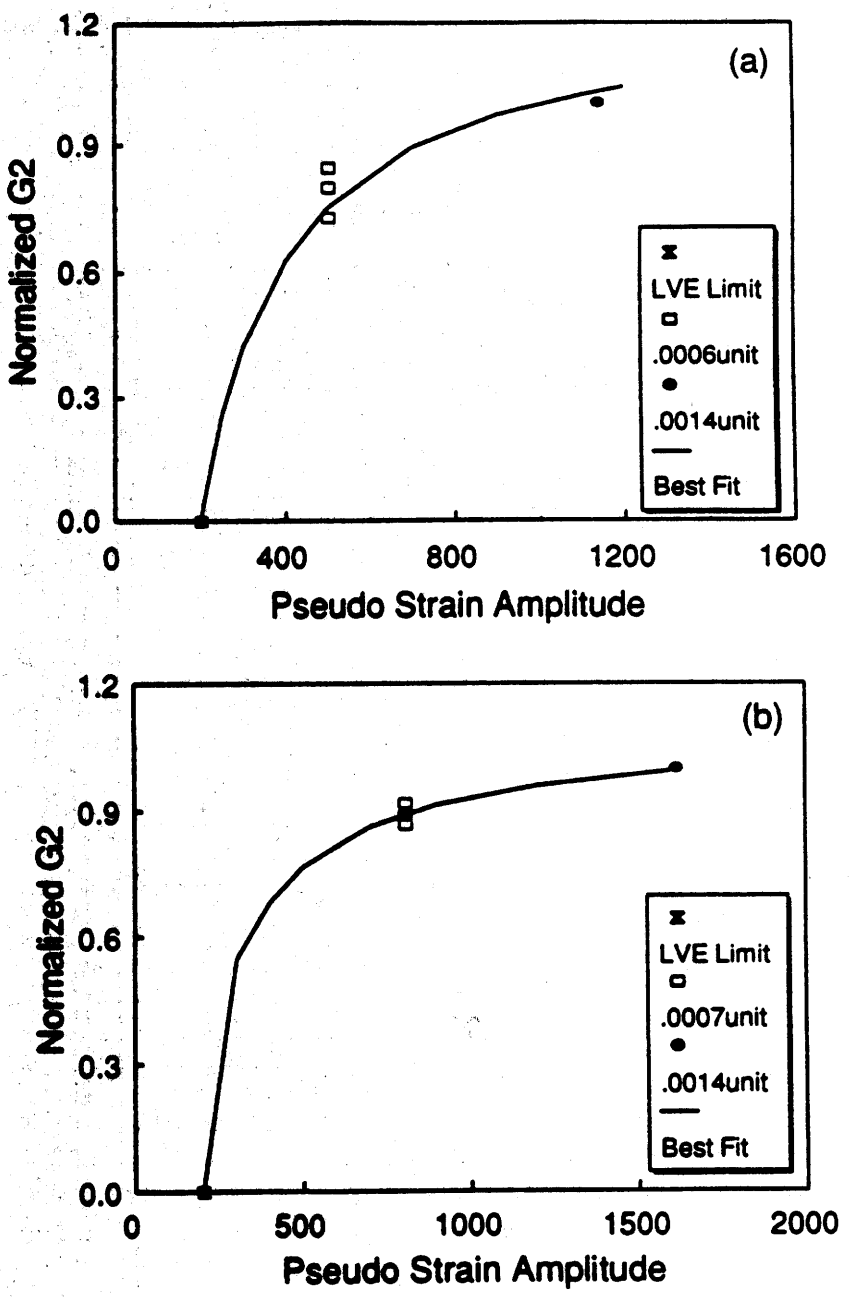

Figure B.22 Normalized G_2 Versus ϵ_0^R: (a) AAD Mixture; (b) AAM Mixture.

The regression coefficients in equation (B.108) are provided in Table B.10 for the two mixtures.

Table B.10 Coefficients in Equation (B.108)

Mixture	β_0	β_1	Boundary Condition
AAD	0.0	0.0	$\varepsilon^R_L \le 200$
	1.246	-247.066	$\varepsilon^R_L > 200$
AAM	0.0	0.0	$\varepsilon^R_L \le 200$
	1.155	-230.606	$\varepsilon^R_L > 200$

Table B.11 Viscoelastic Constitutive Model With Growing Damage

$$\sigma = I[F + G]\,\varepsilon_e^R \qquad \text{(B.109)}$$

where,

$$F = \left(1 + \frac{\varepsilon_S^R}{\varepsilon_{me}^R}\right)[C_{10} - C_{11}(S_{1n})^{C_{12}}]$$

$$G = G_0 + G_1 \left|\frac{\varepsilon^R}{\varepsilon_L^R}\right|^{G_2(\varepsilon_0^R)}$$

$$G_2(\varepsilon_0^R) = G_{2R}\left[\beta_0 + \frac{\beta_1}{\varepsilon_0^R}\right]$$

$$\varepsilon_e^R = \varepsilon^R - \varepsilon_S^R$$

$$\varepsilon_{me}^R = \varepsilon_m^R - \varepsilon_S^R$$

The final form of the constitutive model with growing damage is summarized in Table B.11. It is noted here that M = 1 and $\varepsilon_e^R = \varepsilon^R$ for the controlled-strain case because $\varepsilon_S^R = 0$. Also, for monotonic loading, the constitutive equation (B.109) can be simplified as follows:

$$\sigma = I C_1(S_1)\,(\varepsilon^R) \qquad \text{(B.110)}$$

because $\varepsilon_S^R = 0$, and function $G \approx 0$ when $\varepsilon^R = \varepsilon_L^R$. The form of equation (B.110) is consistent with the stress-pseudo strain behavior observed in Figure B.14. This figure shows that the stress is linearly proportional to the pseudo strain when damage is small (i.e., time elapsed is small). This situation corresponds to a constant value of the function C_1 in (B.110), resulting in a linear

relationship between the stress and pseudo strain.

Constitutive Modeling of Asphalt Concrete With Growing Damage and Microdamage Healing

Characteristics of Microdamage Healing

The constitutive model proposed in the preceding section is extended to account for the microdamage healing occurring during rest periods. To obtain necessary experimental data for this task, constant stress/strain amplitude cyclic tests were performed with rest periods. Two stress/strain levels that were high enough to induce some damage to the specimens were used in the tests. Seven different rest periods whose lengths vary from 0.5 second to 32 minutes were introduced three times during each test.

Figure B.23(a) shows typical stress-strain hysteresis loops right before and after a rest period in the controlled-strain mode. A significant increase in the stiffness of the material is observed by comparing the stress-strain diagrams before and after the rest period, which could be due to either linear viscoelastic relaxation, microdamage healing, or both. The dissipated energy has also increased after the rest period. As mentioned previously, one can not determine how much increase in the dissipated energy or in the stiffness is due to the microdamage healing merely by looking at the stress-strain diagrams. Therefore, pseudo strains were calculated and plotted against the stresses in Figure B.23(b). As can be seen in this figure, the pseudo stiffness S^R has significantly increased after the rest period. Since the beneficial effect of the relaxation phenomenon has been accounted for by using the pseudo strain, the changes in S^R due to the rest period observed in this figure are concluded to be a result of the microdamage healing of the material.

Typical trends of S^R during a constant-strain level of cyclic test with and without rest periods are presented in Figure B.24. It is obvious from this figure that the rest periods have a beneficial effect on S^R. After each rest period, S^R increases, which eventually contributes to the increase in the number of cycles to failure.

In order to understand the characteristics of the S^R behavior more clearly, the trend of S^R before and after a single rest period was plotted against number of cycles in Figure B.25. In this figure, the curve OBCD represents the reduction in S^R due to damage growth for the case without a rest period (i.e., $C_1(S_{1n})$), and the curve AB'D' depicts the reduction in S^R due to damage growth after the rest period. S^R has increased from point B to point A after the rest period due to the microdamage healing, and then it decreases as the loading continues after the rest. The beneficial effect of rest period diminishes gradually in Region I, and eventually in Region II, the slope of the curve B'D' is the same as that of the curve CD but the position of the curve has shifted vertically by (S_B^R - S_C^R). Based on this observation, it can be concluded that the curve AB' and the curve B'D' represent re-establishment of damage in the healed zone and damage growth in virgin

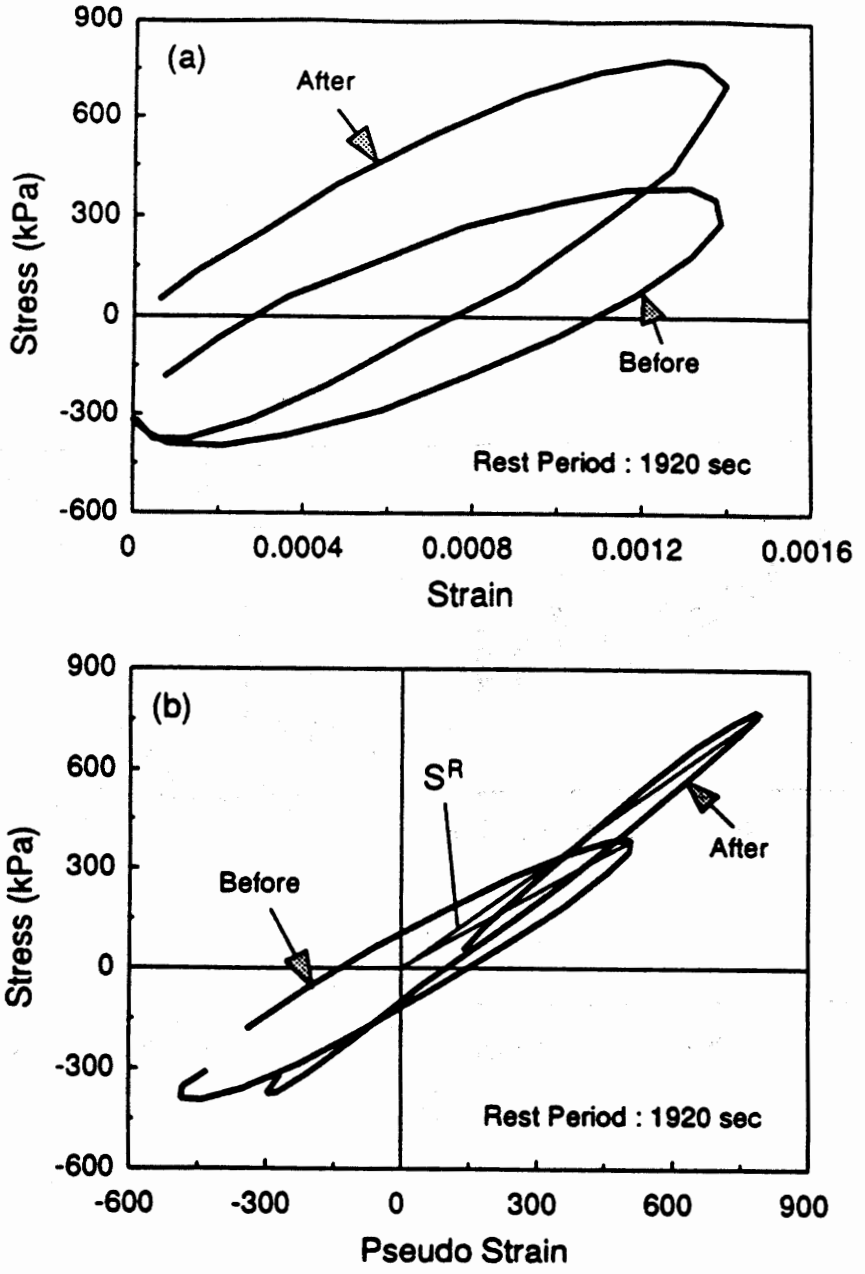

Figure B.23 Application of CP to Cyclic Data With Significant Damage Before and After 480s Rest Period: (a) Stress-strain; (b) Stress-pseudo Strain.

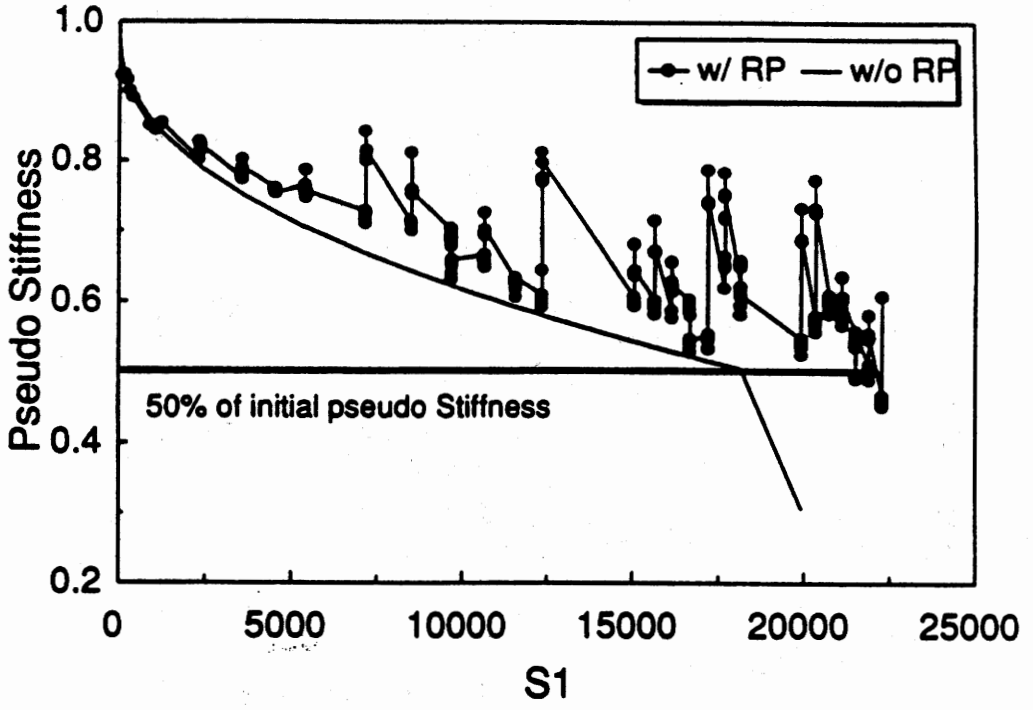

Figure B.24 Change in Pseudo Stiffness Before and After Various Rest Periods.

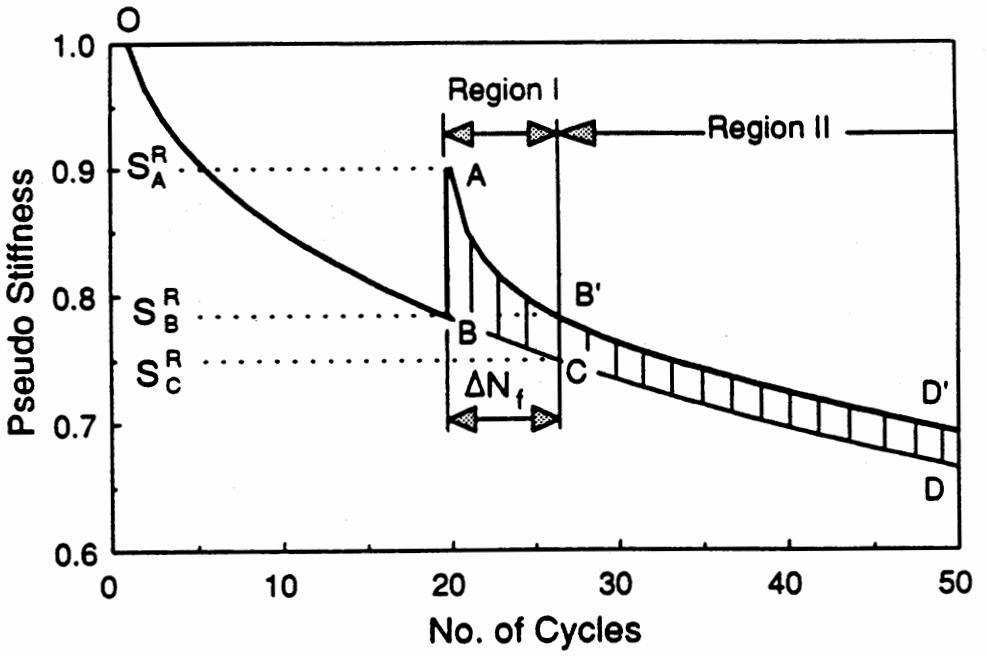

Figure B.25 Change in Pseudo Stiffness Before and After a Single Rest Period.

material, respectively. Therefore, the major factors governing the healing characteristics of the material are not only the increase in S^R during the rest period, but also how slowly the increased S^R diminishes after the rest period (i.e., the slope of the damage evolution curve after the rest period).

Figure B.26 shows the increase in S^R during various rest periods within a test. In Figure B.26(a), there are three S^R data for each rest period because each rest period was introduced three times in the test at different levels of damage in the specimen. The first rest period was introduced at a low level of damage in the specimen. Similarly, the second and third rest periods were introduced at medium and high damage levels, respectively. It is observed from the figure that the higher the damage level, the greater the increase in S^R.

The effect of strain amplitude on the increase in S^R during rest periods is investigated using cyclic data under two different strain amplitudes presented in Figure B.26(b). This figure clearly shows a greater increase in S^R at the higher strain amplitude of 0.0014 units. This trend is consistent with the observation made in Figure B.26(a) because the high strain amplitude develops more damage in the specimen than the low strain amplitude does when the same number of cycles are applied to the specimen. Comparing Figures B.26(a) and B.26(b), it can be said that the strain amplitude has a greater effect on the increase in S^R than the damage level.

The reduction in S^R due to fatigue damage after rest periods was plotted against number of cycles in Figure B.27. The strain amplitude of 0.0014 units data includes the reduction in S^R after three different rest periods. The lengths of rest have a relatively small effect on the S^R behavior after rest periods. The strain amplitude, however, has a significant effect on the S^R behavior. That is, the higher the strain amplitude, the faster the reduction in S^R.

It can be concluded from the above observations that the major factors governing the healing characteristics of the material are not only the increase in S^R during the rest period, but also how slowly the increased S^R diminishes after the rest period. These healing characteristics are heavily dependent on the strain/stress amplitude applied to the specimen. In the following section, two ISV's that can minimize the strain stress-level dependency were employed in order to describe the microdamage healing.

Viscoelastic Constitutive Model With Growing Damage and Healing

Based on the observations made in the preceding subsection, it was assumed that accurate modeling of the changes in S^R during and after rest periods requires two independent internal state variables: one for the increase in S^R during rest periods due to microdamage healing (S_2) and the other for the reduction in S^R after rest periods due to damage evolution (S_3). It was also assumed that the healing does not affect hysteresis function G given in equation (B.107) (this will be proven in the validation study). Therefore, the change in S^R is the only factor to be considered in the modeling. After establishing a constitutive model accounting for the change in S^R, the model will be extended to take into account the hysteretic behavior of each stress-pseudo strain curve by

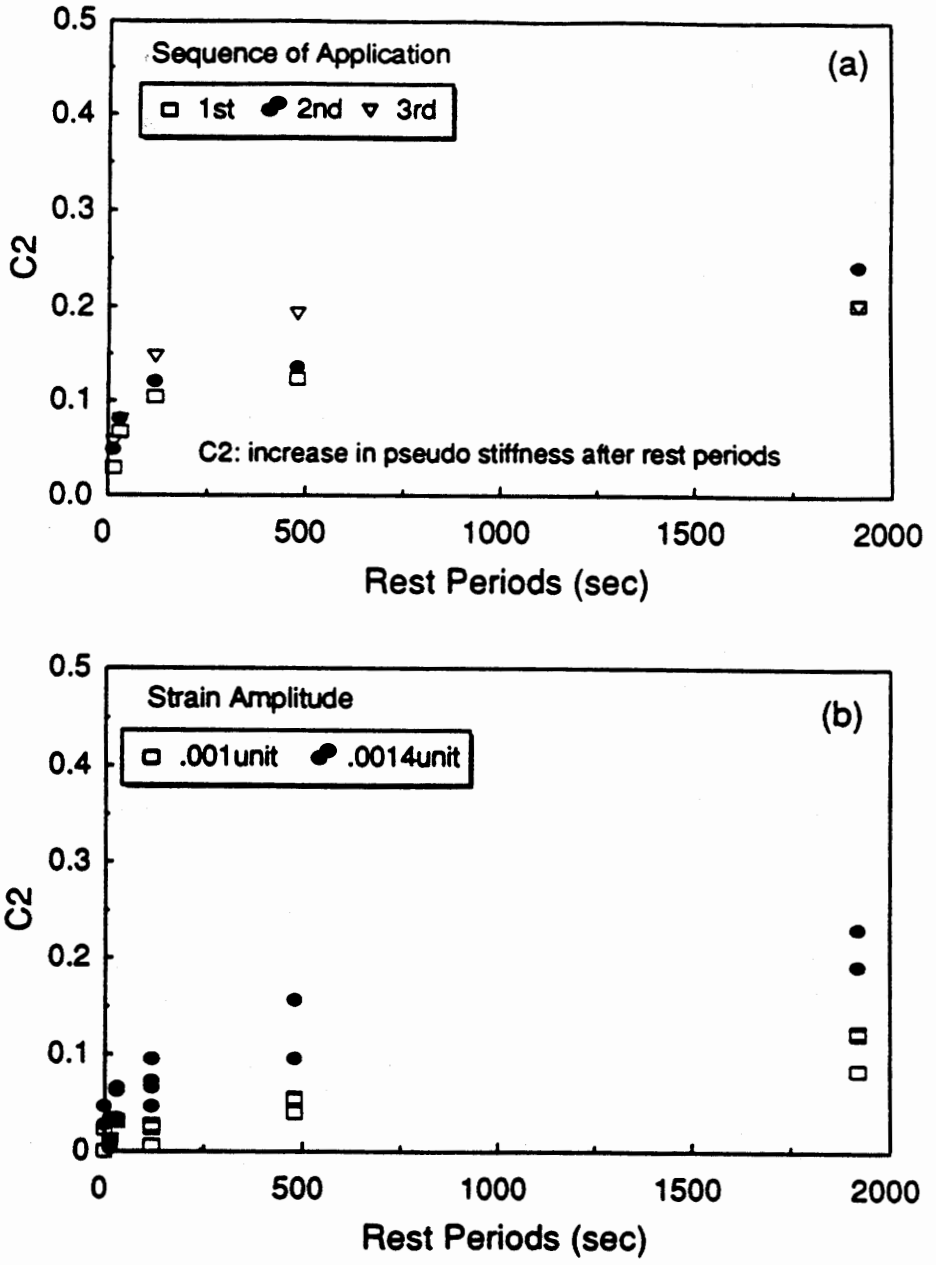

Figure B. 26 Increase in Pseudo Stiffness During Rest Periods: (a) At Different Damage States: (b) Under Different Strain Amplitudes.

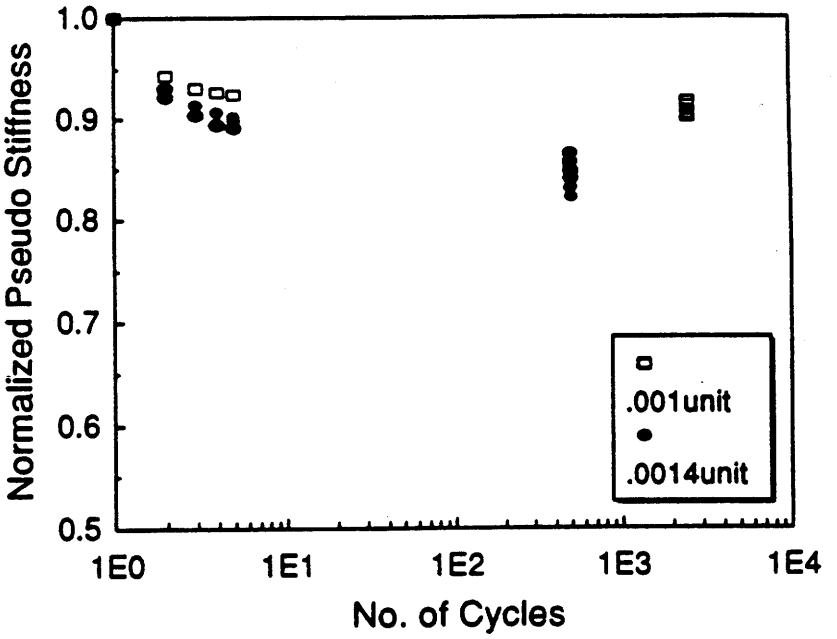

Figure B. 27 Reduction in Normalized Pseudo Stiffness Afer Rest Periods.

employing the function G. In order to simplify the task, only a single rest period is considered in the constitutive modeling, and then the model is generalized to account for the multiple rest periods.

The reduced constitutive equations proposed in this study, accounting for the change in S^R due to growing damage and healing, are summarized in Table B.12. S_B^R in equations (B.111) and (B.112) is the pseudo stiffness before the rest period, as shown in Figure B.25, and is equivalent to $C_1(S_{1n})$ for a single rest period. The constitutive equations (B.89) and (B.90) are special cases of equations (B.111) and (B.112) that describe the reduction in S^R without healing. When there is no rest period, $S_2 = S_3 = 0$, thus $C_2(0) = 0$, and $C_3(0) = 1$. Equations (B.111)-(B.114) will be used in the characterization of the material functions C_2 and C_3.

Since equation (B.112) is a reduced constitutive model that can predict the change in S^R, this model is extended to include the hysteresis function G. Before extending this model, a healing function H is introduced that represents the difference between S^R and $C_1(S_{1n})$ after a rest period:

$$H = \Delta S^R = [S_B^R + C_2(S_2)]C_3(S_3) - C_1(S_{1n}) \tag{B.115}$$

It should be noted that this function H is valid only in Region I in Figure B.25. In Region II, the slope of the curve B'D' is the same as that of the curve CD but the position of the curve has shifted vertically by $(S_B^R - S_C^R)$. Therefore, H is

$$H = \Delta S^R = S_B^R - S_C^R \tag{B.116}$$

Table B.12 Reduced Viscoelastic Constitutive Model With Damage Growth and Healing

Pseudo Strain Energy Density Function:

$$W_m^R = \frac{I}{2} S_B^R C_3(S_3)(\varepsilon_m^R \varepsilon_{me}^R) + \frac{I}{2} C_2(S_2) C_3(S_3)(\varepsilon_m^R \varepsilon_{me}^R) \quad \text{(B.111)}$$

Stress-Pseudo Strain Relations:

$$\sigma_m = I[S_B^R + C_2(S_2)] C_3(S_3)\, \varepsilon_m^R \quad \text{(B.112)}$$

Damage Evolution Laws:

$$\dot{S}_2 = \left(\frac{\partial W_m^R}{\partial S_2}\right)^{\alpha_2} \quad \text{(B.113)}$$

$$\dot{S}_3 = \left(-\frac{\partial W_m^R}{\partial S_3}\right)^{\alpha_3} \quad \text{(B.114)}$$

where

I	=	initial pseudo stiffness,
W_m^R	=	pseudo strain energy density at ε_m^R,
ε_m^R	=	peak pseudo strain in each stress pseudo-strain cycle,
σ_m	=	stress corresponding to ε_m^R, and
ε_{me}^R	=	$\varepsilon_m^R - \varepsilon_S^R$.

The healing function H in equations (B.115) and (B.116) represents the microdamage healing occurring during a single rest period, and thus it is generalized to account for multiple rest periods as follows:

$$H = [S_{B,i}^R + C_2(S_{2,i})]C_3(S_{3,i}) - C_1(S_{1n}) - \sum_{j=1}^{i-1}(S_{B,j}^R - S_{C,j}^R) \quad when\ S^R > S_{B,i}^R\ (Region\ I)$$

or

$$H = \sum_{j=1}^{i}(S_{B,j}^R - S_{C,j}^R) \quad when\ S^R < S_{B,i}^R\ (Region\ II) \tag{B.117}$$

where $S_{2,i}$ = ISV representing the state of healing during the i^{th} rest period,
$S_{3,i}$ = ISV representing the state of damage evolution after the i^{th} rest period,
$S_{B,i}^R$ = S^R before the i^{th} rest period, and
$S_{C,i}^R$ = S^R without rest period at the point when S^R is equal to S_B^R for the case with a rest period.

Now, from equations (B.117) and (B.112), we may obtain

$$\sigma_m = I[C_1(S_{1n}) + H]\,\varepsilon_m^R \tag{B.118}$$

In order to predict inelastic behavior of asphalt concrete on the loading and unloading paths, the hysteresis function G is included in equation (B.118) as follows:

$$\sigma = I[C_1(S_{1n}) + G + H]\,\varepsilon^R \tag{B.119}$$

The final form of the constitutive model considering the mode of loading effects is summarized in Table B.13.

Table B.13 Viscoelastic Constitutive Model With Damage Growth and Healing

$$\sigma = I[F + G + H]\,\varepsilon_e^R \qquad \text{(B.120)}$$

Damage Function F:

$$F = (1 + \frac{\varepsilon_S^R}{\varepsilon_{me}^R})\,[C_{10} - C_{11}(S_{1f}S_{1n})^{C_{12}}]$$

Hysteresis Function G:

$$G = G_0 + G_1 |\frac{\varepsilon^R}{\varepsilon_L^R}|^{G_2(\varepsilon_0^R)}$$

Healing Function H:

$$H = [S_{B,i}^R + C_2(S_{2,i})]C_3(S_{3,i}) - C_1(S_{1n}) - \sum_{j=1}^{i-1}(S_{B,j}^R - S_{C,j}^R) \quad \textit{when } S^R > S_{B,i}^R \textit{ (Region I)}$$

$$H = \sum_{j=1}^{i}(S_{B,j}^R - S_{C,j}^R) \quad \textit{when } S^R < S_{B,i}^R \textit{ (Region II)}$$

where

$$G_2(\varepsilon_0^R) = G_{2R}[\beta_0 + \frac{\beta_1}{\varepsilon_0^R}]$$

$\varepsilon_e^R = \varepsilon^R - \varepsilon_S^R$

$\varepsilon_{me}^R = \varepsilon_m^R - \varepsilon_S^R$

$S_{2,i}$ = ISV representing the state of healing during the i^{th} rest period;

$S_{3,i}$ = ISV representing the state of damage evolution after the i^{th} rest period;

$S_{B,i}^R$ = S^R before the i^{th} rest period, and

$S_{C,i}^R$ = S^R without rest period at the point when S^R is equal to S_B^R for the case with a rest period.

Characterization of Material Functions and Constants

Material Function C_2 and α_2

During rest periods, $S_3 = 0$. Thus $C_3(0) = 1$. Therefore, with this initial condition, equations (B.111) and (B.112) become, respectively,

$$W_m^R = \frac{I}{2} S_B^R (\varepsilon_m^R \varepsilon_{me}^R) + \frac{I}{2} C_2(S_2)(\varepsilon_m^R \varepsilon_{me}^R) \tag{B.121}$$

and

$$\sigma_m = I [S_B^R + C_2(S_2)] \varepsilon_m^R \tag{B.122}$$

Since $\sigma_m/(I\varepsilon_m^R) = S_A^R$ right after the rest period, equation (B.122) can be rewritten as follows:

$$C_2(S_2) = S_A^R - S_B^R \tag{B.123}$$

Therefore, $C_2(S_2)$ represents the difference in S^R before and after the rest period. Differentiating equation (B.111) with respect to S_2 gives

$$\frac{\partial W_m^R}{\partial S_2} = \frac{I}{2} \frac{dC_2}{dS_2} (\varepsilon_m^R \varepsilon_{me}^R) \tag{B.12 4}$$

Substituting equation (B.12 4) into equation (B.123) results in

$$\dot{S}_2 = [\frac{I}{2} \frac{dC_2}{dS_2} (\varepsilon_m^R \varepsilon_{me}^R)]^{\alpha_2} \tag{B.125}$$

The term ($\partial W^R / \partial S_2$) in equation (B.113) was used instead of ($-\partial W^R / \partial S_2$) because the pseudo-strain energy density increases during rest periods (i.e., $dC_2/dS_2 > 0$). Following the characterization procedure described in Approach 2, we can obtain S_2 from equation (B.125) that

$$S_2 = \int_0^{t_{RP}} [\frac{I}{2} \frac{dC_2}{dt} (\varepsilon_m^R \varepsilon_{me}^R)]^{\frac{\alpha_2}{1+\alpha_2}} dt \tag{B.126}$$

where t_{RP} is the duration of rest. When t = 0, $S_2 = C_2 = 0$ because $\varepsilon^R = 0$. $C_2 = S_A^R - S_B^R$ when $t = t_{RP}$. Therefore, we can obtain the following form of S_2 from equation (B.126):

$$S_2 \cong \left[\frac{I}{2}(\varepsilon_m^R \varepsilon_{me}^R)(S_A^R - S_B^R)\right]^{\frac{\alpha_2}{(1+\alpha_2)}} t_{RP}^{\frac{1}{(1+\alpha_2)}} \qquad \text{(B.127)}$$

It can be seen from equation (B.127) that the larger ε_m^R, ε_{me}^R, $(S_A^R - S_B^R)$ and the longer t_{RP}, the greater S_2 is.

The values of C_2 were calculated from equation (B.123) for different rest periods using the measured values of σ_m and ε_m^R. The S_2 values, corresponding to each rest period, were then calculated from equation (B.127) with the C_2 values. The final values of α_2 were obtained through the trial-and-error procedure, and were 1.7 and 1.5 for AAD and AAM mixtures, respectively. The C_2 values were plotted against the S_2 values in Figure B.28. This figure shows that S_2 successfully accounts for the strain-level dependence of the materials. The regression analysis on the data in this figure resulted in the following form:

$$C_2(S_2) = C_{20} + C_{21}(S_2)^{C_{22}} \qquad \text{(B.128)}$$

The regression coefficients in equation (B.128) for the two mixtures are provided in Table B.8.

Material Function C_3 and Constant α_3

After the material is subjected to a rest period, S_1 and S_3 increase due to the damage evolution in the virgin material and in the healed material, respectively, while S_2 remains constant. We can obtain the values of C_3 from equation (B.112) using the material functions C_1 and C_2 characterized so far and the measured σ_m and ε_m^R. Since $C_2 = S_A^R - S_B^R$, equation (B.112) can be reduced to

$$\sigma_m = I S_A^R C_3(S_3) \varepsilon_m^R \qquad \text{(B.129)}$$

It can be seen from equation (B.129) that $C_3(0) = 1$ when $S_3 = 0$ because $S^R = S_A^R$.

Knowing that $S_B^R + C_2 = S_A^R$, the following form of the evolution law for S_3 can be obtained from equations (B.111) and (B.114):

$$\dot{S}_3 = \left[-\frac{I S_A^R}{2}\frac{dC_3}{dS_3}(\varepsilon_m^R \varepsilon_{me}^R)\right]^{\alpha_3} \qquad \text{(B.130)}$$

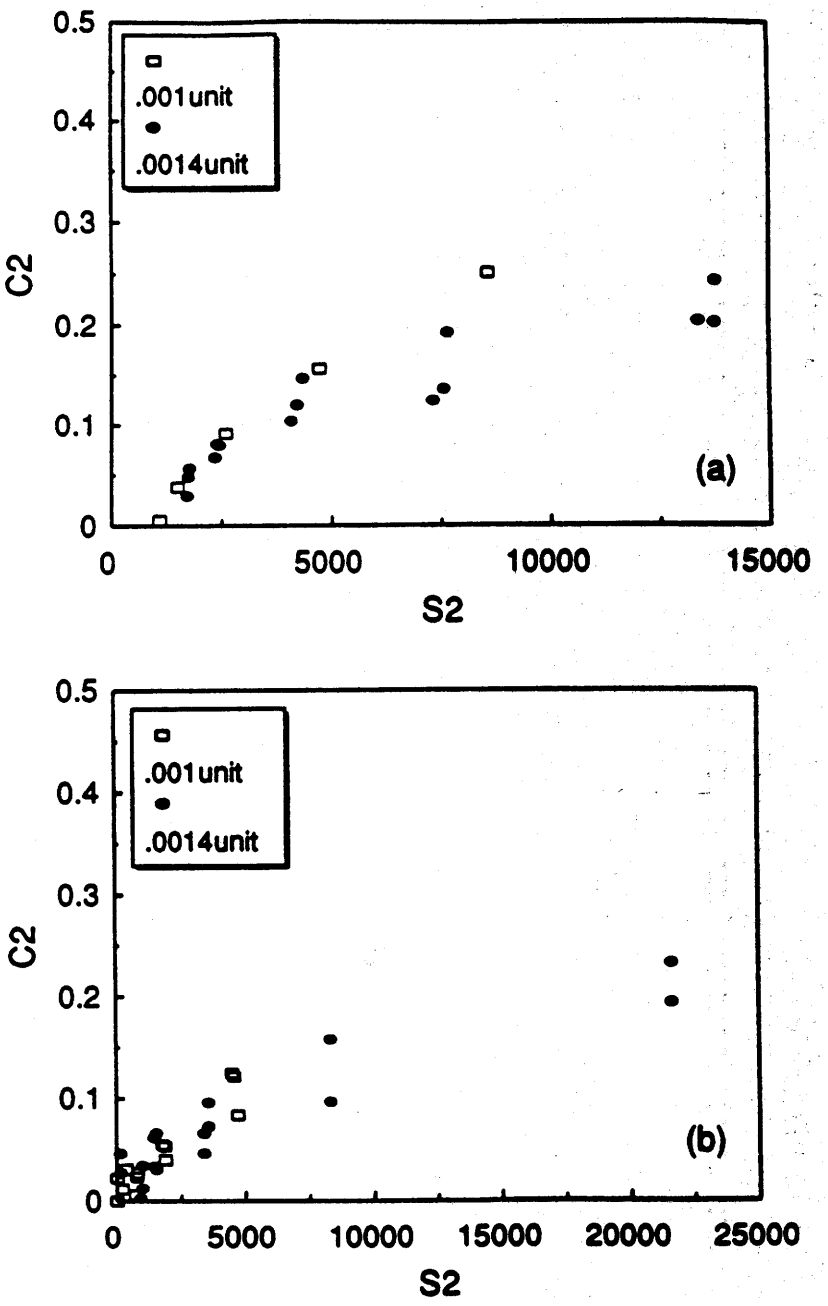

Figure B.28 C_2 Versus S_2: (a) AAD Mixture; (b) AAM Mixture.

Following the characterization procedure described in Approach 2, we can obtain S_3 from equation (B.130):

$$S_3 = \int_0^t [-\frac{IS_A^R}{2}\frac{dC_3}{dt}(\varepsilon_m^R \varepsilon_{me}^R)]^{\frac{\alpha_3}{1+\alpha_3}} dt \qquad \text{(B.131)}$$

The S_3 values after different durations of rest were calculated from equation (B.131) using the C_3 values obtained from equation (B.129) with the assumed values of α_3. The final values of α_3 were determined by examining the cross-plot of C_3 and S_3, and were 2.1 and 2.0 for AAD and AAM mixtures, respectively. Figure B.29 shows the C_3-S_3 behavior for different mixtures. All the data fall on the same curve regardless of the duration of rest. This implies that the slope of C_3-S_3 is independent of the durations of rest as well as the strain amplitude applied during the test. The following power form was obtained from the regression analysis:

$$C_3(S_3) = C_{30} - C_{31}(S_3)^{C_{32}} \qquad \text{(B.132)}$$

The regression coefficients in equation (B.132) are provided in Table B.8.

Comparison of the Material Functions C_1, C_2, and C_3

According to the constitutive model developed in this study, the constitutive behavior of asphalt-aggregate mixtures is mainly dependent on the three internal state functions, $C_1(S_{1n})$, $C_2(S_2)$, and $C_3(S_3)$. Some observations are made on the internal state functions using the model coefficients summarized in Table B.8.

The ISV functions C_1 and C_3 represent the damage growth in virgin materials and healed materials, respectively. The coefficients of C_1 and C_3 are similar. The coefficients C_{10} and C_{30} are close to 1 simply because the functions C_1 and C_3 are determined by normalizing S^R by the initial S^R value. The slope of C_3 (i.e., C_{32}) is slightly larger than that of C_1 (i.e., C_{12}). This implies that the damage grows more quickly in the healed material than in the virgin material. Namely, the strength of the healed zone is not as strong as the intact zone of the material. The AAD mixture has a smaller C_{11} and larger C_{12} values than the AAM mixture, indicating slower decrease in C_1 at very early cycles but overall faster reduction of C_1. This trend is well displayed in Figure B.19.

Another observation based on Table B.8 data is the difference in C_{21} and C_{22} values between AAD and AAM mixtures. The AAD mixture has a smaller value of C_{22} and a larger value of C_{21} than the AAM mixture, indicating the AAD mixture's ability to heal quicker in short rest durations and the AAM mixture's strength in continuous healing over long rest duration.

In order to determine which mixture has a higher microdamage healing potential, one needs to examine both C_2 and C_3 functions. That is, it is important to know not only how much

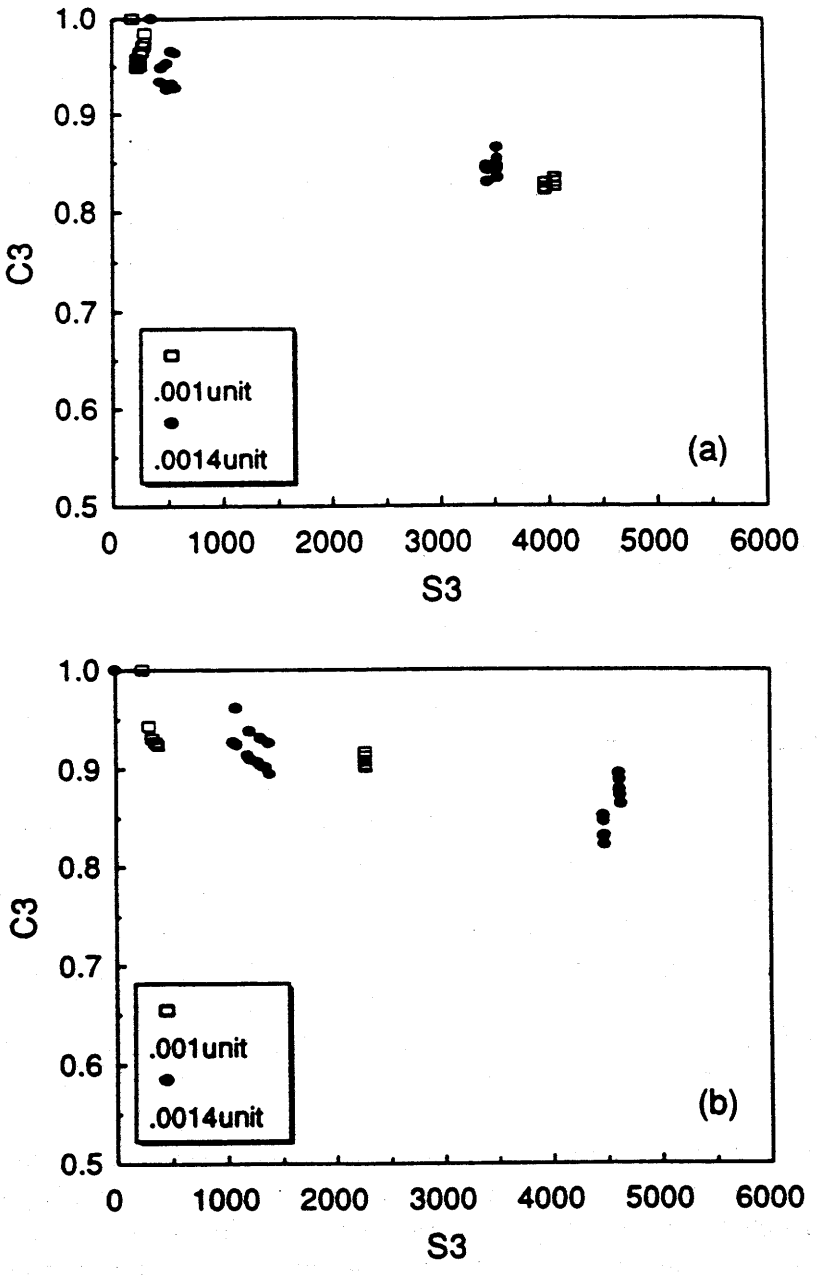

Figure B.29 C_3 Versus S_3: (a) AAD Mixture; (b) AAM Mixture.

increase in S^R has occurred during a certain duration of rest (C_2 function), but also the rate of damage growth after the rest (C_3 function).

Validation of the Constitutive Model

For verification purposes, cyclic loading tests with random durations of rest under multi-level stress/strain amplitudes were performed on both mixtures. The strain history used in the controlled-strain tests for both mixtures is illustrated in Figure B.30(a). The stress histories used in the controlled-stress tests for the AAD and the AAM mixtures are shown in Figure B.30. Stresses in all the verification studies were calculated using the constitutive equation (B.120) given in Table B.13, and the model coefficients tabulated in Table B.8. Strain values measured throughout the testing were used in the calculation of pseudo strains. Figures B.31 and B.32 present the validation results from the controlled-strain cyclic tests of the AAD mixture, and Figures B.33 and B.34 for the controlled-stress cyclic tests of the AAM mixtures.

Controlled-Strain Cyclic Test

Four different strain amplitudes between 0.0008 unit and 0.0015 unit were used in this validation. In order to verify that the constitutive model is independent of strain amplitude, the strain amplitudes which were not used in the characterization of the constitutive model were selected. Also, five different lengths of rest periods between 50 and 800 seconds, which were not used in the characterization of the constitutive model, were selected for the validation study. Sequences of both strain amplitudes and rest periods were random. The strain history used in this test was composed of eight groups of strain applications as shown in Figure B.30(a). The last loading group (Group 8) was applied until the specimen failed. The strain amplitude in each loading group was held constant.

The measured and predicted stresses for loading groups 1, 2, 4, and 8 were plotted against loading time in Figure B.31. The constitutive model successfully predicts the reduction in stress due to cyclic loading regardless of strain amplitudes applied during the test. Figure B.31(d) shows the accuracy of the prediction near the point of failure. These results verify that the constitutive model developed in this study is independent of strain amplitudes. Since the same loading time (0.1 second) was used throughout testing, different strain amplitudes produced different strain rates for each loading group. Thus, the verification results also demonstrate that the model can account for the coupling effects of rate-dependence and damage.

In Figure B.32, the measured and predicted stresses before and after rest periods are plotted against strains. The predictions made by the constitutive equation (B.120) are satisfactory. The increases in stress after varying lengths of rest periods were predicted accurately, as were the effects of different sequences of varying load levels. It should be noted that the hysteresis function G in equation (B.120), developed based on the data obtained from the constant strain amplitude cyclic tests without rest periods, successfully predicts the hysteretic behavior of the loading and unloading paths before and after the various durations of rest all the way up to failure. This

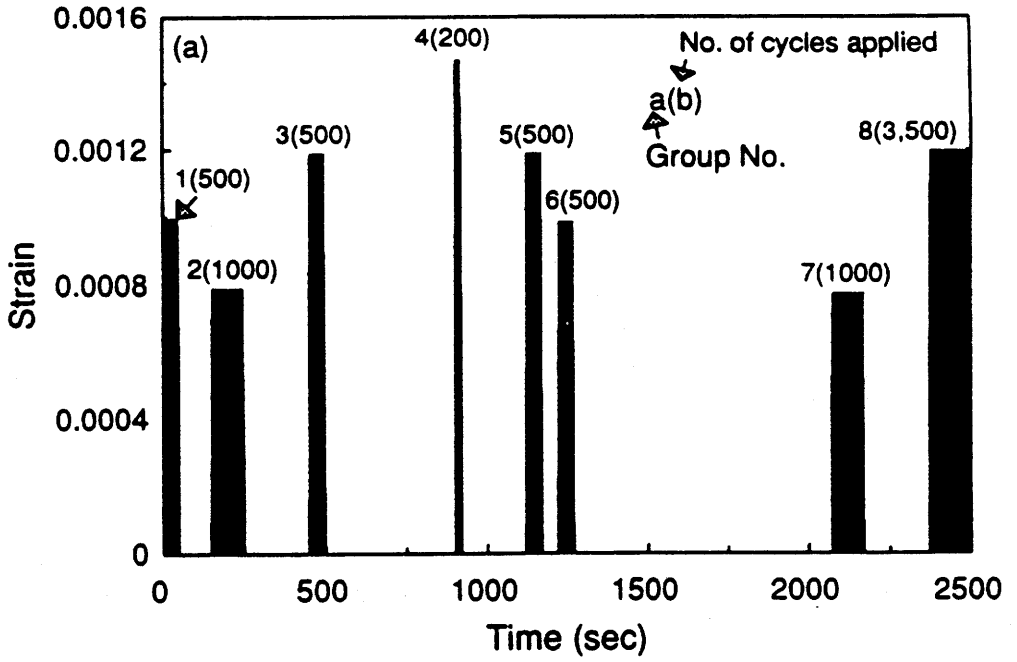

Figure B.30 Validation Loading Histories: (a) Controlled-strain Mode; (b) Controlled-stress Mode for AAD Mixture; (c) Controlled-stress for AAM Mixture.

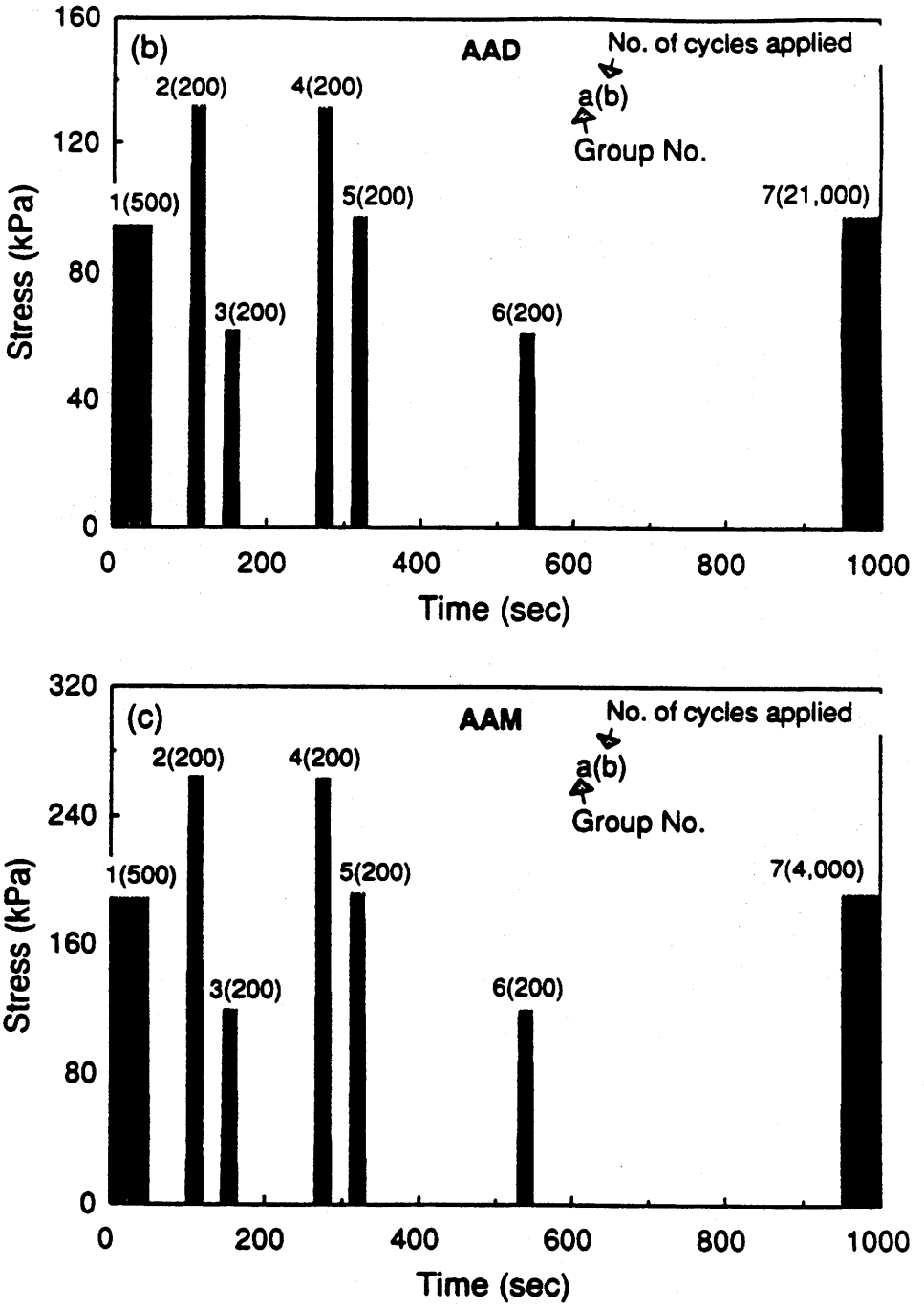

Figure B.30 (Continued)

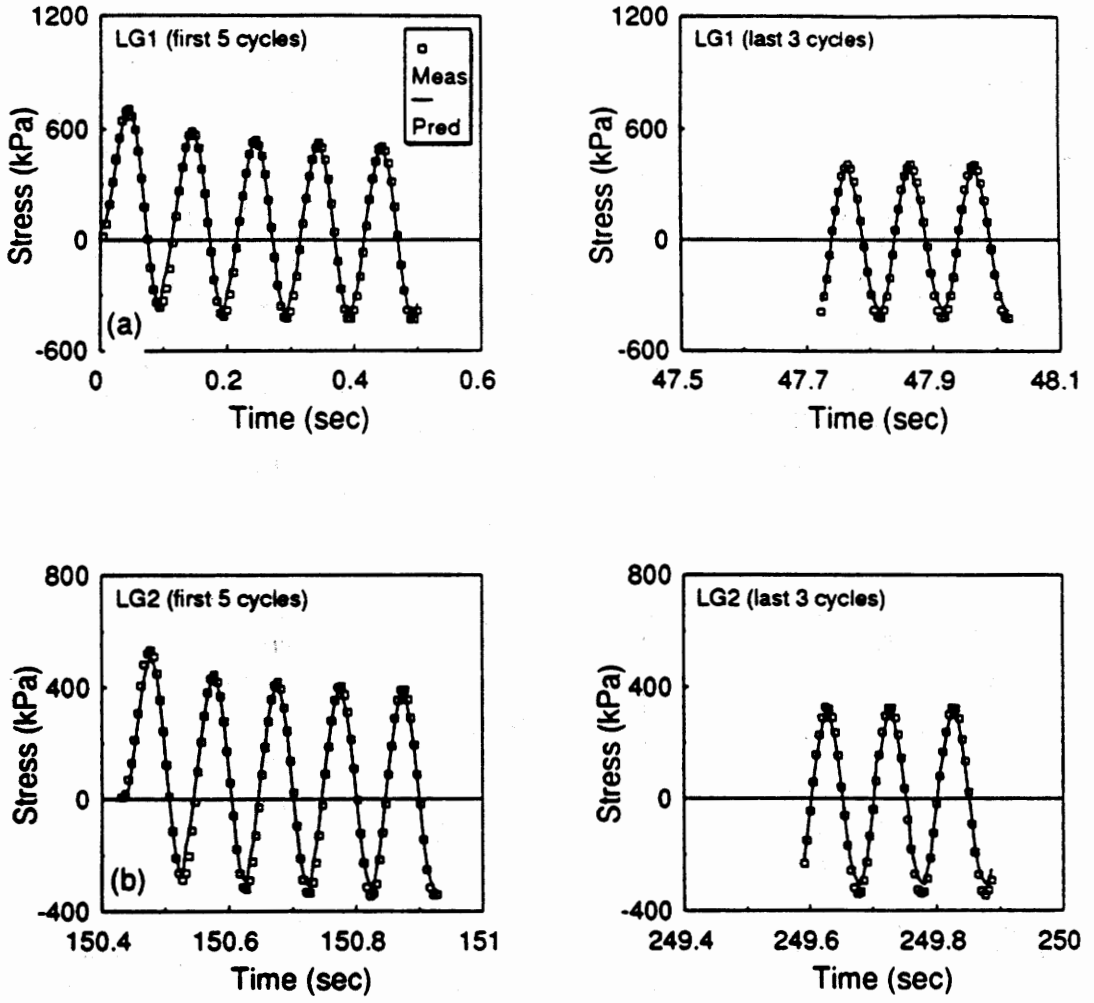

Figure B.31 Prediction of Stresses for Different Loading Groups in the Controlled-strain Validation History for AAD Mixture: (a) Loading Group 1; (b) Loading Group 2; (c) Loading Group 4; (d) Loading Group 8.

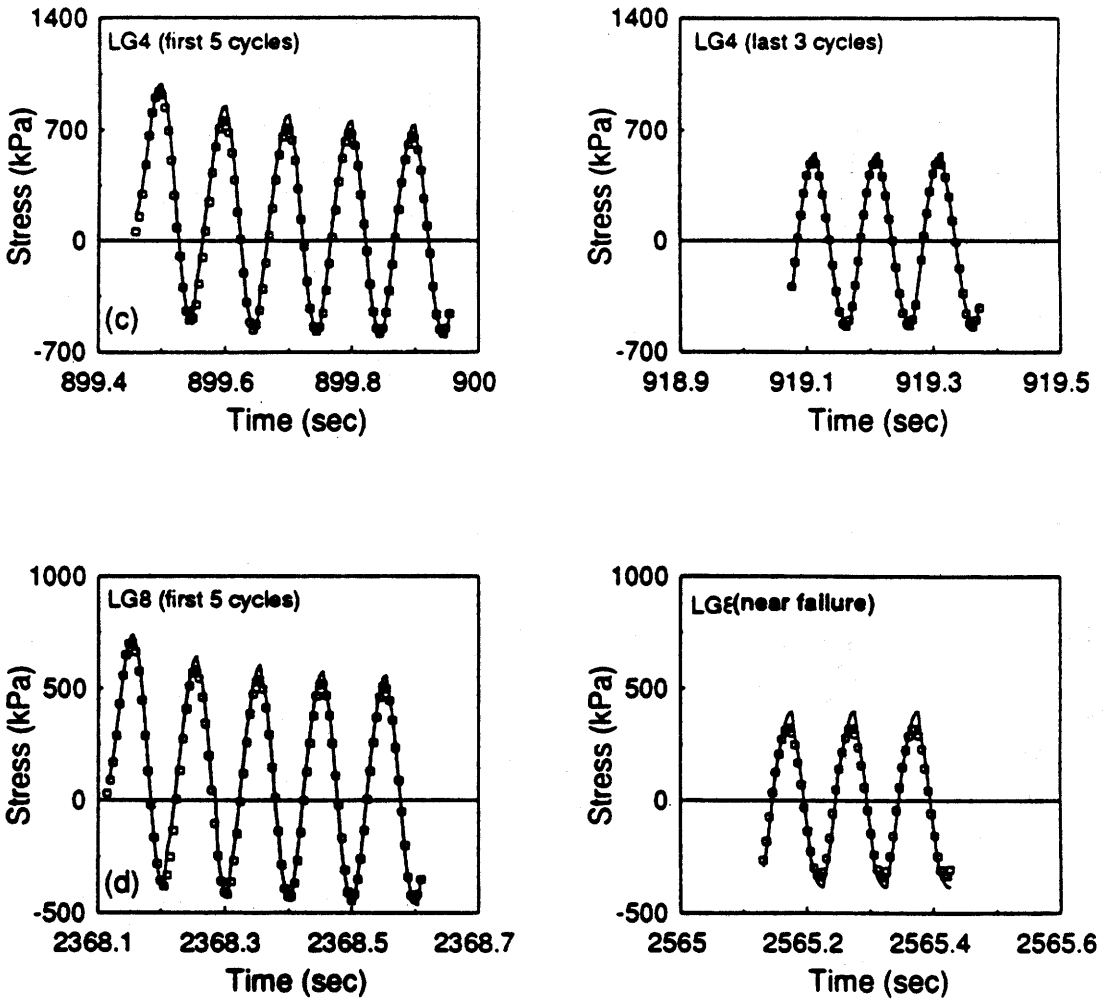

Figure B.31 (Continued)

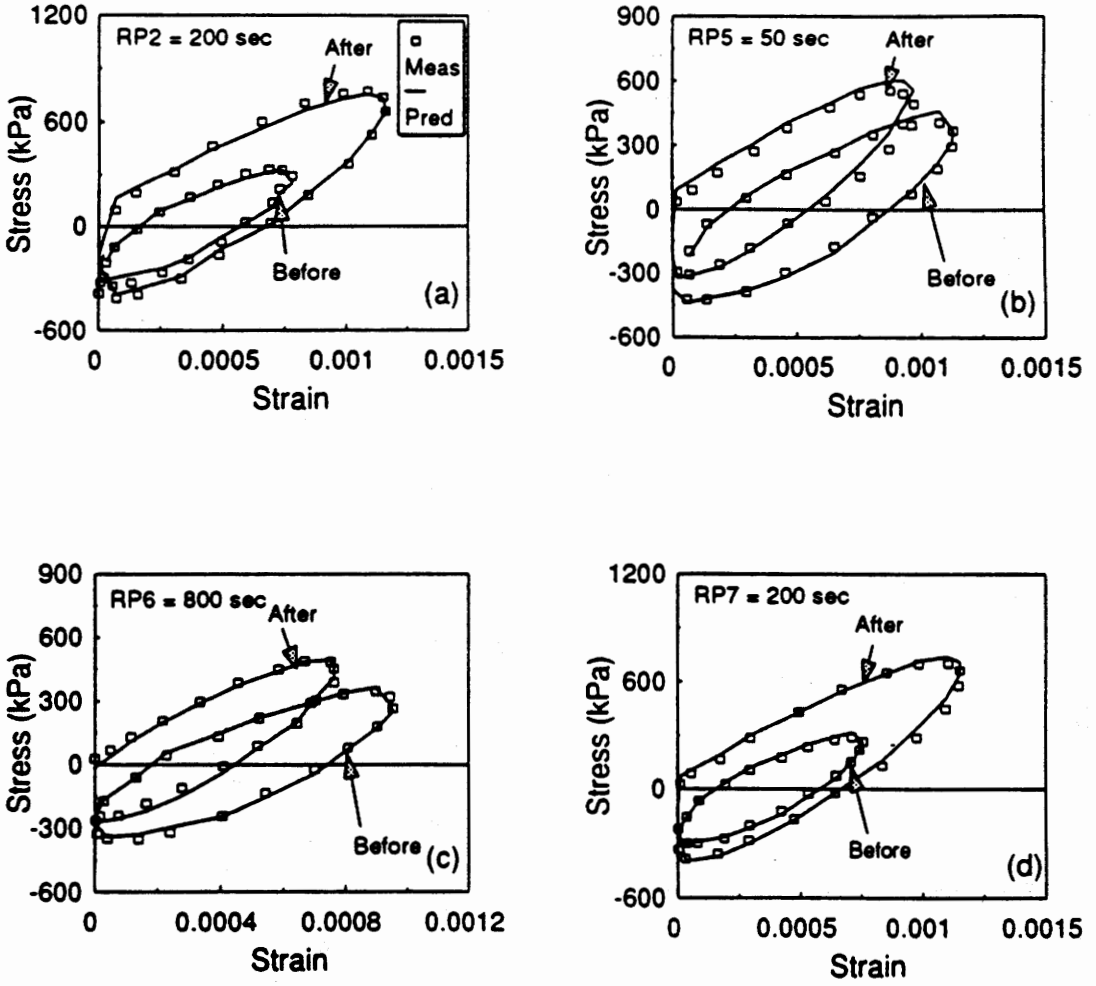

Figure B.32 Prediction of Stresses Before and After Varying Rest Periods for Controlled-strain Mode: (a) 200s; (b) 50 s; (c) 800 s; (d0) 200 s.

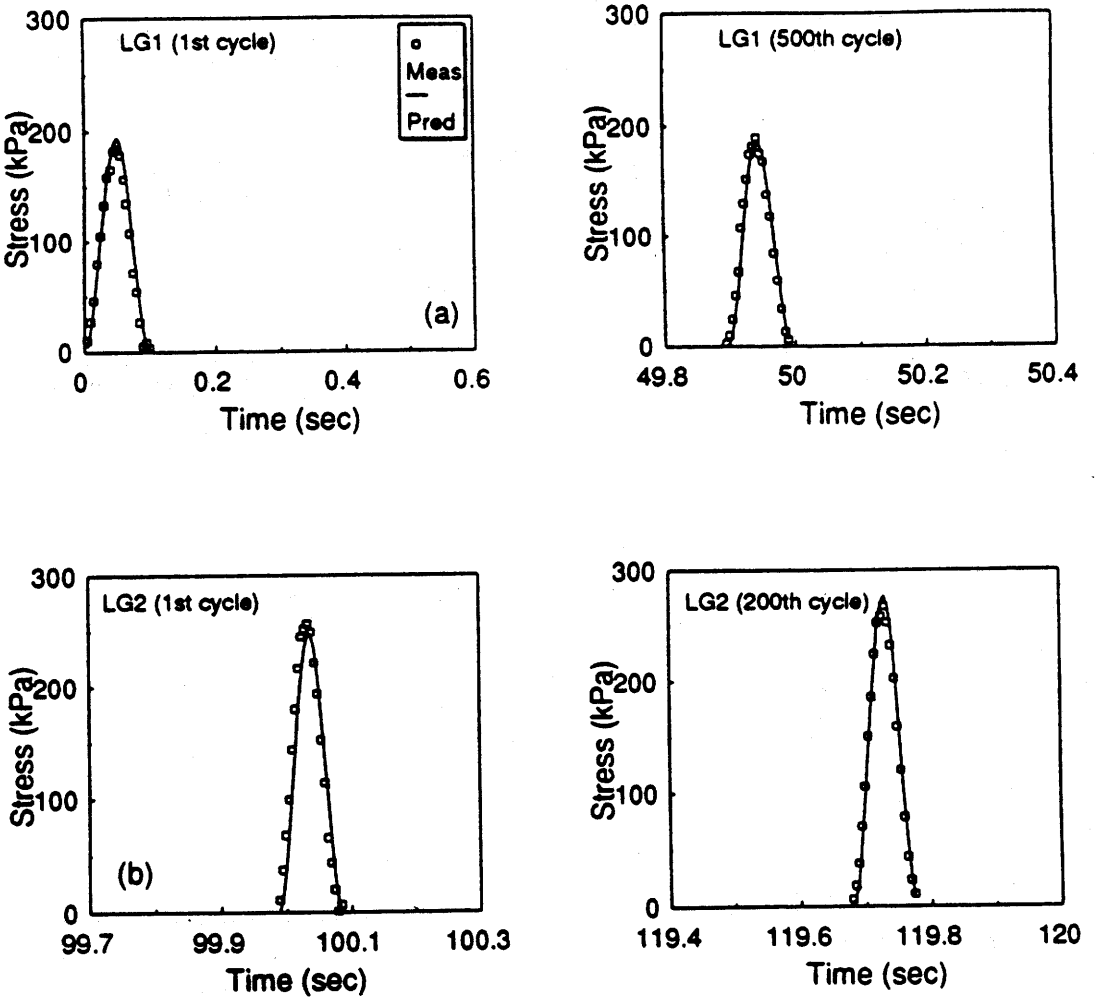

Figure B.33 Prediction of Stresses for Different Loading Groups in the Controlled-stress Validation History for AAM Mixture; (a) Loading Group 1; (b) Loading Group 2; (c) Loading Group 3; (d) Loading Group 5.

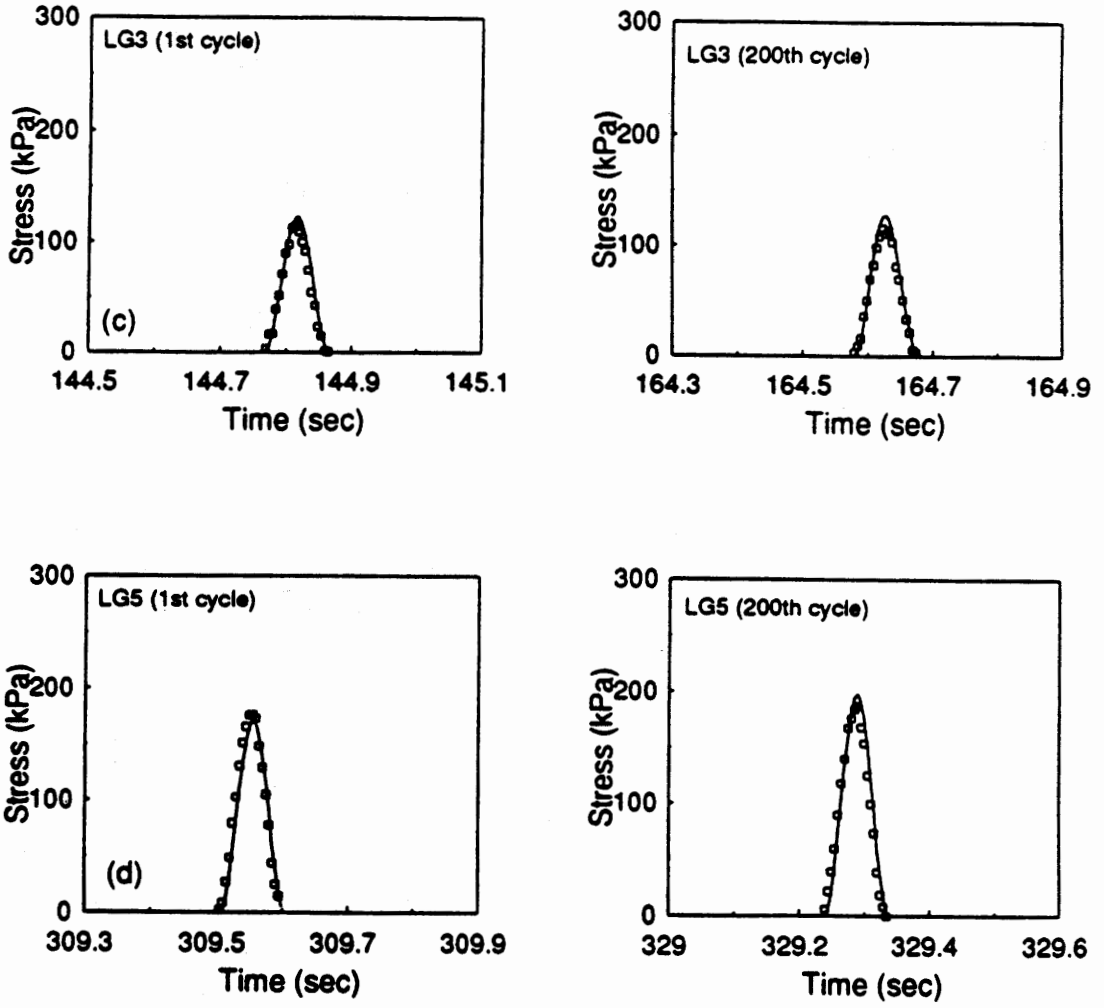

Figure B.33 (Continued)

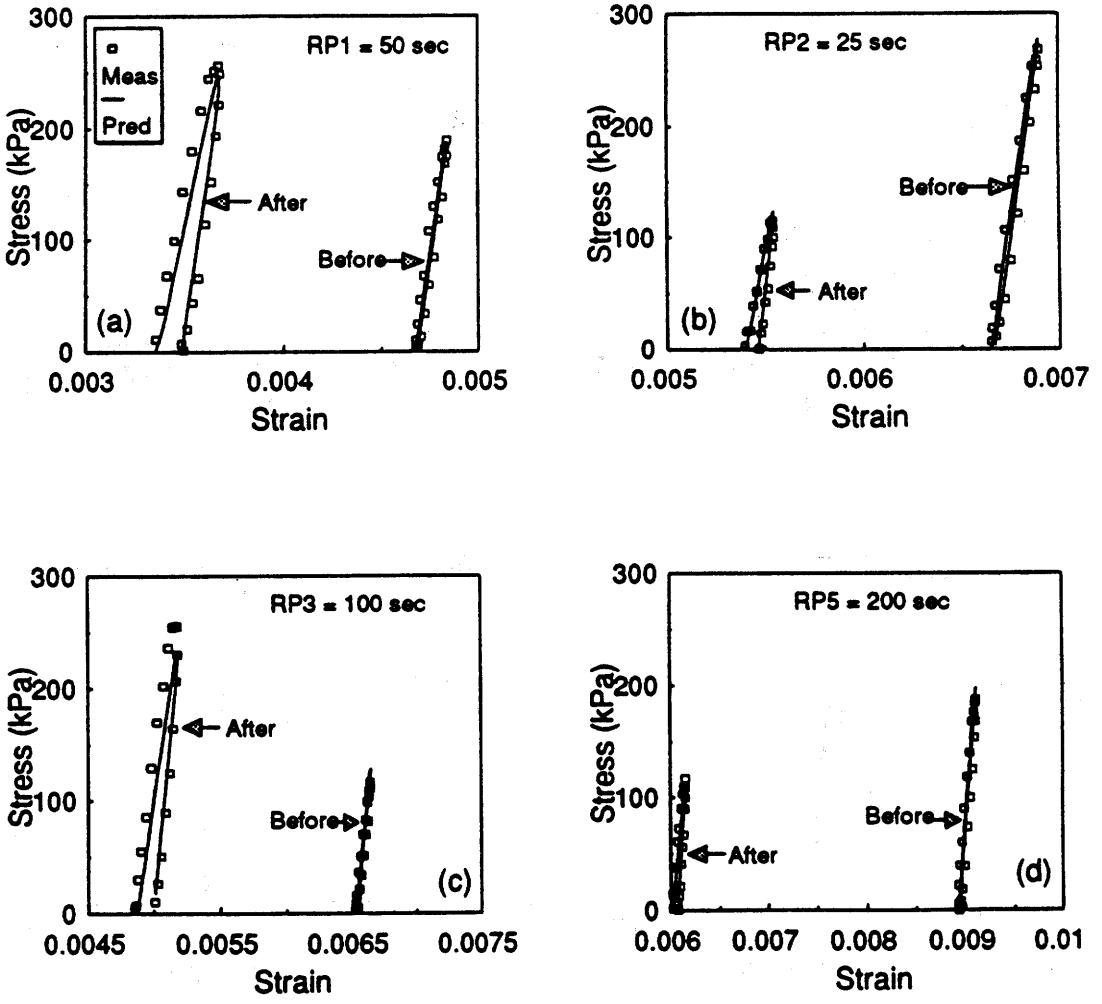

Figure B.34 Prediction of Stresses Before and After Varying Rest Periods for Controlled-stress Mode: (a) 50 s; (b) 25 s; (c) 100 s; (d) 200 s.

implies that the slopes of loading and unloading paths are independent of the fatigue damage or healing incurred in the materials. The validation results for AAM mixture can be found in Lee (1996).

Controlled-Stress Cyclic Test

Three stress amplitudes (66, 99, and 132 kPa) and five rest periods between 25 and 400 seconds were randomly applied to create the stress history shown in Figure B.30(c). Again, the cyclic loading continued in loading Group 7 until failure. The pseudo-strain values were calculated using the measured strain responses. The stresses were then predicted using the constitutive equation (B.120) and compared with the measured stresses in Figure B.33. Figure B.34 displays the validation results for the cycles before and after varying lengths of rest period.

In general, the accuracy of prediction in the controlled-stress cyclic test is acceptable, but a little poorer than the controlled-strain case. It must be noted here that the coefficients in the constitutive model used in the prediction were obtained solely from the controlled-strain cyclic tests. The extrapolation from the controlled-strain mode to the controlled-stress mode might have affected the accuracy. Another reason for the reduced accuracy is attributed to some errors associated with the calculation of pseudo strain in the controlled-stress case due to inaccurate representation of strain history. Unlike the controlled-strain case where the strain history is simple and known a priori, the strain in the controlled-stress mode is the response and needs to be measured during the entire testing period. It is impossible, or at least extremely impractical, to acquire all the stress-strain data up to failure in long-term fatigue tests because of the limitation in computer memory capacity. Therefore, the strain histories in the controlled-stress tests are generated from a limited number of data sets that were collected at different stages of fatigue testing. Strains that were not measured were interpolated using the measured strain values, which introduce some errors in the pseudo strain calculation, resulting in less accurate prediction of stresses in Figures B.33 and B.34. The validation results for AAD can be found in Lee (1996).

Although the prediction within each cycle is not as good as the controlled-strain case, the constitutive model reasonably predicts the stresses up to failure, demonstrating the applicability of the constitutive model to different modes of loading. Due to the inherent difficulties of calculating pseudo-strain values in controlled-stress fatigue tests, controlled-strain cyclic tests are recommended for fatigue testing of asphalt concrete.

Fatigue Performance Prediction

When equation (B.120) is used for fatigue performance prediction (i.e., prediction of the number of cycles to failure, N_f), only the functions F and H are needed, which represent the changes in S^R during cyclic loading and rest periods, respectively. The function G is required to predict hysteretic stress-strain behavior during loading and unloading paths. It is an important component for accurate constitutive modeling but is not needed in predicting N_f, because peak stress and strain values in each cycle are sufficient to model the change in S^R. Therefore, the

fatigue performance prediction using equation (B.120) reduces to accurate modeling of the change in S^R as a function of loading cycles under complex loading histories.

When continuous loading is applied without rest, an S-shape curve (Figure B.19) is observed between C_1 (normalized S^R) and S_1 with a quick drop in C_1 near the failure. The reduction in S^R by 50 percent from the initial S^R value (or C_1 value of 0.5) can be used as the failure criterion irrespective of mode of loading and stress/strain amplitude, which has also been validated by visual observation of specimens' failure during fatigue tests.

These findings lead to the following fatigue performance prediction model:

$$\textit{Failure occurs when} \qquad C_1 + H \leq 0.5 \qquad \text{(B.133)}$$

Since H is a function of $C_2(S_2)$ and $C_3(S_3)$, the left-hand term is a function of the three internal state functions, $C_1(S_{1n})$, $C_2(S_2)$, and $C_3(S_3)$.

A validation study has been performed on the fatigue performance prediction model (B.133) using fatigue test data from AAD and AAM mixtures under controlled-strain mode. The controlled-stress fatigue tests were not used in the validation study because of the inherent difficulties of calculating pseudo-strain values in the controlled-stress fatigue tests as discussed in the preceding section "Validation of the Constitutive Model." The results are presented in Table B.14. The data points in this table represent a total of 16 tests with various combinations of strain amplitudes and rest durations.

As can be seen in this table, there are three specimens that have the percentage of error between the predicted and measured N_f's ranging from 70 to 120 percent. These specimens failed earlier than expected. An additional test was conducted for each of the three points, and the replicates all fall below 10 percent error, indicating that the sample-to-sample variability affected the prediction accuracy in these specimens. In all other tests, the percentage of error was kept below 10 percent.

The effect of rest periods on S^R, and therefore on the fatigue life, is schematically shown in Figure B.25. The increased S^R due to the rest period (i.e., $S_A^R - S_B^R$) results in an increasing number of cycles to failure (ΔN_f). It can be seen from this figure that the beneficial effect of microdamage healing on the fatigue life is governed not only by the increase in S^R observed immediately after the rest, but also by the slope of S^R-N curve in Region I. The ISV's representing these two post-rest characteristics of S^R-N curve are S_2 and S_3 respectively, and thus ΔN_f is a function of S_2 and S_3. When the material is subjected to M number of rest periods, a total increase in the fatigue life due to these rest periods ($\Delta N_{f,\,total}$) is:

$$\Delta N_{f,\,total} = \sum_{i=1}^{M} \Delta N_{f,i} \qquad \text{(B.134)}$$

where $\Delta N_{f,i}$ is the increase in N_f due to the i^{th} rest period.

The total number of cycles to failure (N_f) may be obtained as follows:

$$N_f = N_{f,w/oRP} + \Delta N_{f,total} \tag{B.135}$$

where $N_{f,w/o\ RP}$ is the number of cycles to failure without rest periods. A more specific version of equation (B.135) may be obtained based on the damage evolution law (B.91) with internal state functions C_1-C_3, and the failure criterion described earlier.

Table B.14 Validation of the Fatigue Performance Prediction

Mixture	Strain Amplitude (units)	w/o Rest Periods			w/ Rest Periods		
		Meas. N_f	Pred. N_f	% Error	Meas. N_f	Pred. N_f	% Error
AAD	0.002	550	605	10.0	N/A	N/A	N/A
	0.0014	3000	3010	0.3	12500	13000	3.8
	0.0014	2700	2460	1.6	N/A	N/A	N/A
	0.0009	29000	26560	8.4	20000	44000	120
	0.0009	28000	28950	3.4	N/A	N/A	N/A
	0.0006	170000	162100	4.6	N/A	N/A	N/A
AAM	0.0014	3800	3900	2.6	N/A	N/A	N/A
	0.0014	4000	4030	0.8	N/A	N/A	N/A
	0.001	15000	32400	116	71000	75400	6.2
	0.001	25000	24750	1.0	N/A	N/A	N/A
	0.0007	161000	156900	2.5	N/A	N/A	N/A
	0.0007	100000	179500	79.5	N/A	N/A	N/A

Conclusions and Recommendations

Damage accumulation under uniaxial tensile cyclic loading and microdamage healing during rest periods were modeled in this study using the elastic-viscoelastic correspondence principle and continuum damage theory. The resulting constitutive model successfully predicts the damage growth of asphalt concrete under monotonic loading of varying strain rates and damage growth as well as recovery due to complex cyclic loading histories, in both the controlled-strain and controlled-stress modes, composed of randomly applied multi-level loading with different loading rates and varying durations of rest.

Some important results obtained from this study are as follows:

1. The pseudo strain transformation greatly simplified the task of evaluating damage growth and microdamage healing of asphalt concrete while separating out linear viscoelastic behavior.
2. Both damage parameters S_p and S successfully eliminated stress/strain-level-dependence of asphalt concrete in fatigue behavior, and have a power law relationship under uniaxial cyclic loading.
3. The rate-type evolution law (B.29) was useful for describing the time-dependent damage growth as well as microdamage healing in asphalt concrete under cyclic loading.
4. A direct method of determining internal state variables from the evolution law (B.29) has been established and greatly simplified the characterization procedure.
5. The reduction in S^R by 50 percent from the initial S^R value (or C_1 value of 0.5) seems to be an effective failure criterion irrespective of mode of loading and stress/strain amplitude.
6. Recommendations were made on how the constitutive model can be used for practical fatigue performance prediction of asphalt concrete.

Although the validation results of the constitutive model indicate the strength and versatility of this model which may be used for the fatigue performance prediction of asphalt concrete, further research is recommended to develop a simple test and analysis procedure that can be readily used in specification testing.

The mechanical response of asphalt concrete to thermal or thermomechanical loading, which induces time- and temperature-dependent damage growth, may be predicted using the constitutive model (B.120) by replacing the time that appears in the model with the reduced time given in equation (B.36). The time-temperature superposition principle is, in general, applicable to linear viscoelastic behavior without damage, but may carry over to viscoelastic behavior with damage if the damage evolution law can be expressed in the same reduced time (Park et al., 1996). Therefore, an experimental study is recommended to validate the applicability of the constitutive model to predicting the thermomechanical behavior of asphalt concrete at various temperatures. More research is also required to extend the one-dimensional model to multi-axial loading conditions.

References

Christensen, R.M. (1982). "Theory of Viscoelasticity: An Introduction." Academic Press, New York.

Ferry, J. D. (1950). "Mechanical Properties of Substances of High Molecular Weight; vi. Dispersion in concentrated polymer solutions and its dependence on temperature and concentration." *Jr. Amer. Chem. Soc.*, 72, 3746.

Finn, F., C. Saraf, K. Kulkarni, W. Smith, and A. Abdullah (1977). "The Use of Prediction Subsystems for the Design of Pavement Structures." *Proceedings, Fourth International Conference on Structural Design of Asphalt Pavements*, pp. 3-38.

Fitzgerald, J. E. and J. Vakili (1973). "Nonlinear Characterization of Sand-Asphalt Concrete by Means of Permanent Memory Norms." *Exp. Mech.*, 13(12), 504-510.

Huang, Y. H. (1993). "Pavement Analysis and Design." Prentice Hall, New Jersey.

Ju, J. W. (1991). "On Two-Dimensional Self-Consistent Micromechanical Damage Models for Brittle Solids." *Int. J. Solids Struct.*, 27(2), pp. 227-258.

Kachanov, L. M. (1958). "Time of the Rupture Process under Creep Conditions." Izv. Akad. Nauk, USSR, 8, pp. 26-31.

Kachanov, L. M. (1986). "Introduction to Continuum Damage Mechanics." Martinus Nijhoff Publishers, Dordrecht, Netherlands.

Kim, Y. R. and D. N. Little (1990). "One-Dimensional Constitutive Modeling of Asphalt Concrete." *J. of Eng. Mech.*, ASCE, Vol. 116, No. 4.

Kim, Y. R., Y. Lee, and H. J. Lee (1995). "Correspondence Principle for Characterization of Asphalt Concrete." *J. Materials in Civil Eng.*, ASCE, 7(1), pp. 59-68.

Kim, Y. R., H. J. Lee, and D. N. Little (1996). "Fatigue Characterization of Asphalt Concrete Using Viscoelasticity and Continuum Damage Theory." To be published in *Proceedings of The Association of Asphalt Paving Technologists.*

Krajcinovic, D. (1984). "Damage Mechanics." *Appl. Mech. Rev.*, 37(1-6), pp. 397-402.

Krajcinovic, D. and D. Fanella (1986). "A Micromechanical Damage Model for Concrete." *Eng. Fracture Mech.*, 25(5/6), pp. 585-596.

Krajcinovic, D. (1989). "Continuum Damage Mechanics." *Mechanics of Materials*, 8(2-3), pp.

117-197.

Leaderman, H. (1943). "Elastic and Creep Properties of Filamentous Materials and Other High Polymers." The Textile Foundation, Washington D.C., 175.

Lee, H. J. (1996). "Viscoelastic Constitutive Modeling of Asphalt Concrete Using Viscoelasticity and Continuum Damage Theory." Ph.D. Dissertation, North Carolina State University, Raleigh, North Carolina.

Lee, H. J. and Y. R. Kim (1997). "A Viscoelastic Constitutive Model for Asphalt Concrete under Cyclic Loading." *J. of Eng. Mech.*, ASCE (in Press).

Lemaitre, J. (1984). "How to Use Damage Mechanics." *Nucl. Eng. Design*, 80, pp. 233-245.

Little, D. N., A. Letton, S. Prapnnachari, and Y. R. Kim (1994). "Rheological and Rheo-Optical Characterization of Asphalt Cement and Evaluation of Relaxation Properties." *Transportation Research Record 1436*, Transportation Research Board, National Research Council, Washington D.C.

Monismith, C. L. and Y. M. Salam (1973). "Distress Characteristics of Asphalt Concrete Mixes." *Proc. Assoc. of Asphalt Paving Technologists*, Association of Asphalt Paving, 320-350.

Park, S. W. (1994). "Development of a Nonlinear Thermo-Viscoelastic Constitutive Equation for Particulate Composites with Growing Damage." Ph. D. Dissertation, The University of Texas, Austin, Texas.

Park, S. W., Y. R. Kim, and R. A. Schapery (1996). "A Viscoelastic Continuum Damage Model and Its Application to Uniaxial Behavior of Asphalt Concrete." To be published in *Mechanics of Materials.*

rao Tangella S. C. S., J. Craus, J. A. Deacon, and C. L. Monismith. (1990). "Summary Report on Fatigue Response of Asphalt Mixtures." Report No. SHRP-A/IR-90-011, Strategic Highway Research Program, National Research Council, Washington, DC.

Schapery, R. A. (1975). "A Theory of Crack Initiation and Growth in Viscoelastic Media, Part I: Theoretical Development, Part II: Approximate Methods of Analysis, Part III: Analysis of Continuous Growth." *Int. J. Fracture*, 11, pp. 141-159, 369-388, 549-562.

Schapery, R. A. (1981). "On Viscoelastic Deformation and Failure Behavior of Composite Materials with Distributed Flaws." *1981 Advances in Aerospace Structures and Materials* (eds., S. S. Wang and W. J. Renton), ASME, AD-01, pp. 5-20.

Schapery, R. A. (1982). "Models for Damage Growth and Fracture in Nonlinear Viscoelastic

Particulate Composites." *Proc. 9th U.S. National Congress of Applied Mech.*, American Society of Mechanical Engineers, 237-245.

Schapery, R. A. (1984). "Correspondence Principles and a Generalized J-integral for Large Deformation and Fracture Analysis of Viscoelastic Media." *Int. J. Fract.*, 25, pp. 195-223, 1984.

Schapery, R. A. (1986). "A Micromechanical Model for Nonlinear Viscoelastic Behavior of Particle-reinforced Rubber with Distributed Damage." *Eng. Fracture Mech.*, 25, pp. 845-867.

Schapery, R. A. (1987). "Nonlinear Constitutive Equations for Solid Propellant Based on a Work Potential and Micromechanical Model." *Proc. 1987 JANNAF Structures and Mechanical Behavior Meeting*, CPIA, Huntsville, AL.

Schapery, R. A. (1989). "On the Mechanics of Crack Closing and Bonding in Linear Viscoelastic Media." *Int. Jr. of Fracture*, 39, pp. 163-189.

Schapery, R. A. (1990). "A Theory of Mechanical Behavior of Elastic Media with Growing Damage and Other Changes in Structure." *J. Mech. Phys. Solids*, 38, pp. 215-253, 1990.

Schapery, R. A. (1991). "Analysis of Damage Growth in Particulate Composites using a Work Potential." *Composites Engineering*, Vol. 1. No. 3, pp. 167-182.

Schapery, R. A. (1994). "Nonlinear Viscoelastic Constitutive Equations for Composites Based on Work Potentials." *Mechanics USA 1994 (Proc. 12th U.S. National Congress of Applied Mechanics)*, Appl. Mech. Rev., 47, pp. 269-275.

Sias, J. E. (1996). "Rate-Dependent Stiffnesses of Asphalt Concrete Used for Field to Laboratory Prediction and Fatigue and Healing Evaluation." Master's Thesis, North Carolina State University, Raleigh, NC, 1996.

Sumarac, D. and D. Krajcinovic (1987). "A Self-Consistent Model for Microcrack-Weakened Solids." *Mechanics of Materials*, 6, pp. 39-52.

Wu, C. H. (1985). "Tension-Compression Test of a Concrete Specimen via a Structure Damage Theory." In *Damage Mechanics and Continuum Modeling* (ed., N. Stubbs and D. Krajcinovic), ASCE, New York, pp. 1-12.

REFERENCES

Cominsky, R. J., J. S. Moulthrop, W. E. Elmore, and T. W. Kennedy. *"SHRP Materials Library Asphalt Selection Process."* Center for Transportation Research, University of Texas at Austin, Report No. SHRP-IR-A-89-002, August, 1989.

Finn, F., C. Saraf, K. Kulkarni, W. Smith, and A. Abdullah, *"The Use of Prediction Subsystems for the Design of Pavement Structures,"* Proceedings, Fourth International Conference on Structural Design of Asphalt Pavements, pp. 3-38, 1977.

Harvey, J. T., *"A University of California at Berkeley SHRP A-003A Asphalt Concrete Specimen Preparation Protocol,* Technical Memo. No. TM-UCB-A-003A-91-2, 1991.

Kim, Y. R. and D. N. Little, *"One-Dimensional Constitutive Modeling of Asphalt Concrete,"* J. of Eng. Mech., ASCE, Vol. 116, No. 4, 1990.

Kim, Y. R., S. L. Whitmoyer, and D. N. Little., *"Healing in Asphalt Concrete Pavements: Is it Real ?"* Transportation Research Record 1454, TRB, National Research Council, Washington, D.C., pp. 89-96, 1994.

Kim, Y. R. and Y. C. Lee, *"Interrelationships Among Stiffnesses of Asphalt-Aggregate Mixtures,"* Proceedings, The Association of Asphalt Paving Technologists, Vol. 64, pp. 575-609, 1995 a.

Kim, Y. R., Y. Lee, and H. J. Lee, *"Correspondence Principle for Characterization of Asphalt Concrete,"* J. Materials in Civil Eng., ASCE, 7(1), pp. 59-68, 1995 b.

Kim, Y. R., H. J. Lee, and D. N. Little, *"Fatigue Characterization of Asphalt Concrete using Viscoelasticity and Continuum Damage Theory,"* Journal of the Association of Asphalt Paving Technologists, Vol. 66, 1997.

Lee, H. J., *"Uniaxial Constitutive Modeling of Asphalt Concrete Using Viscoelasticity and Continuum Damage Theory,"* Ph.D. Dissertation, North Carolina State University, Raleigh, NC, 1996.

Lee, H. J. and Y. R. Kim, *"A Uniaxial Viscoelastic Constitutive Model for Asphalt Concrete under Cyclic Loading,"* Jr. of Eng. Mech., ASCE, Jan., 1998.

Moulthrop, J. S., "Memorandum to SHRP Asphalt Research Program Coordinators," 1990.

Park, S. W. and R. A. Schapery, *"A Thermoviscoelastic Constitutive Equation for Particulate Composites with Damage Growth,"* Proc. 1994 Joint Army-Navy-NASA-Air Force (JANNAF) Structures and Mechanical Behavior Working Group Conference, Chemical Propulsion Information Agency, Baltimore, MD, 1994.

Park, S. W. and R. A. Schapery, *"A Viscoelastic Constitutive Model for Particulate Composites with Growing Damage,"* Submitted to Int. J. Solids and Structures, 1996.

Park, S. W., Y. R. Kim, and R. A. Schapery, *"A Viscoelastic Continuum Damage Model and Its Application to Uniaxial Behavior of Asphalt Concrete,"* To be published in Mechanics of Materials, 1996.

Schapery, R. A., *"A Theory of Crack Initiation and Growth in Viscoelastic Media, Part I: Theoretical Development, Part II: Approximate Methods of Analysis, Part III: Analysis of Continuous Growth,"* Int. J. Fracture, 11, pp. 141-159, 369-388, 549-562, 1975.

Schapery, R. A., *"Models for Damage Growth and Fracture in Nonlinear Viscoelastic Particulate Composites,"* Proc. 9th U.S. National Congress of Applied Mech., American Society of Mechanical Engineers, pp. 237-245, 1982.

Schapery, R. A., *"Correspondence Principles and a Generalized J-integral for Large Deformation and Fracture Analysis of Viscoelastic Media,"* Int. J. Fract., 25, pp. 195-223, 1984.

Schapery, R. A., *"A Micromechanical Model for Nonlinear Viscoelastic Behavior of Particle-reinforced Rubber with Distributed Damage,"* Eng. Fracture Mech., 25, pp. 845-867, 1986.

Schapery, R. A., *"Nonlinear Constitutive Equations for Solid Propellant Based on a Work Potential and Micromechanical Model,"* Proc. 1987 JANNAF Structures and Mechanical Behavior Meeting, CPIA, Huntsville, AL, 1987.

Schapery, R. A., *"A Theory of Mechanical Behavior of Elastic Media with Growing Damage and Other Changes in Structure,"* J. Mech. Phys. Solids, 38, pp. 215-253, 1990.

Schapery, R. A., *"Simplifications in the Behavior of Viscoelastic Composites with Growing Damage,"* Proc. IUTAM Symposium on Inelastic Deformation of Composite Materials, Troy, New York, (ed., G. J. Dvorak), Springer, New York-Wien, pp. 193-214, 1990.

Schapery, R. A., *"Nonlinear Viscoelastic Constitutive Equations for Composites Based on Work Potentials,"* Mechanics USA 1994 (Proc. 12th U.S. National Congress of Applied Mechanics), Appl. Mech. Rev., 47, pp. 269-275, 1994.

Sias, J. E., *"Rate-Dependent Stiffnesses of Asphalt Concrete Used for Field to Laboratory Prediction and Fatigue and Healing Evaluation,"* M.S. Thesis, North Carolina State University, Raleigh, NC, 1996.

Tangella, S. C. S. R., J. Craus, J. A. Deacon, and C. L. Monismith, *"Summary Report on Fatigue Response of Asphalt Mixtures,"* Report No. SHRP-A/IR-90-011, Strategic Highway Research Program, National Research Council, Washington, DC., 1990.

Tayebali, A. A., J. A. Deacon, J. S. Coplantz, J. T. Harvey, and C. L. Monismith, *"Mix and Mode-of Loading Effects on Fatigue Response of Asphalt-aggregate Mixes"*, Proceedings, The Association of Asphalt Paving Technologists, Vol. 63, pp. 118-151, 1994.

Van, W. D. and W. Visser, *"The Energy Approach to Fatigue for Pavement Design,* Proceedings, The Association of Asphalt Paving Technologists, Vol. 46, 1, 1977.

Yoder, E. J. and M. W. Witczak, "Principles of Pavement Design", John Wiley & Sons, 1975.